Linear Stability and Sensitivity of a Low-speed Jet in Cross-flow

A DISSERTATION
SUBMITTED TO THE FACULTY OF THE GRADUATE SCHOOL
OF THE UNIVERSITY OF MINNESOTA
BY

Marc Allen Regan

IN PARTIAL FULFILLMENT OF THE REQUIREMENTS
FOR THE DEGREE OF
DOCTOR OF PHILOSOPHY

Krishnan Mahesh, Adviser

May, 2018

Acknowledgements

Foremost, I express my sincere gratitude to my adviser, Dr. Krishnan Mahesh, for his unwavering support for my research, and for his continuous patience, motivation, and encouragement throughout my graduate school career. Prof. Mahesh's combination of physical and theoretical knowledge, as well as his involvement, were paramount in making my doctoral studies stimulating and rewarding.

My wife, Abby, has been my partner in crime throughout my academic journey. Her unconditional love and her support for my graduate studies was second to none. Also, my parents have been behind me all of my life. I am forever indebted to them for all of their love and care.

I would also like to thank all of my committee members: Prof. Joseph Nichols, Prof. Ellen Longmire, and Prof. Bernardo Cockburn. I am thankful for the time and effort that they took to review my dissertation and participate in my final examination.

I will also thank Dr. Prahladh Iyer, for mentoring me early on in graduate school. He is responsible for building the strong foundation that springboarded my research. I would also like to thank various members of Prof. Mahesh's research group, most importantly, Mr. Jacob Keller and Dr. Praveen Kumar, for their fruitful discussions and genuine interest in helping me. Other colleagues that I would like to thank, in no particular order, are Dr. Aswin Gnanaskandan, Dr. Rajapandiyan Asaithambi, Dr. Maninder Grover, Dr. Jeffrey Komives, Mr. Nathaniel Hildebrand, Mr. Aditya Madabhushi, Mr. Mrugank Bhatt, Mr. Karim Alame, Ms. Rong Ma, Mr. Wyatt Horne, Mr. Sreevatsa Anantharamu, Mr. Filipe Brandao and Ms. Yixuan Li. Thank you for enriching my graduate experience, both academically and socially.

Lastly, I thank Dr. Ann Karagozian and her research group for their experimental collaboration and valuable discussions. This research was made possible by generous financial support provided by the Air Force Office of Scientific Research under Grant No. FA9550-15-1-0261. Computational resources were provided by the Minnesota Supercomputing Institute (MSI) and the Texas Advanced Computing Center (TACC) under the Extreme Science and Engineering Discovery Environment (XSEDE) allocation.

To my wife and parents

Abstract

The Jet in Cross-flow (JICF) is a canonical flow that is characterized by a jet of fluid injected transverse to an incoming cross-flow. Complex vortical structures are generated as the cross-flow boundary layer interacts with the jet. Reviews by Margason (1993), Karagozian (2010) and Mahesh (2013) compile most of the research advances over the last seventy years. The goal of this dissertation is to increase understanding of the stability and sensitivity of the JICF. Achieving this goal will directly benefit the many engineering applications which use the JICF, including gas turbine combustor dilution jets, film cooling, vertical and/or short take-off and landing (V/STOL) aircraft, and thrust vectoring. The JICF is studied using direct numerical simulation (DNS) of the Navier-Stokes equations, as well as their adjoint. These equations are key components of this research.

The JICF is studied at a Reynolds number of 2000, and two jet-to-cross-flow velocity ratios: $R = 2$ with an absolutely unstable upstream shear-layer, and $R = 4$ with a convectively unstable upstream shear-layer. Global linear stability analysis is used to study the stability of the turbulent mean flows generated from DNS of the Navier-Stokes equations. Global adjoint sensitivity analysis is used to study the sensitivity of the same mean flows. The linear stability and adjoint sensitivity analyses are combined to obtain global optimal perturbations which generate the largest energy growth over different time-scales. These analyses for the JICF pose formidable challenges due to the use of DNS, and the fact that the JICF turbulent mean flows (around which linear stability, adjoint sensitivity, and optimal perturbation analyses are performed) have no homogeneous directions.

Linear stability analysis of the JICF reveals that the dominant eigenmodes are shear-layer modes whose frequencies match frequencies of the upstream shear-layer observed in simulation (Iyer & Mahesh, 2016) and experiment (Megerian *et al.*, 2007). Asymmetric modes are also present, which are more important to the overall dynamics at higher jet-to-cross-flow ratios. Low-frequency modes persist far downstream, and are connected to wake vortices. For $R = 4$, unstable downstream shear-layer eigenmodes can be more unstable than the upstream shear-layer modes. For each instability mode, there is a corresponding adjoint mode that provides sensitivity information. Adjoint modes show that the upstream shear-layer is most sensitive to perturbations along the upstream side of the jet nozzle exit. Additionally, the lower frequency downstream modes have sensitive regions that extend upstream into the cross-flow boundary layer along the wall. The product of the direct and adjoint modes (i.e. wavemaker) reveals the regions that are most sensitive to localized feedback. Wavemaker results are shown to be consistent with the transition of the upstream shear-layer from absolute to convective instability. Optimal perturbation analysis reveals that for short-time horizons, perturbations that are asymmetric, and grow along the counter-rotating vortex pair (CVP), dominate when $R = 2$. However, as the time horizon increases, growth is focused along the upstream shear-layer. When $R = 4$, the optimal perturbations for short-time scales are dominated by growth along the downstream shear-layer. For long-time horizons, the optimal perturbations become hybrid modes that grow along the upstream and downstream shear-layers, simultaneously.

Contents

Acknowledgements **i**

Dedication **iii**

Abstract **iv**

List of Tables **ix**

List of Figures **xii**

1 Introduction **1**

1.1 Motivation and background 1

1.2 Review of related past work 3

1.3 Overview 9

2 Numerical Methodology **13**

2.1 Governing equations and numerical algorithm 13

2.2 Linear Stability Analysis 16

2.2.1 Solutions of the LNS equations 18

2.2.2 Time horizon 19

2.2.3 Scaling 19

2.2.4 Rotating reference frame 19

2.3 Adjoint sensitivity analysis 22

2.3.1 Solutions of the linearized adjoint equations 26

2.3.2 Wavemaker . . . 27
2.4 Optimal perturbation analysis . . . 28
2.5 Baseflow generation . . . 29

3 Validation **32**
3.1 Linear stability . . . 32
3.1.1 Parallel flow linear stability . . . 33
3.1.2 Bi-Global linear stability . . . 33
3.1.3 Global linear stability . . . 34
3.1.4 Global linear stability and parallel flow linear stability . . . 35
3.1.5 Rotational reference frame . . . 37
3.1.6 IRAM parameters . . . 42
3.2 Adjoint Sensitivity . . . 43
3.2.1 Blasius boundary layer . . . 44
3.2.2 Laminar channel flow . . . 45
3.3 Optimal perturbation . . . 47
3.3.1 Lid-driven cavity validation . . . 47

4 Linear Stability Analysis of the Jet in Cross-flow **53**
4.1 Problem Description . . . 53
4.2 Results . . . 58
4.2.1 Stability analysis of case $R2$ . . . 64
4.2.2 Stability analysis of case $R4$ . . . 66
4.3 Summary . . . 68

5 Adjoint Sensitivity Analysis of the Jet in Cross-flow **71**
5.1 Results . . . 71
5.1.1 Upstream shear-layer . . . 72
5.1.2 Asymmetries in the CVP . . . 73
5.1.3 Downstream of the jet exit . . . 76
5.1.4 Downstream shear-layer . . . 77

5.2 Summary 78

6 Optimal Perturbation Analysis of the Jet in Cross-flow 80

6.1 Results 80

6.2 Optimal perturbations for case $R2$ 85

6.2.1 Short-time horizon 85

6.2.2 Characteristic-time horizon 89

6.2.3 Long-time horizon 90

6.3 Optimal perturbations for case $R4$ 93

6.3.1 Short-time horizon 94

6.3.2 Characteristic-time horizon 95

6.3.3 Long-time horizon 97

6.4 Summary 99

7 Conclusion 101

List of Tables

2.1 Strong scaling performed on Comet (Intel Haswell, 2.5 GHz) for linear stability analysis of the 3D lid-driven cavity. A representative time step is chosen to calculate the time taken for one time step. 20

2.2 Weak scaling performed on Comet (Intel Haswell, 2.5 GHz) for linear stability analysis of the 3D lid-driven cavity. A representative time step is chosen to calculate the time taken for one time step. The loading for each processor is held constant at 83,000 grid elements. 21

3.1 Descriptions of the cases used for validation of linear stability analysis. . 33

3.2 The leading eigenvalues ($c_j = \omega_j/\alpha$) from parallel flow linear stability results for a Blasius boundary layer at $Re = 580$, subject to a streamwise T-S wave, ($\alpha = 0.179$), compared to Criminale *et al.* (2003). 34

3.3 The leading eigenvalues (ω_j) from Bi-Global linear stability of a 2D lid-driven cavity subject to different spanwise wavenumbers (β) compared to Ding & Kawahara (1998). 34

3.4 The leading eigenvalues (ω_j) from linear stability analysis for a stable 3D lid-driven cavity (288^3 elements) at $Re = 1000$ compared to Gómez *et al.* (2014) (64^3 elements) and Giannetti *et al.* (2009) (114^3 elements) for validation. 35

3.5 Two leading eigenvalues (ω_j) from global linear stability for laminar channel flow at $Re = 1000$. Streamwise wavenumbers, α, and spanwise wavenumbers, β, are observed in the global eigenmodes (see figures 3.2 and 3.3) and are used as input to parallel flow stability analysis of Poiseuille flow. The parallel flow stability results are produced by a code available in the supplementary material from Juniper *et al.* (2014). . . . 38

3.6 The leading linear stability eigenvalues from Taylor-Couette flow solved in inertial and rotational frames of reference. 40

3.7 Two leading eigenvalues (ω_1 and ω_2) from adjoint sensitivity for laminar channel flow at $Re = 1000$ are compared to results from parallel (Juniper *et al.*, 2014) and global linear stability. Streamwise wavenumbers, α, and spanwise wavenumbers, β, are observed in the global adjoint eigenmodes (see figures 3.2 and 3.3) and are used as input to the parallel flow stability analysis of Poiseuille flow. The parallel flow stability results are produced using a code available in the supplementary material by Juniper *et al.* (2014). 47

3.8 Details are shown for validation of optimal perturbation analysis for a cubic lid-driven cavity at $Re = 1000$. A characteristic time-scale of 3 was chosen, which is non-dimensionalized by the lid velocity and cavity dimension. The leading eigenvalue λ and the observed energy growth are compared as a % difference of λ. 50

4.1 Details are shown for the simulations used to study the stability of the JICF. Jet to cross-flow ratios R of 2 and 4 are studied at a Reynolds number Re of 2000, based on the average velocity $\overline{v}_{\text{jet}}$ at the jet exit and the jet exit diameter D. Also shown is the jet to cross-flow ratio R^*, based on the jet exit peak velocity $v_{\text{jet,max}}$, and the Reynolds number Re_{cf}, based on the cross-flow velocity u_∞. The momentum thickness of the laminar cross-flow boundary layer is described at the jet exit when the jet is turned off. 55

6.1 Details are shown for optimal perturbation analysis used to study the transient stability of the JICF. Several different time horizons are chosen that are shorter and longer than the characteristic time-scale of the upstream shear-layer, $1/St_{up}$ (see text). Additionally, the leading eigenvalue λ and the observed energy growth are compared as a % difference of λ. Note that the "upstream shear-layer" and "downstream shear-layer" are abbreviated as "Up SL" and "Down SL", respectively. 81

List of Figures

1.1 The instantaneous turbulent flowfield for a JICF with a jet-to-cross-flow velocity ratio of 2, visualized using isocontours of Q-criterion (eq. 3.1) colored by streamwise velocity u. 2

1.2 Shapiro *et al.* (2006) studied the JICF by acoustically pulsing the jet. By varying either the amplitude or the frequency, jet penetration and mixing can be affected. 4

1.3 Sau & Mahesh (2010) developed this map which shows the pulsed JICF split into three distinct regimes based on R and the stroke ratio. Several different simulations and experiments which exhibit optimal jet penetration for different sets of parameters are plotted and they all collapse onto a single line where vortex rings are ejected from the jet exit. 5

1.4 Iyer & Mahesh (2016) proposed this schematic representation of the JICF to aid in identifying the counter-current shear-layer made up of the reverse flow upstream and the jet. 8

1.5 Iyer & Mahesh (2016) computed the counter-current velocity ratios for jet-to-cross-flow ratios of (a) 2 and (b) 4 using the most negative vertical velocity in the reverse flow region (see figure 1.4) and the jet fluid velocity. 8

2.1 Strong scaling of global linear stability analysis of the 3D lid-driven cavity tested on Comet. 20

2.2 Weak scaling of global linear stability analysis of the 3D lid-driven cavity tested on Comet. 21

3.1 Real part of the eigenmodes from linear stability analysis for a 3D lid-driven cavity at $Re = 1000$. The results are shown with positive and negative isocontours of $\tilde{u}, \tilde{v}, \tilde{w} = \pm 0.15$. The associated eigenvalues are shown, with the real part being the growth rate, and the imaginary part being the frequency. Modes (a-c) show good qualitative agreement with Gómez *et al.* (2014). A comparison to the eigenvalues results of Giannetti *et al.* (2009) and Gómez *et al.* (2014) may be found in table 3.4. 36

3.2 Real parts of the first eigenmode corresponding to the eigenvalues in table 3.5 from global linear stability for laminar channel flow at $Re = 1000$. Here, there is no variation in the z-direction, making a single slice sufficient to display all relevant data. The results are shown as an x-y slice ($z = 0$) with contours of $\tilde{w}$ (note: $\tilde{u} = \tilde{v} = 0$). The streamwise and spanwise wavenumbers ($\alpha = \mathrm{i}1$, $\beta = \mathrm{i}0$) are extracted and used as input to classic parallel flow stability analysis of Poiseuille flow. Additionally, the Tri-Global eigenmode Fourier coefficients ($\hat{\boldsymbol{u}}_i$) are compared to the results from parallel stability of Juniper *et al.* (2014) for $|\hat{u}|$, $|\hat{v}|$ and $|\hat{w}|$. Note that every fourth point from Juniper *et al.* (2014) is plotted in an effort to not obscure other data. 38

3.3 The real part of the second eigenmode corresponding to the eigenvalues in table 3.5 from global linear stability for laminar channel flow at $Re = 1000$. The results are shown as x-y ($z = 0$) and $z - x$ ($y = 0$) slices with contours of $\tilde{u}$ and $\tilde{w}$ (note: $\tilde{v} = 0$). The streamwise and spanwise wavenumbers ($\alpha = \mathrm{i}1$ and $\beta = \mathrm{i}1.5$) may be extracted and used as input to a classic parallel flow stability analysis of Poiseuille flow. Tri-Global eigenmode Fourier coefficients ($\hat{\boldsymbol{u}}_i$) are compared to the results from parallel stability of Juniper *et al.* (2014) for $|\hat{u}|$, $|\hat{v}|$ and $|\hat{w}|$. Note that every fourth point from Juniper *et al.* (2014) is plotted in an effort to not obscure other data. 39

3.4 Linear stability results for Taylor-Couette flow are compared. The base-flow is shown in (a). The leading eigenmode when solved in the inertial frame is shown in (b), and (c) shows the solution obtained using a rotating reference frame. Isocontours of Q-criterion colored by $\tilde{u}_\theta$ along with perturbation streamlines are used to show the eigenmodes. 41

3.5 Residual behavior when performing linear stability of Taylor-Couette flow in the inertial (a) and rotating frames (b). 42

3.6 Choosing a τ that is too large will alias eigenvalues to lower frequencies. The three leading eigenvalues are examined for the 3D lid-driven cavity at $Re = 1000$. Four different values of τ are used, and the effect of aliasing on the frequencies is clear for higher values of τ. Note that the stationary eigenvalue is unaffected. 44

3.7 Spatial adjoint sensitivity of a Blasius boundary is used as a validation case. Hill (1995) performed parallel flow adjoint sensitivity analysis at $Re = U_\infty \delta/\nu = 1274$ subject to a T-S wave with $f = \omega/Re = 20 \times 10^{-6}$. Hill (1995) recovered the leading adjoint eigenvalue $\alpha = 0.0895 - \mathrm{i}0.00377$ compared to $\alpha = 0.0894 - \mathrm{i}0.00381$ from the present work. The associated eigenmodes are displayed above and show good agreement when comparing the magnitudes. The grid used by Hill (1995) has 84 elements in the y-direction, compared to the 80 points used in the present work. Note that $\delta_{99} = 4.93\delta \approx 5\frac{y}{\delta}$. 45

3.8 Real part of the first adjoint eigenmode corresponding to the first adjoint sensitivity eigenvalue ω_1 in table 3.7 for laminar channel flow at $Re = 1000$. Here, there is no variation in the z-direction, making a single slice sufficient to display all relevant data. The results are shown as an x-y slice ($z = 0$) with contours of $\tilde{w}^\dagger$ (note: $\tilde{u}^\dagger = \tilde{v}^\dagger = 0$). The streamwise and spanwise wavenumbers ($\alpha = 1$, $\beta = 0$) are extracted and used as input to classic parallel flow stability analysis of Poiseuille flow. Additionally, the adjoint sensitivity eigenmode Fourier coefficients ($\hat{u}_i^\dagger$) are computed and shown in (b). 48

3.9 Real part of the second adjoint eigenmode corresponding to the eigenvalues ω_2 in table 3.7 from adjoint sensitivity for laminar channel flow at $Re = 1000$. The results are shown as x-y ($z = 0$) and $z - x$ ($y = 0.25$) slices with contours of $\tilde{u}^\dagger$, $\tilde{v}^\dagger$, and $\tilde{w}^\dagger$. The adjoint sensitivity eigenmode Fourier coefficients ($\hat{\boldsymbol{u}}_i^\dagger$) are shown for completeness (c). 49

3.10 Validation for lid-driven cavity at Re=1000 for optimal perturbation analysis. The energy growths are plotted as lines of different shades of blue, and the corresponding eigenvalues, λ, are shown as symbols at $\tau = 3$. . . 51

3.11 The first four leading optimal perturbations (corresponding to table 3.8) showing the initial perturbations (a-d) and their evolution at τ (e-h) for the lid-driven cavity. 52

4.1 A schematic of the jet in cross-flow computational domain is shown. The origin is located at the center of the jet exit. A Blasius boundary layer is prescribed as the leftmost inflow condition. Additionally, uniform inflow is prescribed for the jet inflow. The nozzle shape is modelled using a 5th order polynomial that matches the nozzle used in experiments of Megerian *et al.* (2007). 54

4.2 The 80 million element computational grid is shown. A view of the symmetry plane (a), as well as a wall normal plane near the jet exit (b), and the nozzle (c) are shown. 55

4.3 The refined, 138 element computational grid that is used in linear stability, adjoint sensitivity and optimal perturbation analyses is shown. A view of the symmetry plane (a), as well as a wall normal plane near the jet exit (b), and the nozzle (c) are shown. 56

4.4 Isocontours of Q-criterion colored by streamwise velocity for the instantaneous turbulent flowfield for $R = 2$ (a) and $R = 4$ (b). 57

4.5 Cross-sectional views of the turbulent mean flows at the symmetry plane that are used as the base states for linear stability, adjoint sensitivity, and optimal perturbation analyses for cases $R2$ (a) and $R4$ (b). Contours of velocity magnitude $|\overline{\boldsymbol{u}}|$ are shown. 59

4.6 Results from the grid convergence study used to determine the sensitivity of the leading eigenvalue to the mesh for case $R2$. Three different grids were tested: coarse (10 million elements), normal (80 million elements), fine (99 million elements). St_1 highlights the primary Strouhal number observed along the upstream shear-layer in simulations by Iyer & Mahesh (2016). 60

4.7 Linear stability analysis spectrum for the JICF at $Re = 2000$ for $R = 2$ (a) and $R = 4$ (b). The vertical blue dashed lines correspond to most dominant frequencies from DNS vertical velocity spectra in the upstream shear-layer obtained by Iyer & Mahesh (2016). The DNS frequency of $St_2 = 1.3$ from Iyer & Mahesh (2016) is not shown in (a) as it would obscure the lower frequency linear stability results. Eigenvalues (ω_j) with red symbols are unstable modes (i.e. positive growth rate), while stable values are colored green. The circled eigenvalues have their corresponding eigenmodes shown in Figure 4.8 for $R = 2$ (a) and $R = 4$ (b). 61

4.8 Real part of the eigenmodes for case $R2$ at $St = 0.62$ (a) and $R4$ at $St = 0.75$ (b) are shown with positive and negative isocontours of $\tilde{u}$ and $\overline{v}$. Isocontours of Q-criterion for the DMD modes by Iyer & Mahesh (2016) are shown for $R2$ at $St = 0.65$ (c) and $St = 1.3$ (e) and for $R4$ at $St = 0.39$ (d) and $St = 0.78$ (f). 63

4.9 Slices of eigenmodes and DMD modes (Iyer & Mahesh, 2016) at the symmetry plane ($z = 0$) with contours of Q-criterion. The eigenmodes have frequencies of $St = 0.62$ (a) and $St = 0.75$ (b) for $R = 2$ and $R = 4$, respectively. The DMD modes have frequencies for case $R2$ at $St = 0.65$ (c) and $St = 1.3$ (e) and case $R4$ at $St = 0.39$ (d) and $St = 0.78$ (f). . . 65

4.10 Real part of the eigenmodes for case $R2$ are shown with positive and negative isocontours of $\tilde{u}$ and $\overline{v}$ contours of the base state in the background. The eigenvalues are shown above, with the real part being the growth rate, and the imaginary part being the Strouhal number. Mode (a) corresponds to the most unstable and highest frequency upstream shear-layer mode. Modes (b-e) are lower frequency and originate near the downstream shear-layer and travel far downstream. Modes (d) and (e) also show a connection between near-wall motions and motions in the jet wake. 67

4.11 Real part of the eigenmodes for case $R4$ are shown with positive and negative isocontours of $\tilde{u}$ and $\overline{v}$ contours of the base state in the background to highlight the jet baseflow. The associated eigenvalues are shown above, with the real part being the growth rate, and the imaginary part being the Strouhal number. Modes (a-g) correspond to the higher frequency downstream shear-layer modes. Mode (h) is associated with the upstream shear-layer. 69

5.1 Eigenvalues from linear stability and adjoint sensitivity for $R2$ (a) and $R4$ (b). The blue-dashed lines correspond to the dominant frequencies observed within the upstream shear-layer by Iyer & Mahesh (2016). The legend subscripts refer to results from the 80 million and 138 million grids. 72

5.2 The $R2$ upstream shear-layer linear stability (a) and adjoint sensitivity analyses (b) eigenmodes along with their associated wavemaker (c-d). Symmetry plane contours show the vertical velocity of the baseflow $\overline{v}$. . 72

5.3 Similar to figure 5.2, but for the $R4$ upstream shear-layer. 73

5.4 Similar to figure 5.2, but for the $R2$ *left-leaning* asymmetric eigenmodes. 74

5.5 Similar to figure 5.2, but for the $R4$ *left-leaning* asymmetric eigenmodes. 74

5.6 Similar to figure 5.2, but for a representative pair of $R2$ downstream eigenmodes. 76

5.7 Similar to figure 5.2, but for the $R4$ lowest frequency eigenmodes. 76

5.8 Similar to figure 5.2, but for the $R4$ leading downstream shear-layer eigenmodes (circled in figure 5.1b). Note that (a) is generated using the 80 million grid. 77
6.1 Transient growth is shown for case $R2$, optimized for different τ, which are differentiated by color and the vertical dash-dotted lines. Additionally, the upstream shear-layer characteristic time-scale, $1/St_{\mathrm{up}}$, is shown as a vertical black dashed line to provide temporal context. Eigenvalues for different τ are shown on their associated vertical lines. 83
6.2 Similar to figure 6.1, but for case $R4$. Additionally, the time-scale of the downstream shear-layer, $1/St_{\mathrm{dn}}$, is shown as another vertical black dashed line. 84
6.3 Case $R2$, short-time horizon, $\tau = 0.4$, final state of the leading asymmetric optimal perturbations. 86
6.4 Case $R2$, short-time horizon, $\tau = 0.8$, final state of the leading asymmetric optimal perturbations. 86
6.5 Case $R2$, short-time horizon, $\tau = 0.4$, final state of sub-optimal asymmetric optimal perturbations with decreasing growth factors and increasing circumferential wavenumbers. 87
6.6 Case $R2$, short-time horizon, $\tau = 0.4$, origination (a) and final state (b) of the sub-optimal downstream shear-layer perturbation. 87
6.7 Case $R2$, short-time horizon, $\tau = 0.8$, origination (a) and final state (b) of the sub-optimal downstream shear-layer perturbation. 88
6.8 Case $R2$, short-time horizon, $\tau = 0.4$, final state of the sub-optimal hybrid asymmetric downstream shear-layer and perturbations. 88
6.9 Case $R2$, short-time horizon, $\tau = 0.8$, final state of sub-optimal asymmetric optimal perturbations with decreasing growth factors and increasing circumferential wavenumbers. 88
6.10 Case $R2$, characteristic-time horizon, $\tau = 1.6$, origination (a) and final state (b) of the leading downstream shear-layer optimal perturbations. . 89

6.11 Case $R2$, characteristic-time horizon, $\tau = 1.6$, final state of the sub-optimal hybrid asymmetric downstream shear-layer optimal perturbations. 89
6.12 Case $R2$, characteristic-time horizon, $\tau = 1.6$, final state of the sub-optimal upstream shear-layer optimal perturbations, along with higher circumferential wavenumbers with decreasing growth factors. 90
6.13 Case $R2$, long-time horizon, $\tau = 3.2$, final state of the leading upstream shear-layer optimal perturbations, along with lower growth factor perturbations with increasing circumferential wavenumbers. 91
6.14 Case $R2$, long-time horizon, $\tau = 3.2$, origination (a) and final state (b) of the sub-optimal downstream shear-layer optimal perturbation. 91
6.15 Case $R2$, long-time horizon, $\tau = 3.2$, final state of the sub-optimal hybrid shear-layer optimal perturbations. 92
6.16 Case $R2$, long-time horizon, $\tau = 4.9$, final state of the leading upstream shear-layer optimal perturbations, along with lower growth factor perturbations with increasing circumferential wavenumbers. 92
6.17 Case $R2$, long-time horizon, $\tau = 4.9$, originations (a-c) and final state (d-f) of the sub-optimal hybrid shear-layer optimal perturbations, organized in order of decreasing growth factor. 93
6.18 Case $R4$, short-time horizon, $\tau = 0.4$, origination (a-d) and final state (e-h) of the leading downstream shear-layer perturbation, in addition to sub-optimal higher wavenumber perturbations with decreasing growth factors that are not symmetric across the $z = 0$ plane. 94
6.19 Case $R4$, short-time horizon, $\tau = 0.8$, origination (a-c) and final state (d-f) of the leading downstream shear-layer perturbation, in addition to sub-optimal higher wavenumber perturbations with decreasing growth factors that are not symmetric across the $z = 0$ plane. 95
6.20 Case $R4$, short-time horizon, $\tau = 0.4$, origination (a) and final state (b) of sub-optimal upstream shear-layer perturbation with a high circumferential wavenumber. 96

6.21 Case $R4$, short-time horizon, $\tau = 0.8$, final state of sub-optimal upstream shear-layer perturbation, along with lower growth factor perturbation with higher circumferential wavenumbers. 96
6.22 Case $R4$, characteristic-time horizon, $\tau = 1.6$, final state of the leading downstream shear-layer optimal perturbations, as well as sub-optimal perturbations with decreasing growth factor and increasing circumferential wavenumbers. 96
6.23 Case $R4$, characteristic-time horizon, $\tau = 1.6$, origination (a-d) and final state (e-h) of the sub-optimal hybrid shear-layer optimal perturbations organized with decreasing growth factors. 97
6.24 Case $R4$, characteristic-time horizon, $\tau = 3.1$, origination (a) and final state (b) of the leading downstream shear-layer optimal perturbations. . 98
6.25 Case $R4$, long-time horizon, $\tau = 3.1$, sub-optimal hybrid shear-layer perturbations organized with decreasing growth factor. Note that the initial perturbations (a-d) are above the associated final states (e-h). 98
6.26 Case $R4$, long-time horizon, $\tau = 4.7$, sub-optimal hybrid shear-layer perturbations organized with decreasing growth factor. Note that the initial perturbations (a-c) are above the associated final states (d-f). 99

Chapter 1

Introduction

1.1 Motivation and background

Jets in cross-flow (JICF), or transverse jets, are canonical flows where a jet of fluid is injected transverse to an incoming cross-flow. Typically, a flat-plate boundary layer interacts with a wall-normal jet, creating a complex array of inter-related vortical structures, as shown in figure 1.1. Shear-layer vortices and the Kelvin-Helmholtz instability are typically observed on the upstream side of the jet. The counter-rotating vortex pair (CVP), which dominates the jet cross-section (Kamotani & Greber, 1972; Smith & Mungal, 1998), persists far downstream and is a characteristic feature of transverse jets. Additionally, horseshoe vortices are formed near the wall just upstream of the jet exit and wrap around the jet (Krothapalli *et al.*, 1990; Kelso & Smits, 1995). As the horseshoe vortices travel downstream they begin to tilt upward during 'separation events' (Fric & Roshko, 1994) caused by the adverse pressure gradient created as the jet entrains fluid from the boundary layer. This process forms wake vortices that extend up in the wall-normal direction through the jet wake (Fric & Roshko, 1994; Kelso *et al.*, 1996; Eiff *et al.*, 1995; McMahon *et al.*, 1971; Moussa *et al.*, 1977).

Transverse jets are found in many engineering applications. For example, the gas turbine combustor utilizes the JICF for dilution jets (Mahesh *et al.*, 2004). Here the JICF helps reduce the pattern factor of hot combustion gases. The JICF also provides

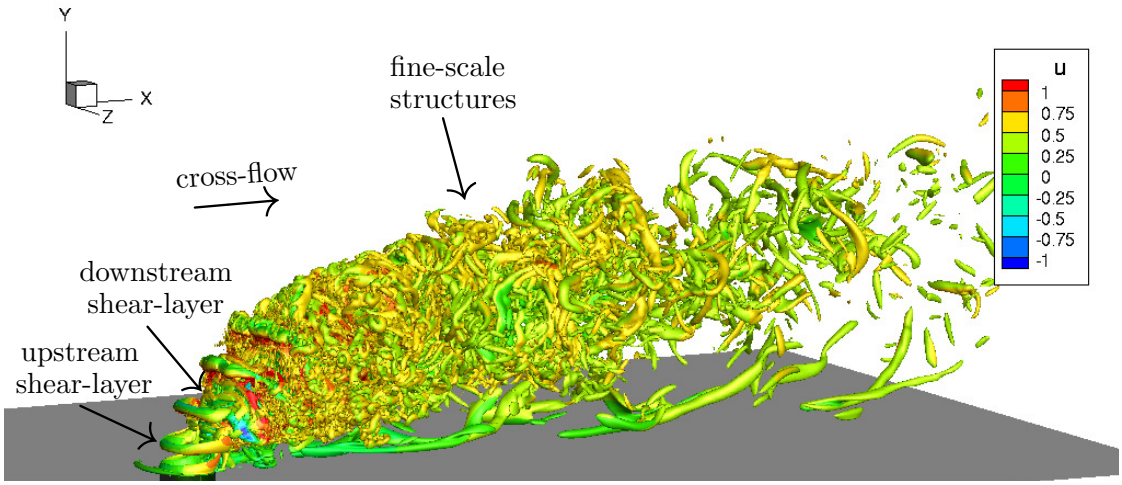

Figure 1.1: The instantaneous turbulent flowfield for a JICF with a jet-to-cross-flow velocity ratio of 2, visualized using isocontours of Q-criterion (eq. 3.1) colored by streamwise velocity u.

significant improvement in injectant mixing, over a free jet. Film cooling also involves transverse jets; here high pressure compressor gases are bled through small holes on turbine blades to shield them from the hot post-combustion gases in the cross-flow. Finally, vertical and/or short take-off and landing (V/STOL) aircraft utilize the JICF for controlled fluidic injection (i.e. thrust vectoring) to replace other control systems, often reducing the overall weight. Reviews by Margason (1993), Karagozian (2010) and Mahesh (2013) compile most of the JICF research, both experimental and computational, over the last seven decades.

The JICF may be characterized by the following parameters: the jet Reynolds number,

$$Re = \overline{v}_{\text{jet}} D/\nu_{\text{jet}}, \tag{1.1}$$

based on the average velocity ($\overline{v}_{\text{jet}}$) at the jet exit, the diameter (D), and the kinematic viscosity of the jet (ν_{jet}); the cross-flow Reynolds number,

$$Re_\infty = u_\infty D/\nu, \tag{1.2}$$

based on the free-stream velocity (u_∞) and kinematic viscosity of cross-flow (ν); and the momentum flux ratio,

$$J = \rho_{\text{jet}}\overline{v}_{\text{jet}}^2/\rho_\infty u_\infty^2, \tag{1.3}$$

where ρ_{jet} and ρ_∞ are the densities of the jet and free-stream, respectively. When the jet and free-stream densities are equal, as in isodensity flows, the jet-to-cross-flow velocity ratio

$$R = \overline{v}_{\text{jet}}/u_\infty, \tag{1.4}$$

is often used. The velocity ratio can also be defined as,

$$R^* = \frac{v_{\text{jet,max}}}{u_\infty} \tag{1.5}$$

based on the maximum velocity at the jet exit. The present work considers low-speed jets in cross-flow that are constant density, so R is used as the characterization parameter (instead of J).

1.2 Review of related past work

Su & Mungal (2004) used planar laser-induced fluorescence (PLIF) to study two-dimensional velocity fields of the JICF for $R = 5.7$ at a Reynolds number of 5000. Due to the 10% higher density of the acetone vapor used to seed the jet fluid, the effective jet to cross-flow ratio (based on momentum)

$$R_{\text{eff}} = \sqrt{\frac{\rho_{\text{jet}}\overline{v}_{\text{jet}}^2}{\rho_\infty u_\infty}}, \tag{1.6}$$

may be computed as 6.008 for the experiments. Su & Mungal (2004) reported profiles of turbulent statistics in the cross-flow-direction at the symmetry plane for different distances from the jet exit ($y = 0.1RD, 0.5RD, 1.0RD$). Muppidi & Mahesh (2007)

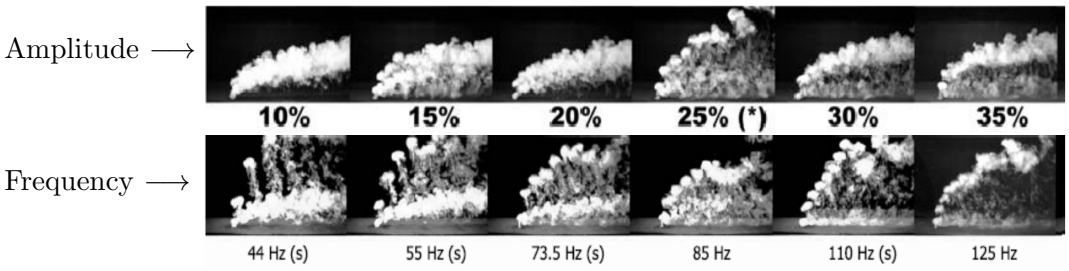

Figure 1.2: Shapiro *et al.* (2006) studied the JICF by acoustically pulsing the jet. By varying either the amplitude or the frequency, jet penetration and mixing can be affected.

performed direct numerical simulation (DNS) for the same JICF parameters. The results showed good agreement with experiment, highlighting that DNS is able to capture the complex turbulent features of the JICF.

Shapiro *et al.* (2006) studied how the JICF responds to different acoustic excitations. Jet penetration and mixing were the main focus of their study, which acoustically pulsed the JICF at $R = 2.4$ and $R = 4$, for $1420 \leq Re \leq 3660$. They found that often a single set of excitation conditions generated vortical structures that greatly improved jet penetration. Some of their results are shown in figure 1.2, which highlights how varying the amplitude or the frequency affects jet penetration. However, optimal jet penetration does not necessarily result in an optimally mixed JICF. They suggest that low frequency excitation (relative to the unforced jet upstream shear-layer frequency) may enhance mixing. This is because subharmonic frequencies resulting from high frequency excitation may cause strong bifurcations of the jet, reducing the degree of injectant distribution and therefore the quantified amount of mixing. Furthermore, Shapiro *et al.* (2006) reported that the optimal forcing conditions for high ($R > 5$) and low ($R < 5$) velocity ratios might depend on the jet regime. This observation is consistent with experiments by Narayanan *et al.* (2003) who show that when $R = 6$, low-amplitude excitation of the JICF can promote mixing. Whereas, M'Closkey *et al.* (2002) and Shapiro *et al.* (2006) have shown that when $R \leq 4$, high-amplitude sinusoidal excitation has little success increasing jet penetration or mixing.

Sau & Mahesh (2010) used DNS to further understand the effect of pulsing on the

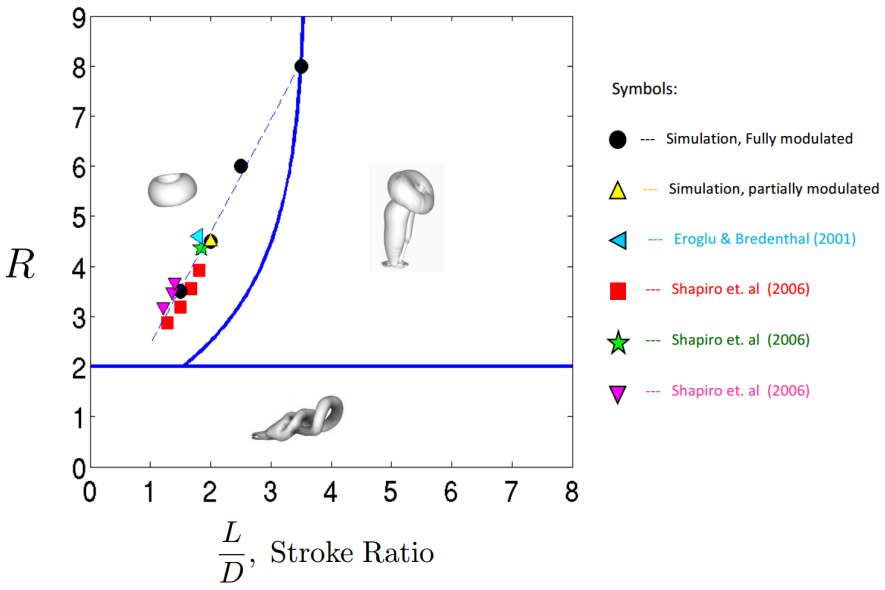

Figure 1.3: Sau & Mahesh (2010) developed this map which shows the pulsed JICF split into three distinct regimes based on R and the stroke ratio. Several different simulations and experiments which exhibit optimal jet penetration for different sets of parameters are plotted and they all collapse onto a single line where vortex rings are ejected from the jet exit.

JICF. They suggested that strong pulsing produced vortex rings whose properties could be characterized in terms of experimental parameters, such as amplitude, frequency and duty cycle. They performed DNS with the same pulse profiles as experiment and showed how the results were identical to those obtained using idealized top-hat profiles. They developed a regime map, shown in figure 1.3, that characterized jet pulsing based on the stroke ratio (L/D) and velocity ratio (R). They demonstrated three distinct JICF regimes in the map: hairpin vortices (small R), vortex rings (small L/D, $R > 2$), vortex rings with trailing shear-layer (large L/D, $R > 2$). The three regimes have different mixing characteristics. Sau & Mahesh (2010) showed that the optimal jet penetration conditions from several different experiments (Shapiro *et al.*, 2006; Eroglu & Breidenthal, 2001), their own DNS, and even zero-net-mass-flux jets (Cater & Soria, 2002) all collapsed along a single line on the regime map.

Megerian *et al.* (2007) showed that the response of the JICF to pulsing depends on the stability of the upstream shear-layer. They performed experiments on the JICF at Re of 2000 and 3000 over the range $1 \leq R \leq 10$. They collected vertical velocity spectra along the upstream shear-layer and observed this region to transition from absolutely to convectively unstable between $R = 2$ and $R = 4$. When $R = 2$, Megerian *et al.* (2007) observed a strong tone in the upstream shear-layer at a single Strouhal number ($St = fD/v_{\text{jet,max}}$), based on the jet exit diameter (D) and the maximum velocity at the jet exit ($v_{\text{jet,max}}$). This disturbance originated near the jet exit and was also observed further downstream. This is consistent with an absolute instability, which grows at the point of origin and travels downstream. Conversely, when $R = 4$, Megerian *et al.* (2007) observed that upstream shear-layer instabilities were weaker and a broader spectrum formed farther downstream. This behavior is consistent with a convective instability, which grows as it travels downstream.

Iyer & Mahesh (2016) performed direct numerical simulations (DNS) reproducing the same stability transition, which they explained by proposing that the upstream shear-layer is a counter-current shear-layer. Their schematic is shown in figure 1.4, where the counter-current shear-layer is identified across the reverse flow upstream, and the jet. According to the classic analysis by Huerre & Monkewitz (1985), the following

velocity ratio characterizes the stability of counter-current mixing layers:

$$\mathcal{R}_{\text{vel}} = \frac{V_1 - V_2}{V_1 + V_2}, \tag{1.7}$$

where V_1 and V_2 are the velocities of the two mixing layers. Huerre & Monkewitz (1985) show that for $\mathcal{R}_{\text{vel}} > 1.315$ a mixing layer is absolutely unstable, whereas if $\mathcal{R}_{\text{vel}} < 1.315$ the mixing layer is convectively unstable. Iyer & Mahesh (2016) calculated $\mathcal{R}_{\text{vel}}$ from their simulations for $R = 2$ and $R = 4$. The mixing layer velocities were taken as the maximum and minimum (most negative) vertical velocities across the upstream shear-layer of the turbulent mean flows. The locations where $\mathcal{R}_{\text{vel}}$ was extracted for each case can be identified using the symmetry plane contour plots (figure 1.5), where only the negative vertical velocity contours are shown. Iyer & Mahesh (2016) found that $\mathcal{R}_{\text{vel}} = 1.44$ and $\mathcal{R}_{\text{vel}} = 1.20$ for $R = 2$ and $R = 4$, respectively. This suggests that the mechanism that drives the stability for free shear-layers may also drive stability characteristics for complex flows like the JICF.

Alves *et al.* (2008) have studied the stability of JICFs using local linear stability analysis. They study the spatial stability of two different baseflows; a modified version of the potential flow solution by Coelho & Hunt (1989) and continuous velocity model based on the same potential flow solution (valid for larger values of Strouhal number). In their analysis they prescribe a temporal wavenumber, ω, which is real (i.e. zero growth rate), and solve for the complex spatial wavenumber, α. Although the JICF upstream shear-layer is locally parallel at certain locations, global stability analysis would provide a more rigorous study of the JICF stability characteristics.

The global linear stability of the JICF has been studied by Bagheri *et al.* (2009), which marks one of the first simulation-based Tri-Global linear stability analysis of a fully three-dimensional baseflow. From this point on, linear stability analysis will refer to Tri-Global linear stability analysis unless otherwise specified. Bagheri *et al.* (2009) studied the stability of the JICF at a jet-to-cross-flow velocity ratio $R^* = 3$ (eq. 1.5), with a Reynolds number $Re_{\delta_0^*} = U_\infty \delta_0^* / \nu = 165$, based on the displacement thickness δ_0^* at the inlet of the cross-flow, or equivalently $Re_{cf} = D u_\infty / \nu_\infty = 495$, based on the jet

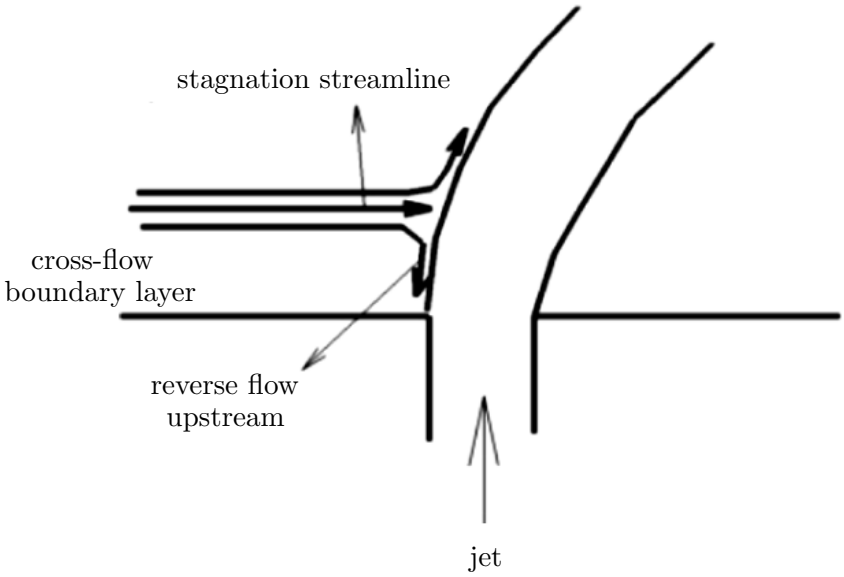

Figure 1.4: Iyer & Mahesh (2016) proposed this schematic representation of the JICF to aid in identifying the counter-current shear-layer made up of the reverse flow upstream and the jet.

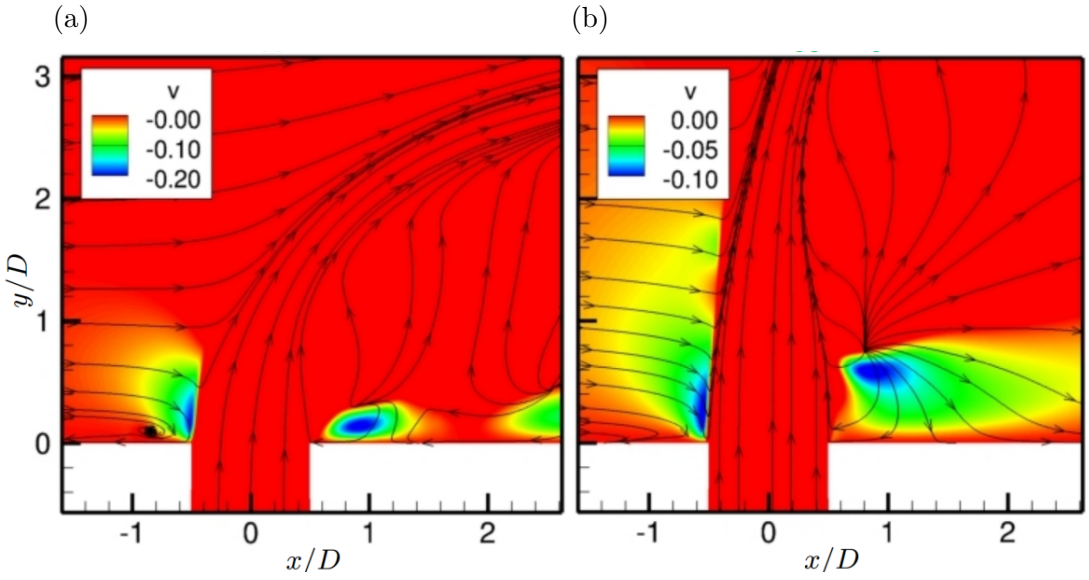

Figure 1.5: Iyer & Mahesh (2016) computed the counter-current velocity ratios for jet-to-cross-flow ratios of (a) 2 and (b) 4 using the most negative vertical velocity in the reverse flow region (see figure 1.4) and the jet fluid velocity.

exit diameter D. The steady baseflow at this value of R^* was obtained using selective frequency damping (SFD) (Akervik *et al.*, 2006). The jet nozzle was not included in their simulation. Instead, a parabolic velocity profile from pipe Poiseuille flow was imposed at the jet exit. Unstable high-frequency modes associated with the upstream shear-layer as well as lower frequency wake modes were identified in their work. Additionally, it was shown that the shedding frequency for the upstream shear-layer was not far from the non-linear shedding frequency. However, the linear wake mode frequency was far from the non-linear wake frequency. Bagheri *et al.* (2009) suggested that the differences in shedding frequencies could be related to the differences between the SFD solution and the time-averaged solution. Peplinski *et al.* (2015) extended the analysis of Bagheri *et al.* (2009) to include $R^* = 1.5$ and $R^* = 1.6$. Peplinski *et al.* (2015) used modal and non-modal linear analyses to study the JICF. They observed an almost identical wavepacket develop for the stable ($R^* = 1.5$) and unstable ($R^* = 1.6$) cases, and were able to determine the bifurcation point of R^* to lie between 1.5 and 1.6.

1.3 Overview

The focus of this dissertation is to further the understanding of the stability and sensitivity of the JICF using linear stability, adjoint sensitivity, and optimal perturbation analyses. Understanding the dominant flow instability mechanisms, and how they are most sensitive to velocity perturbations will help control of the JICF in engineering applications. Jet-to-cross-flow ratios of 2 and 4 at $Re = 2000$ are chosen, to straddle the upstream shear-layer stability transition observed by Megerian *et al.* (2007). The upstream shear-layer transition is important since optimizing jet penetration and mixing is shown to be highly dependent on the stability of the shear-layer (Megerian *et al.*, 2007; Sau & Mahesh, 2010).

Linear stability analysis determines the dominant eigenvalues and eigenmodes of the linearized Navier-Stokes equations. This provides information about the dominant instability modes at asymptotic times. Similarly, adjoint sensitivity analysis solves for the dominant eigenvalues and eigenmodes of the adjoint to the linearized Navier-Stokes

equations, which yield the dominant sensitivity modes that correspond to the linear stability modes. Finally, optimal perturbation analysis studies the direct and adjoint to the linearized equations in tandem over different time horizons to determine the 'most dangerous' perturbations. This provides insight into the initial conditions that generate the most energy growth over different time-scales.

This research represents state-of-the-art stability and sensitivity analyses of three-dimensional turbulent mean flows of the JICF. An unstructured finite volume algorithm that ensures discrete kinetic energy conservation (Mahesh *et al.*, 2004) is used to perform the analyses. The combination of the numerics and high-performance computing platforms allows for high-fidelity stability and sensitivity results to be attained.

The main contributions of this dissertation are:

(i) A novel computational capability was developed, for linear stability, adjoint sensitivity, and optimal perturbation analyses of fully three-dimensional baseflows with no homogeneous directions. The framework utilizes unstructured grids and is massively parallel, with robust and high-fidelity numerical methods. This allows the analyses to be performed for a wide variety of flowfields, including the JICF.

(ii) Global linear stability and adjoint sensitivity analyses of the JICF, both capture unstable eigenmodes associated with the upstream shear-layer, with frequencies matching those observed in experiment and simulation. Additionally, dynamic mode decomposition of the non-linear turbulent DNS flowfield shows good qualitative agreement with the linear stability eigenmodes, highlighting their relevance to the dynamics of the turbulent flowfield.

(iii) The upstream shear-layer instability mode is shown to have the largest growth rate when $R = 2$. Conversely, when $R = 4$, the downstream shear-layer eigenmode is shown to have a larger growth rate than the upstream shear-layer instability. The downstream shear-layer is often overlooked; this result shows that for higher values of R, the stability of the downstream shear-layer is significant to the overall dynamics.

(iv) The JICF is shown to have unstable linear stability and adjoint eigenmodes that ride along the CVP and are not symmetric across the mid-plane. These asymmetric modes have larger relative growth rates at higher jet-to-cross-flow velocity ratios, suggesting that they are more relevant to the overall dynamics at higher R. Asymmetries have been observed in mean CVP cross-sections from experiments at higher jet-to-cross-flow ratios; consistent with the asymmetric eigenmode results, which suggest increased sensitivity to experimental asymmetries at higher velocity ratios.

(v) The wavemaker, which highlights regions that are most sensitive to localized feedback, is qualitatively different for $R = 2$ and $R = 4$. When $R = 2$, the wavemaker is a compact region near the origin of the upstream shear-layer along the upstream side of the jet nozzle exit. For $R = 4$, the wavemaker extends several jet diameters along the upstream shear-layer. The difference between the spatial distributions of the wavemaker regions is consistent with the upstream shear-layer region, as it transitions from absolutely to convectively unstable between $R = 2$ and $R = 4$.

(vi) Wavemaker analysis of the downstream shear-layer region for higher jet-to-cross-flow velocity ratios ($R = 4$) reveals a compact region of localized feedback. This region resembles the compact wavemaker shape of the absolutely unstable upstream shear-layer for $R = 2$; suggesting the downstream shear-layer region may be absolutely unstable when $R = 4$. This implies that as R increases further, there is some R_{crit}, such that the downstream shear-layer region becomes convectively unstable, just as a free jet ($R = \infty$) is convectively unstable.

(vii) Low-frequency linear stability eigenmodes extend far downstream with longer spatial length scales (compared to the upstream shear-layer eigenmodes) along the jet path. Additionally, there are fluid structures downstream near the wall which resemble wake vortices. The adjoint analysis shows that when $R = 2$, the low-frequency modes are most sensitive, above and around the upstream side of the jet nozzle exit. For $R = 4$, this sensitivity region is similar, but extends a couple of jet diameters upstream into the cross-flow boundary layer - highlighting the

sensitivity to perturbations in the cross-flow boundary layer.

(viii) Optimal perturbation analysis of the JICF reveals several points where the optimal perturbations change, depending on the optimization time relative to the characteristic time-scale of the upstream shear-layer. For case $R2$, short-time-scale optimal perturbations generate energy asymmetrically at the formation region of the CVP. As the optimization times are increased to the characteristic-time, perturbations to the downstream shear-layer dominate. For long-times, the optimal perturbations switch to the upstream shear-layer, as well as hybrid modes that perturb the upstream and downstream shear-layers, simultaneously. For case $R4$, short- and characteristic-time scale perturbation growth are focused along the downstream shear-layer. For longer time-scales, the upstream shear-layer becomes optimal. Furthermore, hybrid perturbations dominate the longest time-scales for case $R4$.

(ix) The optimal perturbations reveal the effects of the non-normality of the linearized Navier-Stokes operator for the JICF. For long time horizons, the optimal perturbations utilize paths which generate energy growth along both the upstream and downstream shear-layers for $R = 2$ and $R = 4$.

The dissertation is organized as follows. Chapter 2 highlights the governing equations, algorithm, and the different stability and sensitivity analyses performed. Validation of the different analyses is discussed in detail in Chapter 3. Chapters 4, 5, and 6 show the results from the application of linear stability, adjoint sensitivity, and optimal perturbation analyses for the JICF. A summary of the conclusions is provided in Chapter 7.

Chapter 2

Numerical Methodology

This chapter is organized such that §2.1 describes the governing equations and numerical algorithm, §2.2 describes the numerics for linear stability analysis, followed by adjoint sensitivity analysis in §2.3 and optimal perturbation analysis in §2.4.

2.1 Governing equations and numerical algorithm

The Navier-Stokes (N-S) equations for single-phase, constant density, incompressible, Newtonian fluid motion in an inertial reference frame are:

$$\begin{aligned} \frac{\partial \boldsymbol{u}_i}{\partial t} + \frac{\partial}{\partial x_j}\boldsymbol{u}_i\boldsymbol{u}_j &= -\frac{\partial p}{\partial x_i} + \nu\frac{\partial^2 \boldsymbol{u}_i}{\partial x_j \partial x_j}, \\ \frac{\partial \boldsymbol{u}_i}{\partial x_i} &= 0. \end{aligned} \tag{2.1}$$

Here, t, $\boldsymbol{u}_i(x,y,z)$, $p(x,y,z)$, and ν are the time, velocity vector, pressure, and kinematic viscosity of the fluid, respectively. For constant fluid density, the density may be combined with the pressure term.

Directly solving the Navier-Stokes equations (eq. 2.1) quickly becomes expensive for complex flows. Therefore, various assumptions are employed to ease the computational burden. The most common forms include the Reynolds-averaged N-S (RANS) and Large-Eddy Simulation (LES) methodologies. In this dissertation, unless otherwise

specified, DNS is used. Combining robust numerical methods with state-of-the-art computational resources allows for the capture of high Reynolds number flows with the utmost fidelity. Upwinding schemes (often used to solve the RANS equations) provide stability and robustness to simulations by adding numerical dissipation. One way to mitigate this issue to to use numerical schemes that ensure the discrete energy conservation of first- and second-order quantities. This allows for the simulation of complex flows at high Reynolds numbers without added numerical dissipation.

In this dissertation, an unstructured, finite-volume algorithm developed by Mahesh *et al.* (2004) is used to solve the N-S equations 2.1. The spatial discretization emphasizes the simultaneous conservation of discrete first-order quantities (i.e. momentum) in addition to second-order quantities, such as kinetic energy. In other words, $\sum \boldsymbol{u}_i \partial \left(\boldsymbol{u}_i \boldsymbol{u}_j\right) / \partial x_j$ over all control volumes only has contributions from the boundary elements. In this method, Cartesian velocities, u_i, and pressure, p, are stored at the control volume (CV) centroid. Additionally, face-normal velocities, v_n, are stored separately at the centroids of the faces. The algorithm has been validated and used to simulate a variety of complex flows, including: a gas turbine combustor (Mahesh *et al.*, 2004), free jet entrainment (Babu & Mahesh, 2004), and transverse jets (Muppidi & Mahesh, 2005, 2007, 2008; Sau & Mahesh, 2007, 2008; Iyer & Mahesh, 2016; Regan & Mahesh, 2017), flow over hulls (Chang *et al.*, 2011; Mahesh *et al.*, 2015) and propellers in crashback (Verma *et al.*, 2012; Jang & Mahesh, 2013).

A fractional-step (sometimes called predictor-corrector) method is used to solve the governing equations (eq. 2.1). Time is advanced explicitly using the Adams-Bashforth second-order scheme for the predictor velocities, u_i^*, through the momentum equation using two previous time steps, k and $k-1$:

$$\frac{\boldsymbol{u}_i^* - \boldsymbol{u}_i^k}{\Delta t} = \frac{1}{2}\left[3\left(NL + VISC\right)^k - \left(NL + VISC\right)^{k-1}\right], \tag{2.2}$$

where NL and $VISC$ denote the non-linear convective term and the viscous term, respectively. The predicted velocities are then interpolated using second-order symmetric

averaging to obtain the predicted face-normal velocities as:

$$v_n^* = \left[\frac{\boldsymbol{u}_{i,\mathrm{cv1}}^* + \boldsymbol{u}_{i,\mathrm{cv2}}^*}{2}\right] n_i, \tag{2.3}$$

A Poisson equation for pressure is then derived by taking the divergence of the momentum equation and satisfying continuity. This is used in a corrector step to project the solution onto a divergence-free velocity field. The correction step is written as:

$$\frac{\boldsymbol{u}_i^{k+1} - \boldsymbol{u}_i^*}{\Delta t} = -\frac{\partial p^{k+1}}{\partial x_i}, \tag{2.4}$$

which is projected to the face-normal,

$$\frac{v_n^{k+1} - v_n^*}{\Delta t} = -\frac{\partial p^{k+1}}{\partial n}. \tag{2.5}$$

Mass conservation states that,

$$\frac{\partial \boldsymbol{u}_i}{\partial x_i} = 0 \Longrightarrow \sum_{\text{faces}} v_n^{k+1} A_f = 0, \tag{2.6}$$

where A_f is the face area. After using eq. 2.6, eq. 2.5 reveals the Poisson equation for p^{k+1}:

$$\begin{aligned} \sum_{\text{faces}} v_n^{k+1} A_f - \sum_{\text{faces}} v_n^* A_f &= -\Delta t \sum_{\text{faces}} \frac{\partial p^{k+1}}{\partial n} A_f, \\ \Longrightarrow \Delta t \sum_{\text{faces}} \frac{\partial p^{k+1}}{\partial n} A_f &= \sum_{\text{faces}} v_n^* A_f, \end{aligned} \tag{2.7}$$

The Poisson equation is solved using the Algebraic Multi-Grid (AMG) solver available in the HYPRE library (Falgout & Yang, 2002). After solving for p^{k+1}, $\boldsymbol{u}_i^{k+1}$ and v_n^{k+1} are computed from equations 2.4 and 2.5, respectively.

2.2 Linear Stability Analysis

Modal linear stability analysis is the study of the dynamic response of a base state (i.e. baseflow) subject to external perturbations (see Theofilis (2011) for review). In this dissertation, the incompressible Navier-Stokes equations (eq. 2.1) are linearized about a base state $\overline{\boldsymbol{u}}_i$ and $\overline{p}$. The base state can be assumed to vary arbitrarily in space:

$$\begin{aligned} \overline{\boldsymbol{u}}_i &= \overline{\boldsymbol{u}}_i\left(x,y,z\right) = \left[\overline{u},\overline{v},\overline{w}\right]^{\mathrm{T}}, \\ \overline{p} &= \overline{p}\left(x,y,z\right), \end{aligned} \tag{2.8}$$

where $(\cdot)^{\mathrm{T}}$ denotes a vector transpose. If the flow field is decomposed into a base state subject to a small $O(\varepsilon)$ perturbation,

$$\boldsymbol{u}_i = \overline{\boldsymbol{u}}_i + \varepsilon\tilde{\boldsymbol{u}}_i, \qquad p \;\; = \overline{p} + \varepsilon\tilde{p}, \tag{2.9}$$

the governing equations may be rewritten as:

$$\begin{aligned} \frac{\partial\left(\overline{\boldsymbol{u}}_i + \varepsilon\tilde{\boldsymbol{u}}_i\right)}{\partial t} + \frac{\partial}{\partial x_j}\left(\overline{\boldsymbol{u}}_i + \varepsilon\tilde{\boldsymbol{u}}_i\right)\left(\overline{\boldsymbol{u}}_j + \varepsilon\tilde{\boldsymbol{u}}_j\right) &= -\frac{\partial\left(\overline{p} + \varepsilon\tilde{p}\right)}{\partial x_i} + \nu\frac{\partial^2\left(\overline{\boldsymbol{u}}_i + \varepsilon\tilde{\boldsymbol{u}}_i\right)}{\partial x_j \partial x_j} \\ \frac{\partial\left(\overline{\boldsymbol{u}}_i + \varepsilon\tilde{\boldsymbol{u}}_i\right)}{\partial x_i} &= 0. \end{aligned} \tag{2.10}$$

and linearized by neglecting the ε^2 terms. Additionally, the base state is a solution to the incompressible Navier-Stokes equations (eq. 2.1). Subtracting the baseflow equations yields the linearized Navier-Stokes (LNS) equations:

$$\begin{aligned} \frac{\partial\tilde{\boldsymbol{u}}_i}{\partial t} + \frac{\partial}{\partial x_j}\tilde{\boldsymbol{u}}_i\overline{\boldsymbol{u}}_j + \frac{\partial}{\partial x_j}\overline{\boldsymbol{u}}_i\tilde{\boldsymbol{u}}_j &= -\frac{\partial\tilde{p}}{\partial x_i} + \nu\frac{\partial^2\tilde{\boldsymbol{u}}_i}{\partial x_j \partial x_j}, \\ \frac{\partial\tilde{\boldsymbol{u}}_i}{\partial x_i} &= 0. \end{aligned} \tag{2.11}$$

subject to the following boundary and initial conditions:

$$\tilde{\boldsymbol{u}}(\boldsymbol{x}, t=0) = \tilde{\boldsymbol{u}}_0 \neq 0 \quad , \quad \tilde{\boldsymbol{u}}(S,t) = 0, \tag{2.12}$$

where S is the boundary of the spatial domain. In vector notation:

$$\begin{gathered}\frac{\partial \tilde{\boldsymbol{u}}}{\partial t}+\left(\overline{\boldsymbol{u}}\cdot\nabla\right)\tilde{\boldsymbol{u}}+\left(\nabla\overline{\boldsymbol{u}}\right)\cdot\tilde{\boldsymbol{u}}=-\nabla\tilde{p}+\nu\Delta\tilde{\boldsymbol{u}},\\ \nabla\cdot\tilde{\boldsymbol{u}}=0.\end{gathered} \tag{2.13}$$

Note that the same numerical techniques are used to solve the LNS equations (eq. 2.11) and the N-S equations (eq. 2.1). A molecular viscosity is used to perform linear stability analysis since the same was used to obtain the baseflow obtained by DNS.

The LNS equations (eq. 2.11) may be rewritten as a system of linear equations,

$$\frac{\partial \tilde{\boldsymbol{u}}_i}{\partial t}=\boldsymbol{A}\tilde{\boldsymbol{u}}_i, \tag{2.14}$$

where $\boldsymbol{A}$ is the LNS operator and $\tilde{\boldsymbol{u}}_i$ is the divergence-free velocity perturbation field. In modal linear stability analysis, our interest is in the long-time behavior of $\tilde{\boldsymbol{u}}_i$. Consequently, the solutions to the linear system of equations (eq. 2.14) are of the form:

$$\tilde{\boldsymbol{u}}_i\left(x,y,z,t\right)=\sum_{\omega}\hat{\boldsymbol{u}}_i\left(x,y,z\right)e^{\omega t}+\text{c.c}, \tag{2.15}$$

where ω and $\hat{\boldsymbol{u}}_i$ can be complex. This defines $\text{Re}\left(\omega\right)$ as the growth/damping rate and $\text{Im}\left(\omega\right)$ as the temporal frequency of the complex velocity coefficient ($\hat{\boldsymbol{u}}_i$). Substituting eq. 2.15 into the LNS system (eq. 2.14) and invoking orthogonality transforms the system of equations into a linear eigenvalue problem,

$$\boldsymbol{\Omega}\hat{\boldsymbol{U}}_i=\boldsymbol{A}\hat{\boldsymbol{U}}_i, \tag{2.16}$$

where $\omega_j=\text{diag}\left(\boldsymbol{\Omega}\right)_j$ is the j-th eigenvalue and $\hat{\boldsymbol{u}}_i^j=\boldsymbol{U}_i[j,:]$ is the j-th eigenvector (i.e. eigenmode).

2.2.1 Solutions of the LNS equations

For linear stability analysis, the size of the eigenvalue problem (eq. 2.16) can be $O(10^6-10^8)$. This makes solving the eigenvalue problem using direct methods very computationally expensive, often prohibitively so. Instead, an extension of the Arnoldi iteration method (Arnoldi, 1951) called the Implicitly Restarted Arnoldi Method (IRAM) is used, which is a matrix-free method. The present work uses the IRAM implemented in the P_ARPACK library (Lehoucq *et al.*, 1997) to efficiently calculate the leading (i.e. most unstable) eigenvalues and their associated eigenmodes.

A temporal exponential transformation of the eigenvalue spectrum is performed. This transforms the most unstable eigenvalues into the most dominant (i.e. largest magnitude) eigenvalues, which P_ARPACK can solve for efficiently. To do this, the eigenvalue problem (eq. 2.16) is integrated over some time, τ:

$$\int_0^\tau \boldsymbol{\Omega}\hat{\boldsymbol{U}}_i \,\mathrm{d}t = \int_0^\tau \boldsymbol{A}\hat{\boldsymbol{U}}_i \,\mathrm{d}t. \tag{2.17}$$

This yields the exponential of the eigenvalue problem (eq. 2.16):

$$\mathrm{e}^{\boldsymbol{\Omega}\tau}\hat{\boldsymbol{U}}_i = \mathrm{e}^{\boldsymbol{A}\tau}\hat{\boldsymbol{U}}_i. \tag{2.18}$$

which can be rewritten as:

$$\boldsymbol{\Sigma}\hat{\boldsymbol{U}}_i = \boldsymbol{B}\hat{\boldsymbol{U}}_i, \tag{2.19}$$

where $\sigma_j = \mathrm{diag}\,(\boldsymbol{\Sigma})_j$. The matrix exponential $\boldsymbol{B} = \mathrm{e}^{\boldsymbol{A}\tau}$ is a time integration operator, which represents a numerical simulation of the LNS equations (eq. 2.11) over time τ. This method is therefore described as a time-stepper method. Note that the eigenvectors, $\hat{\boldsymbol{U}}_i$, are the same between the two eigenvalue problems (eq. 2.16, 2.19). However, the eigenvalues of the original problem (eq. 2.16) must be recovered using the following relationship:

$$\omega_j = \frac{1}{\tau}\ln\sigma_j. \tag{2.20}$$

2.2.2 Time horizon

When using a time-stepper method, the choice of integration time τ depends on the time scales of interest for the problem at hand. It is imperative that τ be less than t_s, the smallest time scales of interest; usually $\tau = t_s/2$ is appropriate. For capturing the largest time scales of interest, t_L, the number of Arnoldi vectors N_A is important. Once τ is determined, the number of Arnoldi vectors must be greater than t_L/τ; usually $N_A > 2t_L/\tau$ is appropriate. Overall, some knowledge of the range of time scales is needed to effectively use the IRAM in conjunction with a time-stepper method. Additionally, performing stability analysis on problems with a large range of time scales can drastically affect the computational cost and storage requirements as each Arnoldi vector must be stored for each Arnoldi iteration.

2.2.3 Scaling

The algorithm discussed in §2.1 has been tested for scaling in the past for DNS and LES. In this section, scaling simulations are performed using the same algorithm, but for the LNS (eq. 2.11). The scaling was performed using Comet, a part of the San Diego Supercomputer Center (SDSC), which uses 2.5GHz Intel Haswell processor cores and an InfiniBand interconnect. Strong scaling, where the number of processors are increased for a constant grid, is shown in figure 2.1, with corresponding data given in table 2.1. Similarly, weak scaling, where processor loading is held constant for different numbers of processors, is shown in figure 2.2 for a constant loading of 83,000 grid elements. The corresponding weak scaling data is shown in table 2.2. The scaling study concludes that the global linear stability analysis code scales up to thousands of cores with approximately 83,000 elements per core.

2.2.4 Rotating reference frame

The LNS equations were extended to rotating reference frames, which allow efficient description of problems such as rotors and propellers. The rotational reference frame

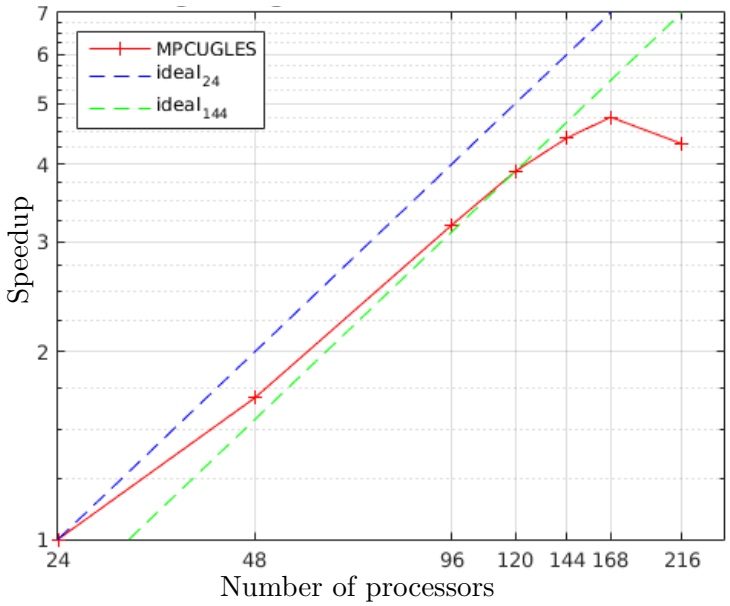

Figure 2.1: Strong scaling of global linear stability analysis of the 3D lid-driven cavity tested on Comet.

number of processors	time per iteration
24	1.343
48	0.796
96	0.421
120	0.345
144	0.305
168	0.282
216	0.312

Table 2.1: Strong scaling performed on Comet (Intel Haswell, 2.5 GHz) for linear stability analysis of the 3D lid-driven cavity. A representative time step is chosen to calculate the time taken for one time step.

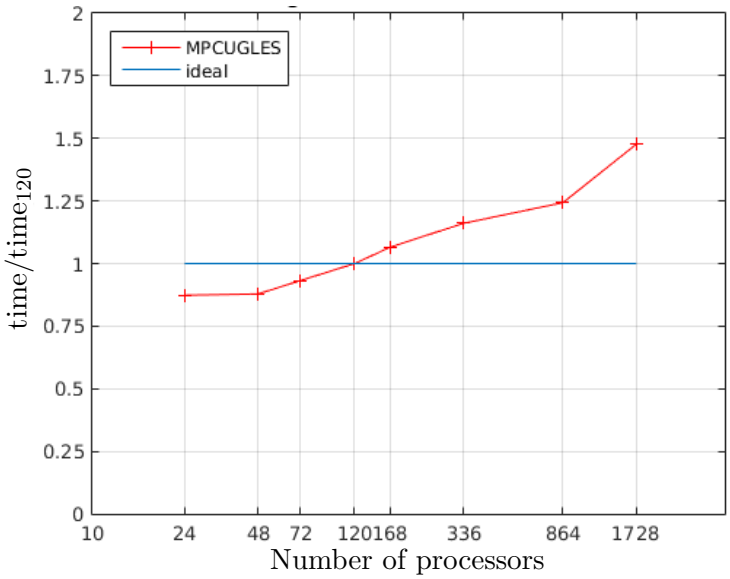

Figure 2.2: Weak scaling of global linear stability analysis of the 3D lid-driven cavity tested on Comet.

number of processors	grid size (in millions)	time per iteration
24	2	0.118
48	4	0.119
72	6	0.126
120	10	0.135
168	14	0.144
336	28	0.157
864	72	0.168
1728	144	0.199

Table 2.2: Weak scaling performed on Comet (Intel Haswell, 2.5 GHz) for linear stability analysis of the 3D lid-driven cavity. A representative time step is chosen to calculate the time taken for one time step. The loading for each processor is held constant at 83,000 grid elements.

governing equations are validated in §3.1.5, but are not used elsewhere in this dissertation. The rotating reference frame LNS equations are written as:

$$\begin{aligned} \frac{\partial \tilde{\boldsymbol{u}}_i}{\partial t} + \frac{\partial}{\partial x_j}\tilde{\boldsymbol{u}}_i\overline{\boldsymbol{u}}_j - \frac{\partial}{\partial x_j}\tilde{\boldsymbol{u}}_i\Omega_k x_l \epsilon_{jkl} + \frac{\partial}{\partial x_j}\overline{\boldsymbol{u}}_i\tilde{\boldsymbol{u}}_j &= -\frac{\partial \tilde{p}}{\partial x_i} - \Omega_j \tilde{\boldsymbol{u}}_k \epsilon_{ijk} + \nu \frac{\partial^2 \tilde{\boldsymbol{u}}_i}{\partial x_j \partial x_j}, \\ \frac{\partial \tilde{\boldsymbol{u}}_i}{\partial x_i} &= 0. \end{aligned} \tag{2.21}$$

where $\tilde{\boldsymbol{u}}_i$ is the inertial perturbation velocity in the inertial frame, $\overline{\boldsymbol{u}}_i$ is the inertial baseflow velocity in the inertial frame, p is the pressure, and x_i is the coordinate vector in the rotating and non-inertial frame of reference, Ω_j is the angular velocity of the reference frame, and ϵ_{ijk} is the permutation tensor. The new term on the left-hand-side (LHS) accounts for the Coriolis acceleration, and the added right-hand-side (RHS) term adds the centrifugal acceleration due to rotation. Note that the velocities are inertial while the grid rotates with angular velocity Ω_j. By substituting $\Omega_j = 0$ into eq. 2.21, the inertial equations (eq. 2.11) are recovered.

2.3 Adjoint sensitivity analysis

Adjoint techniques have been shown to be extremely useful in many fluid mechanics applications involving laminar-to-turbulent transition, receptivity, sensitivity, acoustics, and control. The adjoint of a linear operator can be defined using the generalized Green's theorem (Morse & Feshbach, 1953). In this dissertation, the continuous adjoint to the LNS equations are defined in the same way as Hill (1995) and Giannetti & Luchini (2007) (and similar to Barkley *et al.* (2008)); using the generalized Lagrange identity (Ince, 1926). First, a vector inner product is chosen, which is used to quantify the magnitude of a perturbation, continuously or discretely:

$$(\boldsymbol{u}, \boldsymbol{v}) = \iiint_V \boldsymbol{u}^{\mathrm{T}}\boldsymbol{v}\ \mathrm{d}x\,\mathrm{d}y\,\mathrm{d}z = \int_\Omega \boldsymbol{u}^{\mathrm{T}}\boldsymbol{v}\ \mathrm{d}\Omega \Longrightarrow \sum_{i=1}^{\mathrm{ncv}} \boldsymbol{u}^{\mathrm{T}}\boldsymbol{v} V_{\mathrm{cv}}, \tag{2.22}$$

where Ω is the computational volume, $\boldsymbol{u}$ and $\boldsymbol{v}$ are arbitrary vector quantities, ncv is the total number of control volumes, and V_{cv} is the CV volume. When considering the

set of governing equations, it is easier to express the primitive variables as $\boldsymbol{q} = \{\tilde{\boldsymbol{u}}, p\}$, and the associated adjoint as $\boldsymbol{q}^\dagger = \{\tilde{\boldsymbol{u}}^\dagger, p^\dagger\}$. The combination of the space and time domains, $\Gamma = \Omega \times (0, \tau)$, defines the domain for the governing equations. Therefore, the inner product associated with Γ is:

$$\left\langle \boldsymbol{q}, \boldsymbol{q}^\dagger \right\rangle = \int_0^\tau \iiint_V \boldsymbol{q}^{\mathrm{T}} \boldsymbol{q}^\dagger \, \mathrm{d}x \, \mathrm{d}y \, \mathrm{d}z \, \mathrm{d}t = \int_0^\tau \int_\Omega \boldsymbol{q}^{\mathrm{T}} \boldsymbol{q}^\dagger \, \mathrm{d}\Omega \, \mathrm{d}t = \int_\Gamma \boldsymbol{q}^{\mathrm{T}} \boldsymbol{q}^\dagger \, \mathrm{d}\Gamma. \tag{2.23}$$

It is also useful to compactly write out the LNS as

$$\mathcal{A} = \begin{bmatrix} \frac{\partial}{\partial t} + (\overline{\boldsymbol{u}} \cdot \nabla) + (\nabla \overline{\boldsymbol{u}}) \cdot & -\nu\Delta & , & \nabla \\ & \nabla\cdot & , & 0 \end{bmatrix}, \tag{2.24}$$

which allows the LNS to be compactly written as:

$$\mathcal{A}\boldsymbol{q} = 0. \tag{2.25}$$

$\mathcal{A}^\dagger$ is then defined as the adjoint of $\mathcal{A}$ for the inner product (eq. 2.23):

$$\mathcal{A}^\dagger = \begin{bmatrix} -\frac{\partial}{\partial t} + (\overline{\boldsymbol{u}} \cdot \nabla) - (\nabla \overline{\boldsymbol{u}})^{\mathrm{T}} \cdot & -\nu\Delta & , & \nabla \\ & \nabla\cdot & , & 0 \end{bmatrix}. \tag{2.26}$$

The Lagrange identity states that for any suitably differentiable fields $\boldsymbol{q}$ and $\boldsymbol{q}^\dagger$, the following must be satisfied (note that $\boldsymbol{q}$ is not required to satisfy the LNS equations (eq. 2.11) for the identity to hold true):

$$\left\langle \mathcal{A}\boldsymbol{q}, \boldsymbol{q}^\dagger \right\rangle - \left\langle \boldsymbol{q}, \mathcal{A}^\dagger \boldsymbol{q}^\dagger \right\rangle = 0. \tag{2.27}$$

For $\mathcal{A}^\dagger$ to be the adjoint of $\mathcal{A}$, the above identity must hold. Expanding the above equation and then integrating by parts gives:

$$\begin{aligned} 0 = \int_\Gamma \left[\left(\frac{\partial \tilde{\boldsymbol{u}}}{\partial t} + (\overline{\boldsymbol{u}} \cdot \nabla)\, \tilde{\boldsymbol{u}} + (\nabla \overline{\boldsymbol{u}}) \cdot \tilde{\boldsymbol{u}} - \nu \Delta \tilde{\boldsymbol{u}} \right)^{\mathrm{T}} \tilde{\boldsymbol{u}}^\dagger + (\nabla \cdot \tilde{\boldsymbol{u}})\, \tilde{p}^\dagger \right] \, \mathrm{d}\Gamma - \\ \int_\Gamma \left[\tilde{\boldsymbol{u}}^{\mathrm{T}} \left(-\frac{\partial \tilde{\boldsymbol{u}}^\dagger}{\partial t} + (\overline{\boldsymbol{u}} \cdot \nabla)\, \tilde{\boldsymbol{u}}^\dagger - (\nabla \overline{\boldsymbol{u}})^{\mathrm{T}} \cdot \tilde{\boldsymbol{u}}^\dagger - \nu \Delta \tilde{\boldsymbol{u}}^\dagger \right) + \tilde{p} \left(\nabla \cdot \tilde{\boldsymbol{u}}^\dagger \right) \right] \, \mathrm{d}\Gamma \\ = \int_\Gamma -\frac{\partial}{\partial t} \left(\tilde{\boldsymbol{u}} \cdot \tilde{\boldsymbol{u}}^\dagger \right) \, \mathrm{d}\Gamma + \\ \int_\Gamma \nabla \cdot \left[-\overline{\boldsymbol{u}} \left(\tilde{\boldsymbol{u}} \cdot \tilde{\boldsymbol{u}}^\dagger \right) + \tilde{\boldsymbol{u}} \tilde{p}^\dagger + \tilde{\boldsymbol{u}}^\dagger \tilde{p} + \nu \left((\nabla \tilde{\boldsymbol{u}})^{\mathrm{T}} \cdot \tilde{\boldsymbol{u}}^\dagger - \left(\nabla \tilde{\boldsymbol{u}}^\dagger \right)^{\mathrm{T}} \cdot \tilde{\boldsymbol{u}} \right) \right] \, \mathrm{d}\Gamma. \end{aligned} \tag{2.28}$$

Using the divergence theorem, the RHS may be expressed using only domain boundary terms:

$$\begin{aligned} 0 = \int_\Omega \left[\tilde{\boldsymbol{u}} \cdot \tilde{\boldsymbol{u}}^\dagger \right]_0^\tau \, \mathrm{d}\Omega + \\ \int_0^\tau \oint_S \hat{\boldsymbol{n}} \cdot \left[-\overline{\boldsymbol{u}} \left(\tilde{\boldsymbol{u}} \cdot \tilde{\boldsymbol{u}}^\dagger \right) + \tilde{\boldsymbol{u}} \tilde{p}^\dagger + \tilde{\boldsymbol{u}}^\dagger \tilde{p} + \nu \left((\nabla \tilde{\boldsymbol{u}})^{\mathrm{T}} \cdot \tilde{\boldsymbol{u}}^\dagger - \left(\nabla \tilde{\boldsymbol{u}}^\dagger \right)^{\mathrm{T}} \cdot \tilde{\boldsymbol{u}} \right) \right] \, \mathrm{d}S \mathrm{d}t. \end{aligned} \tag{2.29}$$

where $\hat{\boldsymbol{n}}$ is the unit outward normal. For eq. 2.27 to hold true, the RHS of eq. 2.28 must be equal to zero. For the boundary conditions in eq. 2.12, eq. 2.29 becomes:

$$\begin{aligned} 0 = \int_\Omega \left[\tilde{\boldsymbol{u}} \cdot \tilde{\boldsymbol{u}}^\dagger \right]_0^\tau \, \mathrm{d}\Omega - \int_\Omega \tilde{\boldsymbol{u}}_0 \cdot \tilde{\boldsymbol{u}}^\dagger (t = 0) \, \mathrm{d}\Omega + \\ \int_0^\tau \oint_S \hat{\boldsymbol{n}} \cdot \left[\tilde{\boldsymbol{u}}^\dagger \tilde{p} + \nu \left(\nabla \tilde{\boldsymbol{u}} \right)^{\mathrm{T}} \cdot \tilde{\boldsymbol{u}}^\dagger \right] \, \mathrm{d}S \mathrm{d}t. \end{aligned} \tag{2.30}$$

Using the adjoint boundary conditions,

$$\tilde{\boldsymbol{u}}^\dagger (S, t) = 0, \tag{2.31}$$

eq. 2.30 becomes:

$$0 = \int_\Omega \left[\tilde{\boldsymbol{u}} \cdot \tilde{\boldsymbol{u}}^\dagger \right]_0^\tau \, \mathrm{d}\Omega. \tag{2.32}$$

Up until now, it has been assumed that $\boldsymbol{q}$ and $\boldsymbol{q}^\dagger$ are arbitrary. If we consider the case where $\boldsymbol{q}$ satisfies eq. 2.25 and $\boldsymbol{q}^\dagger$ satisfies

$$\mathcal{A}^\dagger \boldsymbol{q}^\dagger = 0, \tag{2.33}$$

then eq. 2.27 implies that under the inner product (eq. 2.22):

$$\Big(\tilde{\boldsymbol{u}}(\tau), \tilde{\boldsymbol{u}}^\dagger(\tau)\Big) - \Big(\tilde{\boldsymbol{u}}(0), \tilde{\boldsymbol{u}}^\dagger(0)\Big) = 0. \tag{2.34}$$

Therefore, eq. 2.27 is satisfied for the choices of $\mathcal{A}$ and $\mathcal{A}^\dagger$. The adjoint LNS equations may now be written out in full,

$$\begin{aligned} \frac{\partial \tilde{\boldsymbol{u}}_i^\dagger}{\partial t} + \frac{\partial}{\partial x_j}\tilde{\boldsymbol{u}}_i^\dagger \overline{\boldsymbol{u}}_j - \tilde{\boldsymbol{u}}_j^\dagger \frac{\partial}{\partial x_i}\overline{\boldsymbol{u}}_j &= -\frac{\partial \tilde{p}^\dagger}{\partial x_i} - \nu \frac{\partial^2 \tilde{\boldsymbol{u}}_i^\dagger}{\partial x_j \partial x_j}, \\ \frac{\partial \tilde{\boldsymbol{u}}_i^\dagger}{\partial x_i} &= 0, \end{aligned} \tag{2.35}$$

or using vector notation,

$$\begin{aligned} \frac{\partial \tilde{\boldsymbol{u}}^\dagger}{\partial t} + \left(\overline{\boldsymbol{u}} \cdot \nabla\right) \tilde{\boldsymbol{u}}^\dagger - \left(\nabla \overline{\boldsymbol{u}}\right)^{\mathrm{T}} \cdot \tilde{\boldsymbol{u}}^\dagger &= -\nabla \tilde{p}^\dagger - \nu \Delta \tilde{\boldsymbol{u}}^\dagger, \\ \nabla \cdot \tilde{\boldsymbol{u}}^\dagger &= 0. \end{aligned} \tag{2.36}$$

Note the opposite sign on the viscous term, which defines that the adjoint equations must be solved backwards in time. The adjoint equations can also be rewritten as a system of linear equations,

$$\frac{\partial \tilde{\boldsymbol{u}}_i^\dagger}{\partial t} = -\boldsymbol{A}^\dagger \tilde{\boldsymbol{u}}_i^\dagger, \tag{2.37}$$

where $\boldsymbol{A}^\dagger$ is the adjoint LNS operator and $\tilde{\boldsymbol{u}}_i^\dagger$ is the adjoint to the velocity perturbation field. Similar to the direct problem, we assume non-trivial solutions to eq. 2.35 of the

form:

$$\tilde{\boldsymbol{u}}_i^{\dagger}(x,y,z,t) = \sum_{\omega} \hat{\boldsymbol{u}}_i^{\dagger}(x,y,z)\, e^{-\omega t} + \text{c.c}, \tag{2.38}$$

which also can be simplified to an eigenvalue problem (similar to eq. 2.39),

$$-\boldsymbol{\Omega}\hat{\boldsymbol{U}}_i^{\dagger} = \boldsymbol{A}^{\dagger}\hat{\boldsymbol{U}}_i^{\dagger}, \tag{2.39}$$

where $\omega_j = \text{diag}\,(\boldsymbol{\Omega})_j$ is the j-th eigenvalue (coincident with the eigenvalue from linear stability analysis) and $\hat{\boldsymbol{u}}_i^{j,\dagger} = \boldsymbol{U}_i^{\dagger}[j,:]$ is the j-th adjoint eigenvector.

Hill (1995) explains how $\tilde{\boldsymbol{u}}_i^{\dagger}$, the adjoint velocity perturbation field, highlights points in the flow where a large response to unsteady point forcing will occur. In the present work, adjoint sensitivity stability analysis is used in conjunction with linear stability analysis to determine flow regions that are most sensitive to point momentum forcing.

2.3.1 Solutions of the linearized adjoint equations

The size of the eigenvalue problem associated with the global adjoint problem is computationally expensive to solve, just like in linear stability analysis. Therefore, the same method, the IRAM, from the P_ARPACK library, is implemented to efficiently compute the leading adjoint eigenvalues and their associated eigenvectors.

Similar to linear stability analysis, performing a temporal exponential transformation of the adjoint eigenvalue spectrum makes the most unstable eigenvalues the most dominant. Integrating backwards some finite time, τ, the adjoint problem (eq. 2.39) becomes:

$$\int_0^{-\tau} -\boldsymbol{\Omega}\hat{\boldsymbol{U}}_i^{\dagger}\,\mathrm{d}t = \int_0^{-\tau} \boldsymbol{A}^{\dagger}\hat{\boldsymbol{U}}_i^{\dagger}\,\mathrm{d}t. \tag{2.40}$$

This yields the exponential transformation of the original eigenvalue problem (eq. 2.39):

$$\mathrm{e}^{\boldsymbol{\Omega}\tau}\hat{\boldsymbol{U}}_i^{\dagger} = \mathrm{e}^{-\boldsymbol{A}^{\dagger}\tau}\hat{\boldsymbol{U}}_i^{\dagger}, \tag{2.41}$$

which can be rewritten as:

$$\boldsymbol{\Sigma}\hat{\boldsymbol{U}}_i^{\dagger} = \boldsymbol{B}^{\dagger}\hat{\boldsymbol{U}}_i^{\dagger}, \tag{2.42}$$

where $\sigma_j = \mathrm{diag}\,(\boldsymbol{\Sigma})_j$. The matrix exponential $\boldsymbol{B}^{\dagger} = \mathrm{e}^{-\boldsymbol{A}^{\dagger}\tau}$ is a time integration operator, which is the same as integrating the adjoint LNS equations (eq. 2.35) backwards some finite time, τ. Note that between the two eigenvalue problems (eq. 2.39, 2.42), the adjoint eigenvectors, $\hat{\boldsymbol{U}}_i^{\dagger}$, are still the same. However, the adjoint eigenvalues of the original adjoint problem (eq. 2.39) are recovered using the same relationship from linear stability analysis (eq. 2.20).

2.3.2 Wavemaker

This dissertation also discusses the receptivity of the JICF to spatially localized feedback. Due to the non-normality of the eigenvalue problem associated with the JICF, adjoint solutions alone cannot describe the whole picture. Therefore, the product for each j-th pair of direct and adjoint global modes is computed as

$$W_j\,(x,y,z) = \frac{\left\|\hat{\boldsymbol{u}}_i^{j}\right\|\left\|\hat{\boldsymbol{u}}_i^{j,\dagger}\right\|}{\max\left(\left\|\hat{\boldsymbol{u}}_i^{j}\right\|\left\|\hat{\boldsymbol{u}}_i^{j,\dagger}\right\|\right)}, \tag{2.43}$$

which determines the locations that are most sensitive to localized feedback (Giannetti & Luchini, 2007) - also called 'wavemaker' regions. Locations where $W \approx 1$ are most sensitive to localized feedback, whereas areas with $W << 1$ are generally not important to the stability of the baseflow.

Additionally, Giannetti & Luchini (2007) have shown that the eigenvalues from linear stability analysis and adjoint sensitivity analysis are sensitive to domain size changes when values of the wavemaker, W_j, are substantially different from zero at locations close to the domain boundaries. In wavemaker results that follow in chapter 5, all of the isocontours are displayed with a value of 0.01, and are spatially located far from the edges of the domain.

2.4 Optimal perturbation analysis

The study of hydrodynamic stability has long been dominated by modal analysis, which is based on an exponential time dependence and thus only concerned with the asymptotic fate of flow perturbations. However, modal stability analysis fails to predict (Reddy & Henningson, 1993) problems such as the transition-to-turbulence of laminar channel flow observed in experiments. This failure to capture sub-critical transition, where all the eigenvalues from the modal analysis have negative growth rates, is shown to be a result of a non-normality of the associated governing linear operator. There is strong interest in studying the stability of baseflows over different finite time horizons. This approach is termed non-modal stability analysis, or optimal perturbation analysis, and was pioneered by Boberg & Brosa (1988), Gustavsson (1991), Reddy *et al.* (1993), Reddy & Henningson (1993), Trefethen *et al.* (1993), Butler & Farrell (1994), and Schmid & Henningson (2001). Schmid (2007) provides a comprehensive review. The traditional concept of Lyapunov stability does not coincide with non-modal stability analysis. Furthermore, the shape of the eigenmodes from optimal perturbation analysis and traditional asymptotic-time stability analysis can vary significantly, as they describe stability from different perspectives.

Optimal perturbation analysis begins with the decision of how best to quantitatively measure the perturbation energy. In this dissertation, the energy norm is again used as in §2.3 (eq. 2.22). Recall from §2.2 and §2.3, the time integration operators for the direct and adjoint equations $\boldsymbol{B}$ and $\boldsymbol{B}^\dagger$, respectively. Due to the linearity of the perturbations, it makes sense to normalize the energy with the initial energy when describing the transient growth.

$$\frac{E(\tau)}{E_0} = \frac{(\tilde{\boldsymbol{u}}(\tau), \tilde{\boldsymbol{u}}(\tau))}{(\tilde{\boldsymbol{u}}_0, \tilde{\boldsymbol{u}}_0)}, \tag{2.44}$$

where τ is the time scale that the transient growth is optimized over. This value τ is often smaller than the τ used in linear stability analysis and adjoint sensitivity stability analysis in the previous sections. The perturbation energy may also be expressed in

terms of the evolution operators:

$$\frac{E(\tau)}{E_0} = \frac{(\boldsymbol{B}\tilde{\boldsymbol{u}}_0, \boldsymbol{B}\tilde{\boldsymbol{u}}_0)}{(\tilde{\boldsymbol{u}}_0, \tilde{\boldsymbol{u}}_0)} = \frac{\left(\tilde{\boldsymbol{u}}_0, \boldsymbol{B}^\dagger \boldsymbol{B}\tilde{\boldsymbol{u}}_0\right)}{(\tilde{\boldsymbol{u}}_0, \tilde{\boldsymbol{u}}_0)}, \tag{2.45}$$

For optimal perturbation analysis, we are interested in the initial perturbations, $\tilde{\boldsymbol{u}}_0$, that result in the largest transient growth. Examination of eq. 2.45, reveals that $\tilde{\boldsymbol{u}}_0$ is determined by the eigenvalues and eigenmodes of the operator $\boldsymbol{B}^\dagger \boldsymbol{B}$. The eigenvalue problem may be expressed as:

$$\boldsymbol{\Lambda}\hat{\boldsymbol{U}}_i^* = \boldsymbol{B}^\dagger \boldsymbol{B}\hat{\boldsymbol{U}}_i^*, \tag{2.46}$$

where $\lambda_j = \text{diag}\,(\boldsymbol{\Lambda})_j$ is the j-th eigenvalue (i.e. growth factor) and $\hat{\boldsymbol{u}}_i^{j,*} = \boldsymbol{U}_i^*[j,:]$ is the j-th optimal perturbation eigenmode. The leading eigenmode offers the largest transient growth for the specified value of τ, but sub-optimal eigenmodes often provide valuable insight towards other flow mechanisms that generate energy growth.

The size of the eigenvalue problem associated with optimal perturbation analysis is also computationally expensive to solve. The same method, the IRAM, is used to solve for the leading growth factors and the associated optimal perturbations. However, for optimal perturbation analysis, the eigenvalue problem is already formulated as a time-stepper method. The RHS of eq. 2.46 is analogous to integrating a velocity perturbation forward some time τ through the LNS equations, then backwards for time τ through the adjoint equations. Therefore, the IRAM solves for the leading eigenvalues and eigenmodes without any further manipulation.

2.5 Baseflow generation

For increasingly complex and globally unstable flows, a steady-state solution may be difficult and computationally expensive to obtain. As linear stability, adjoint sensitivity, and optimal perturbation analyses look to study more interesting and complex problems, other approaches are being followed to solve for base states. Selective frequency damping (SFD) (Akervik *et al.*, 2006) may be used to obtain a steady-state solution. Here a

forcing term, which acts as temporal low-pass filter, is added to the right-hand side. Some knowledge of the lowest unstable frequency is required when choosing the filter width. In order to converge to a steady solution, the filter cut-off frequency must be lower than that of all of the flow instabilities. Although this method lends itself to easy implementation, the computational cost is governed by the range of time-scales. Additionally, SFD fails to dampen instabilities that are non-oscillatory, as shown by Vyazmina (2010).

Another option is to use a turbulent mean flow as a base state. Perhaps the best known example where linear stability analysis about the turbulent mean flow succeeds over the steady-state solution is the oscillating wake of a circular cylinder (Barkley, 2006). The solutions about both base states agree at the onset of instability, but the steady-state base flow fails to capture the observed vortex shedding frequency far away from the bifurcation point. Recent studies by Turton *et al.* (2015) and Tammisola & Juniper (2016) examine linear stability around a turbulent mean flow. Barkley (2006) and Turton *et al.* (2015) show that performing linear stability analysis around a turbulent mean flow results in eigenvalues which have small real parts and non-zero imaginary frequencies.

Since a turbulent mean flow is a solution to the Reynolds-averaged N-S equations, a non-linear Reynolds stress term is effectively added to the LNS equations when the baseflow equations are removed (eq. 2.1-2.11). This translates into a mode-dependent Reynolds stress being present in the eigenvalue problem (eq. 2.16). A scale-separation argument, first introduced by Crighton & Gaster (1976), and more recently discussed in the review by Jordan & Colonius (2013), can be used to justify when the mode-dependent Reynolds stress term is negligible. Only for the modes of interest (typically low frequency and large-scale) must the Reynolds stress term be shown to be unimportant. For turbulent problems, multiple orders of magnitude can separate the time and length scales of turbulent motions (t_η and η, respectively) with the motions of interest (L and t_L, respectively). Relationships between turbulent and large scale motions of

interest can be determined from the Kolmogorov scales (Pope, 2000, pp. 186):

$$\begin{aligned} L/\eta &= Re^{3/4}, \\ t_L/t_\eta &= Re^{1/2} \end{aligned} \tag{2.47}$$

Therefore, if the scale-separation argument is to hold, there must be a significant gap between scales of interest for linear stability analysis and the turbulent motions themselves. It can be shown by using the above relationships that using a turbulent mean flow as a base state for linear stability analysis can provide meaningful physical insight into flow dynamics.

Chapter 3

Validation

This chapter includes several validation cases for the analyses that are performed in chapters 4-6. §3.1 shows validation for global linear stability analysis, and also includes some insights into selecting the IRAM parameters. Adjoint analysis is validated for two problems in §3.2. Finally, optimal perturbation analysis is validated for the 3D lid-driven cavity in §3.3.

3.1 Linear stability

Table 3.1 outlines the validation cases considered. First, parallel flow linear stability analysis of a Blasius boundary layer subject to a streamwise Tollmien-Schlichting (T-S) wave is compared to the results of Criminale *et al.* (2003). Next, Bi-Global linear stability analysis of a 2D lid-driven cavity with a spanwise wave disturbance is compared to the work of Ding & Kawahara (1998). Linear stability analysis of a 3D lid-driven cavity is then validated against Gómez *et al.* (2014). Finally, linear stability analysis of laminar channel flow is compared to the classic parallel flow linear stability results for Poiseuille flow.

Type	Flow	Re	Reference(s)
Parallel Flow	Blasius boundary layer	580	Criminale *et al.* (2003)
Bi-Global	2D lid-driven cavity	200	Ding & Kawahara (1998)
Global	3D lid-driven cavity	1000	Gómez *et al.* (2014) Giannetti *et al.* (2009)
Global	laminar channel flow	1000	Juniper *et al.* (2014)

Table 3.1: Descriptions of the cases used for validation of linear stability analysis.

3.1.1 Parallel flow linear stability

Parallel flow linear stability assumes wave-like homogeneity in time and two spatial directions. This allows for the governing equations to be simplified to an ODE, which reduces the computational cost of solving the associated linear stability eigenvalue problem. Here the stability of a Blasius boundary layer is chosen as a validation case due to its simplicity and the extensive analysis in the literature. For this problem the spanwise and streamwise directions are assumed to be homogeneous.

Criminale *et al.* (2003) provide temporal linear stability results for a Blasius boundary layer subject to a streamwise T-S disturbance. The applied T-S disturbance has a wavenumber $\alpha = 0.179$ and the $Re = 580$, based on the boundary layer thickness. The eigenvalue problem corresponding to the Orr-Sommerfield equations is solved directly by Criminale *et al.* (2003). In the present work, the eigenvalue problem associated with the 2D LNS (eq. 2.11) is instead solved, using the approach outlined in §2.2. The seven leading eigenvalues show good agreement with Criminale *et al.* (2003) as shown in table 3.2.

3.1.2 Bi-Global linear stability

The flow in a 2D lid-driven cavity is studied using Bi-Global linear stability. Here, time and the spanwise direction are assumed to be homogeneous. The base state is the 2D steady-state solution for the square lid-driven cavity at $Re = 200$, based on the cavity height and lid velocity. Two purely real (i.e. oscillatory) spanwise wavenumbers

Re	α	Criminale *et al.* (2003)	Present
580	0.179	0.007970 + i0.3641	0.007835 + i0.3657
		−0.2787 + i0.2897	−0.2765 + i0.2922
		−0.1921 + i0.4839	−0.1925 + i0.4862
		−0.3653 + i0.5572	−0.3648 + i0.5597
		−0.3308 + i0.6863	−0.3307 + i0.6885
		−0.4341 + i0.7937	−0.4334 + i0.7959
		−0.4147 + i0.8874	−0.4131 + i0.8879

Table 3.2: The leading eigenvalues ($c_j = \omega_j/\alpha$) from parallel flow linear stability results for a Blasius boundary layer at $Re = 580$, subject to a streamwise T-S wave, ($\alpha = 0.179$), compared to Criminale *et al.* (2003).

Re	β	Ding & Kawahara (1998)	Present
200	6	$-0.38 + i0.57$	$-0.38 + i0.56$
	9	$-0.54 + i0.75$	$-0.54 + i0.72$

Table 3.3: The leading eigenvalues (ω_j) from Bi-Global linear stability of a 2D lid-driven cavity subject to different spanwise wavenumbers (β) compared to Ding & Kawahara (1998).

($\beta = 6, 9$) are individually applied as perturbations to the base state. The 2D LNS (eq. 2.11) are solved in conjunction with the time-stepper method and the IRAM outlined in §2.2. Results from Bi-Global linear stability are compared to Ding & Kawahara (1998) in table 3.3, and good agreement is observed.

3.1.3 Global linear stability

When performing global linear stability analysis, no directions are assumed to be homogeneous. Only recently have computational resources made it practical to study the stability of complex 3D problems. The stability of a 3D lid-driven cavity has been studied by multiple authors using different numerical techniques.

The stability of a steady cubic 3D lid-driven cavity is studied at a Reynolds number of

Re	Giannetti *et al.* (2009)	Gómez *et al.* (2014)	Present
1000	$-0.1276 \pm i0.285$	$-0.1292 \pm i0.329$	$-0.1352 \pm i0.299$
	$-0.1301 \pm i0.457$	$-0.1348 \pm i0.485$	$-0.1304 \pm i0.487$
	-0.1457	-0.1382	-0.1375

Table 3.4: The leading eigenvalues (ω_j) from linear stability analysis for a stable 3D lid-driven cavity (288^3 elements) at $Re = 1000$ compared to Gómez *et al.* (2014) (64^3 elements) and Giannetti *et al.* (2009) (114^3 elements) for validation.

1000, based on the cavity height and lid velocity. Giannetti *et al.* (2009) and Gómez *et al.* (2014) have both performed linear stability analysis of a cubic 3D lid-driven cavity. All three results were obtained using some form of the Arnoldi iteration method. Giannetti *et al.* (2009) solve the LNS (eq. 2.11) and utilize the IRAM within the ARPACK library. Gómez *et al.* (2014) directly apply the output from a N-S (eq. 2.1) solver to generate approximate results for linear stability analysis using the classic Arnoldi algorithm. The present work solves the LNS, but utilizes the IRAM implemented in the P_ARPACK library. Results show good agreement across the different numerical methods as shown in table 3.4.

Furthermore, the real part of the leading eigenmodes from the present work are shown in figure 3.1 and highlight positive and negative isocontours of the perturbation velocity fields. Eigenmode results shown in Gómez *et al.* (2014) show good qualitative agreement with the present work. The complexity as well as the symmetry of the 3D cavity can be seen in the eigenmode results. The third eigenmode is a stable stationary mode (i.e. non-oscillatory), and has been described by Gómez *et al.* (2014) as resembling different families of linear modes with Taylor-Görtler-like structures.

3.1.4 Global linear stability and parallel flow linear stability

As a final point of validation, results from linear stability analysis are compared to classic parallel flow linear stability. The stability of a laminar channel is chosen because the assumption that the streamwise and spanwise directions are homogeneous holds true, making the parallel flow assumption valid.

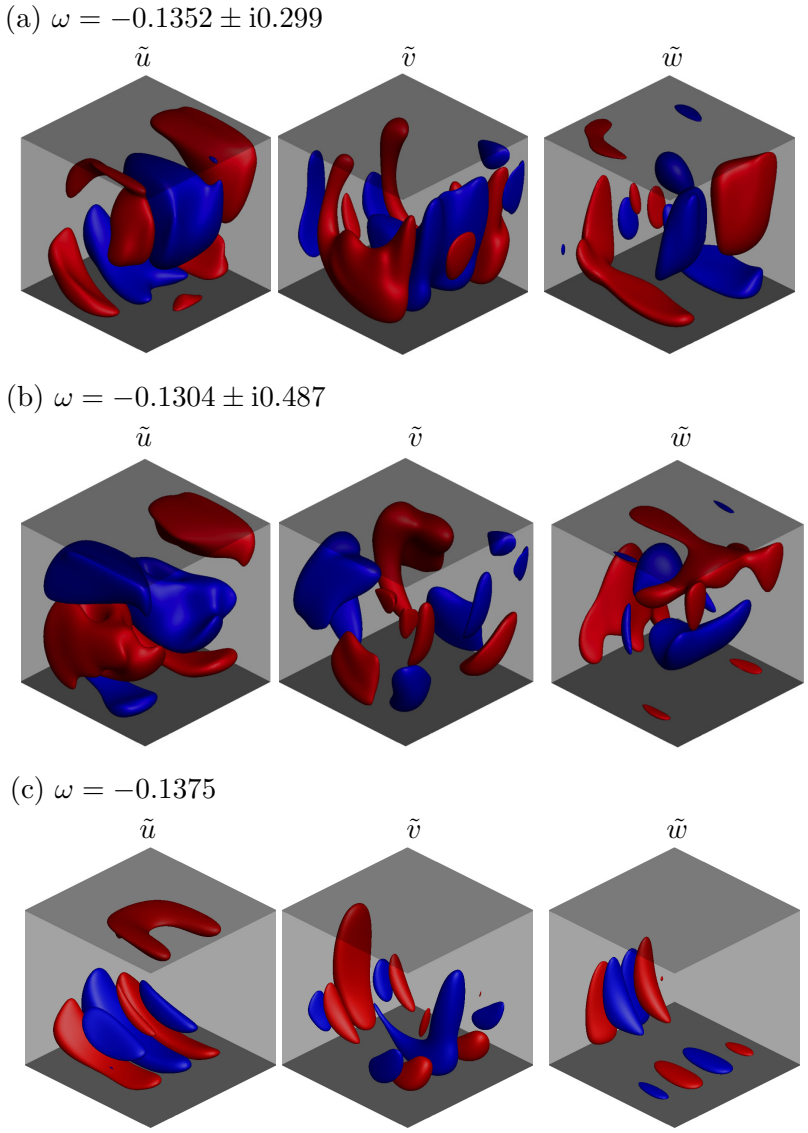

Figure 3.1: Real part of the eigenmodes from linear stability analysis for a 3D lid-driven cavity at $Re = 1000$. The results are shown with positive and negative isocontours of $\tilde{u}, \tilde{v}, \tilde{w} = \pm 0.15$. The associated eigenvalues are shown, with the real part being the growth rate, and the imaginary part being the frequency. Modes (a-c) show good qualitative agreement with Gómez *et al.* (2014). A comparison to the eigenvalues results of Giannetti *et al.* (2009) and Gómez *et al.* (2014) may be found in table 3.4.

The stability of a laminar channel at a $Re = 5780$, based on the centerline velocity and channel half height h, is first computed using linear stability analysis. The channel half height h is 1, while the streamwise length is 4π and the spanwise width is $4\pi/3$. Periodic boundary conditions are applied in the streamwise and spanwise directions, whereas a no-slip condition is applied at the top and bottom of the channel. Since the streamwise and spanwise wavenumbers (α and β, respectively) are not specified in linear stability analysis, any combination of wavenumbers may be present in the global linear stability results. Therefore, the j-th pair of ω_j and $\hat{\boldsymbol{u}}_i^j$ may have a non-zero α_j and/or β_j that can then be extracted using streamwise and spanwise Fast Fourier transforms (FFT). The α_j and β_j can then be used as input to parallel flow linear stability.

The non-zero components of two leading eigenmodes from linear stability analysis are shown in figures 3.2a-b and 3.3a. A quantitative comparison between the global linear stability results and the results from parallel flow linear stability are shown in figures 3.2c and 3.3b. The complex Fourier coefficients, $\hat{\boldsymbol{u}}_i^j$, as well as their magnitudes, are plotted against the results from parallel flow linear stability. The comparison shows good agreement for both eigenmodes in all three velocity components.

The same two leading eigenvalues from global linear stability and parallel flow linear stability are shown in table 3.5. The eigenvalues are non-dimensionalised by the centerline velocity and the channel half height h. The agreement between the two different numerical methods, utilizing drastically different numerical techniques and different assumptions, is very good. Good agreements for growth rates and frequencies are obtained. Thus, the present unstructured grid linear stability solver can be considered validated. The stability solver will now be used to study the global linear stability of the JICF.

3.1.5 Rotational reference frame

Several fluid flows involve the rotation of axisymmetric bodies, which may be described by solving the fluid equations in a rotating reference frame. For example Kumar & Mahesh (2017) studied propeller wake instabilities using LES and such co-ordinate transformation. A simple extension to the global linear stability analysis formulation described

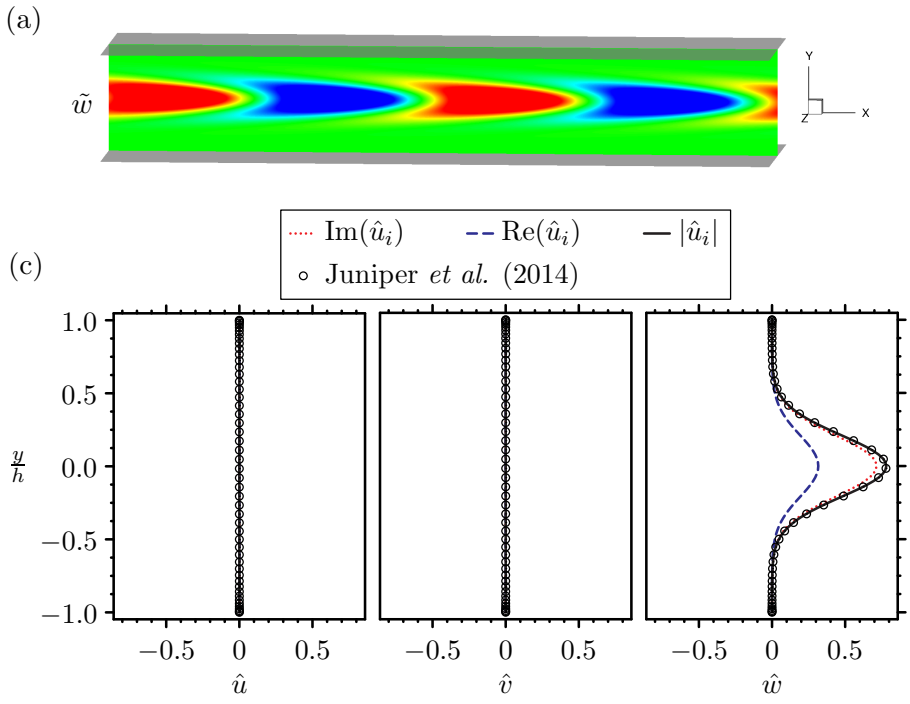

Figure 3.2: Real parts of the first eigenmode corresponding to the eigenvalues in table 3.5 from global linear stability for laminar channel flow at $Re = 1000$. Here, there is no variation in the z-direction, making a single slice sufficient to display all relevant data. The results are shown as an x-y slice ($z = 0$) with contours of $\tilde{w}$ (note: $\tilde{u} = \tilde{v} = 0$). The streamwise and spanwise wavenumbers ($\alpha = \mathrm{i}1$, $\beta = \mathrm{i}0$) are extracted and used as input to classic parallel flow stability analysis of Poiseuille flow. Additionally, the Tri-Global eigenmode Fourier coefficients ($\hat{\boldsymbol{u}}_i$) are compared to the results from parallel stability of Juniper *et al.* (2014) for $|\hat{u}|$, $|\hat{v}|$ and $|\hat{w}|$. Note that every fourth point from Juniper *et al.* (2014) is plotted in an effort to not obscure other data.

Re	α	β	Juniper *et al.* (2014) [Parallel linear stability]	Present [Global linear stability]
1000	1	0	$-2.33610 \times 10^{-2} + \mathrm{i}0.977640$	$-2.33374 \times 10^{-2} \pm \mathrm{i}0.977638$
	1	1.5	$-2.56110 \times 10^{-2} + \mathrm{i}0.977640$	$-2.55906 \times 10^{-2} \pm \mathrm{i}0.977638$

Table 3.5: Two leading eigenvalues (ω_j) from global linear stability for laminar channel flow at $Re = 1000$. Streamwise wavenumbers, α, and spanwise wavenumbers, β, are observed in the global eigenmodes (see figures 3.2 and 3.3) and are used as input to parallel flow stability analysis of Poiseuille flow. The parallel flow stability results are produced by a code available in the supplementary material from Juniper *et al.* (2014).

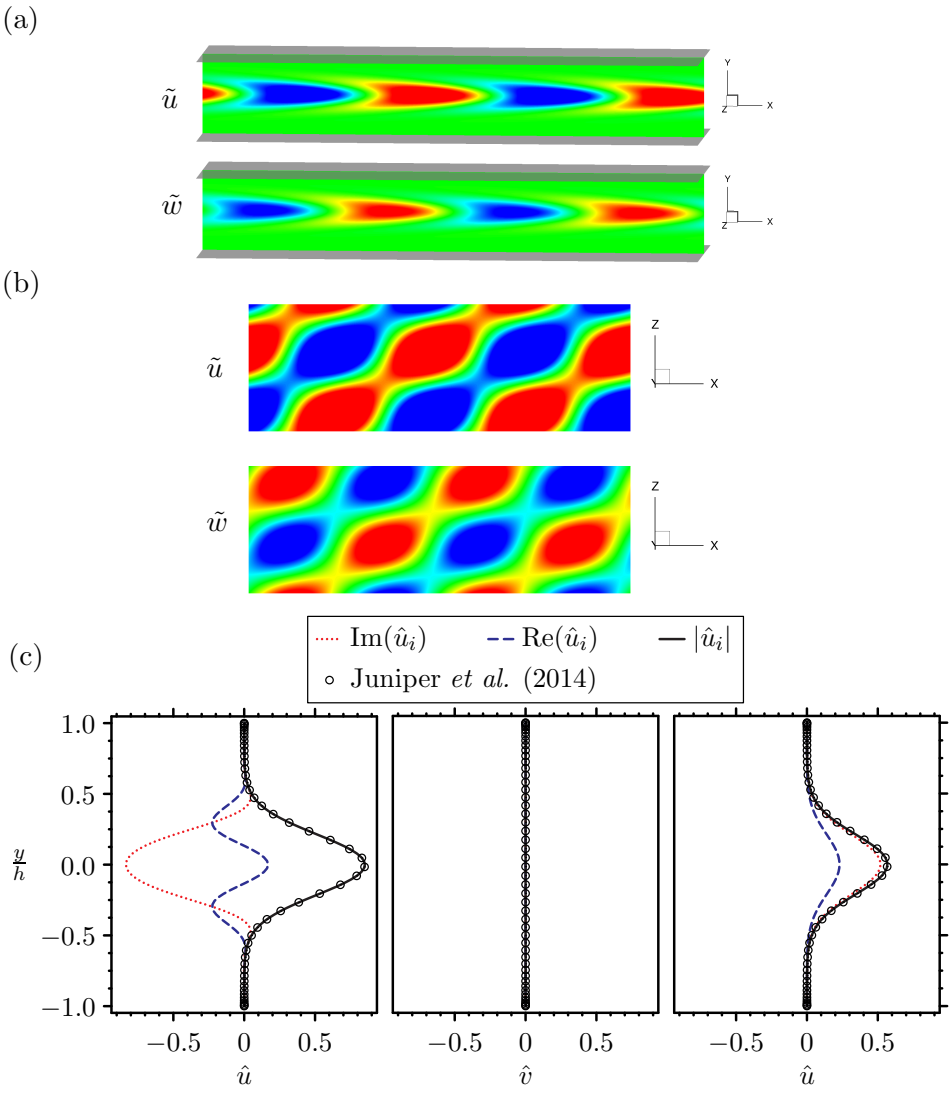

Figure 3.3: The real part of the second eigenmode corresponding to the eigenvalues in table 3.5 from global linear stability for laminar channel flow at $Re = 1000$. The results are shown as x-y ($z = 0$) and $z-x$ ($y = 0$) slices with contours of $\tilde{u}$ and $\tilde{w}$ (note: $\tilde{v} = 0$). The streamwise and spanwise wavenumbers ($\alpha = \mathrm{i}1$ and $\beta = \mathrm{i}1.5$) may be extracted and used as input to a classic parallel flow stability analysis of Poiseuille flow. Tri-Global eigenmode Fourier coefficients ($\hat{\boldsymbol{u}}_i$) are compared to the results from parallel stability of Juniper *et al.* (2014) for $|\hat{u}|$, $|\hat{v}|$ and $|\hat{w}|$. Note that every fourth point from Juniper *et al.* (2014) is plotted in an effort to not obscure other data.

Re	Inertial Frame	Rotating Frame
88.1	$-0.6865 \times 10^{-1} + \mathrm{i}0$	$-0.6878 \times 10^{-1} + \mathrm{i}0$

Table 3.6: The leading linear stability eigenvalues from Taylor-Couette flow solved in inertial and rotational frames of reference.

in the previous sections allows for the analysis to be performed in a rotating reference frame.

Validation for a rotating reference frame is performed using Taylor-Couette flow where two infinitely long concentric cylinders rotate with respect to one another. Here, $Re = \Omega r_1 D/\nu = 88.1$, where the inner radius $r_1 = 1$, the outer radius $r_2 = 2$, $D = r_2 - r_1$, and Ω is the angular speed of the inner cylinder. This problem is chosen because it can easily be solved in both inertial and rotating reference frames.

Table 3.6 shows a comparison of the leading linear stability analysis eigenvalues between inertial and rotating frames of reference. Very good agreement is observed between the two separate analyses. Figure 3.4a shows the steady baseflow using contours of the θ-direction velocity $\overline{u}_\theta$ ($\overline{u}_r = 0$), which has no variation in the z-direction. Figures 3.4b and 3.4c show the leading eigenmodes for the inertial and rotating reference frame analyses, respectively. There is good agreement between the two leading eigenmodes. Both show two counter-rotating cells, highlighted by iso-contours of Q-criterion of the perturbation velocities colored by $\tilde{u}_\theta$. The Q-criterion (Hunt *et al.*, 1988) highlights vortex cores by representing regions where pressure is a local minimum. Q is defined as:

$$Q = \frac{\partial u_i}{\partial x_j}\frac{\partial u_j}{\partial x_i}. \tag{3.1}$$

The vortical cells are stacked on top of each other and extend periodically in both z directions. Perturbation streamlines show how the perturbations rotate around the vortical cells.

Interestingly, the convergence behavior between the two analyses are different. Figure 3.5 shows the Ritz residual for the leading eigenvalue for each Arnoldi iteration

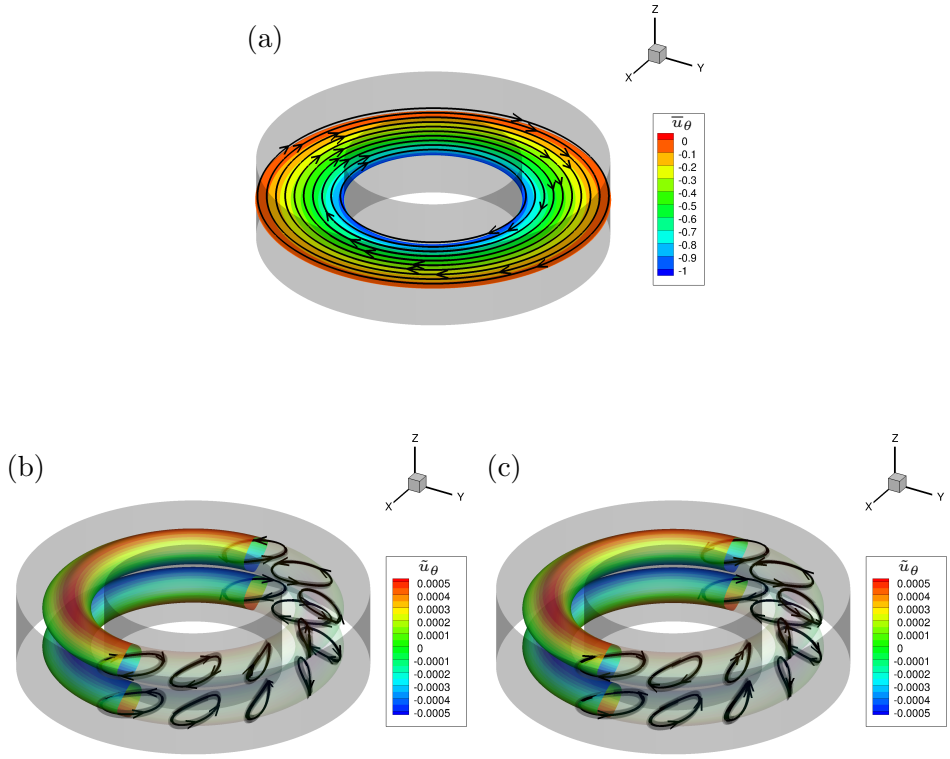

Figure 3.4: Linear stability results for Taylor-Couette flow are compared. The baseflow is shown in (a). The leading eigenmode when solved in the inertial frame is shown in (b), and (c) shows the solution obtained using a rotating reference frame. Isocontours of Q-criterion colored by $\tilde{u}_\theta$ along with perturbation streamlines are used to show the eigenmodes.

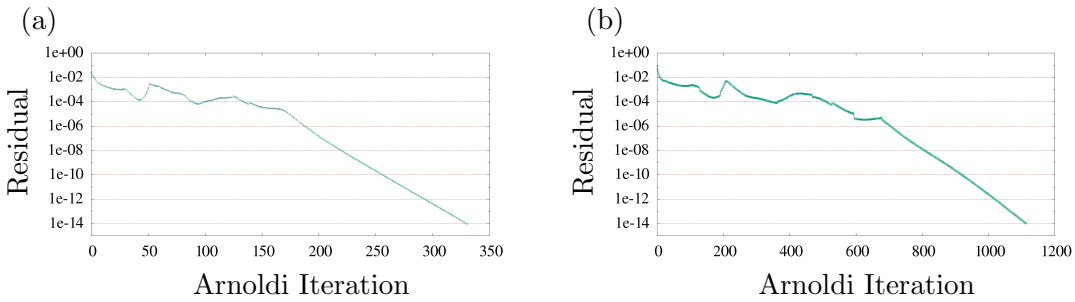

Figure 3.5: Residual behavior when performing linear stability of Taylor-Couette flow in the inertial (a) and rotating frames (b).

in the IRAM. The convergence behavior is similar for both analyses, but the rotating frame takes significantly more Arnoldi iterations compared to the inertial frame.

3.1.6 IRAM parameters

Choosing the correct parameters can significantly affect the results from the IRAM. Since the goal of using the IRAM is to efficiently solve for the leading eigenvalues of a given operator, the first task is to determine the number of leading eigenvalues (and associated eigenvectors) that are of interest. The number of eigenvalues nev to be solved is typically $nev \approx 20$ for a problem with an arbitrary three-dimensional baseflow (i.e. a global problem). The minimum number of Arnoldi vectors m that must be computed for each Arnoldi iteration is defined as $m \geq 2 \times nev + 1$ for the IRAM.

For linear stability and adjoint sensitivity analyses, the IRAM must solve for the eigenvalues σ_j (eq. 2.20) with the largest magnitude; which are equivalent to the eigenvalues ω_j with the largest real part (i.e. growth rate). However, when performing optimal perturbation analysis, the eigenvalue problem that the IRAM solves does not require a recovery equation (e.g. eq. 2.20); therefore, the IRAM is set to solve for the eigenvalues with the largest real part.

The next most important parameter is to determine what integration time τ is appropriate to capture the eigenvalues of interest. Typically, the eigenvalues of interest are those with the largest magnitude (or largest real part for optimal perturbation analysis). The IRAM is an implicitly restarted rendition of the classic Arnoldi iteration

method. The Arnoldi iteration method belongs to a class of algorithms in linear algebra that use Krylov subspaces to efficiently solve for the first few results of a large eigenvalue problem using a small number of iterations. Specifically, the Arnoldi iteration method is very good at solving eigenvalue problems with large matrices that are sparse. To do this, the IRAM interprets how the matrix maps different vectors to solve the leading eigenvalues of the matrix itself. That being said, since the IRAM only interprets the mapping over some finite time τ, anything that happens at a smaller time scale than τ is aliased to a larger time scale. Therefore, τ must be chosen so that the sampling rate, or Nyquist frequency ω_{ny}, is higher than the highest frequencies of interest ω_{high}. As a rule of thumb, $\tau \leq \pi/\omega_{\text{ny}} = \pi/(2f_{\text{high}})$ to ensure that at least 2 points may be used to capture the highest frequencies of interest.

However, if τ is too small, the temporal separation between the different Arnoldi vectors can become too small, which will slow or prevent convergence of the IRAM. Therefore, an appropriate value of τ most be chosen for each problem to ensure convergence to the correct solution without excess computational expense. Generally, τ should be chosen so that the set of Arnoldi vectors for each Arnoldi iteration spans the largest time scales ($1/f_{\text{low}}$) of the flow (i.e. $m\tau \approx 1/f_{\text{low}}$).

Figure 3.6 shows three leading eigenvalues for the 3D lid-driven cavity, and how they can be aliased to lower frequencies if poor choices of τ are chosen for the time-stepper method. Horizontal dashed lines mark the growth rate for each of the three eigenvalues. Different-sized circles are used to denote eigenvalues for different τ. Notice that 'eig1', the highest frequency eigenvalue, gets aliased to a lower frequency first for $\tau \geq 10$. Next, the lower frequency 'eig2'is aliased for $\tau \geq 30$. The third eigenvalue, 'eig3'has no frequency component and is therefore unaffected by the choice of τ.

3.2 Adjoint Sensitivity

Adjoint sensitivity is validated for a Blasius boundary layer and laminar channel flow in this section.

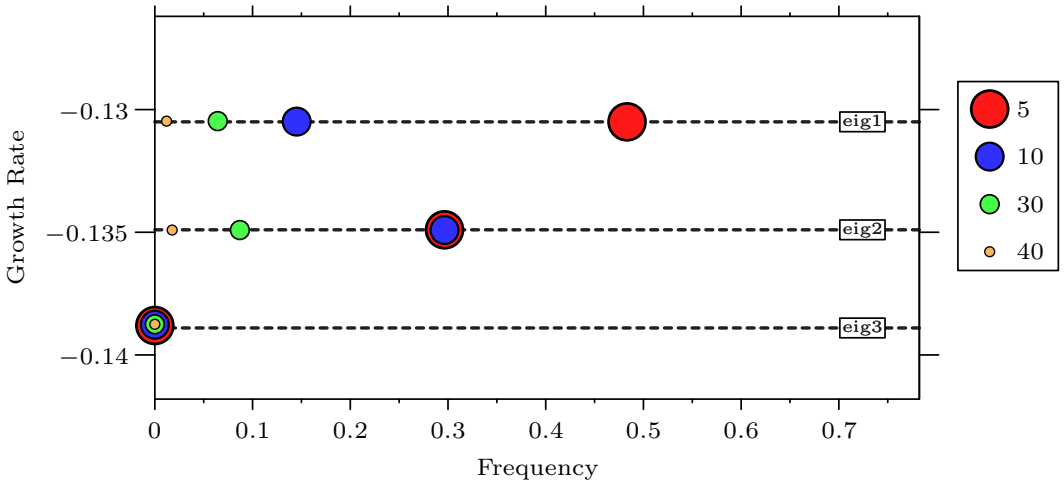

Figure 3.6: Choosing a τ that is too large will alias eigenvalues to lower frequencies. The three leading eigenvalues are examined for the 3D lid-driven cavity at $Re = 1000$. Four different values of τ are used, and the effect of aliasing on the frequencies is clear for higher values of τ. Note that the stationary eigenvalue is unaffected.

3.2.1 Blasius boundary layer

Hill (1995) studied the stability and sensitivity of the Blasius boundary layer. The parallel flow assumption is valid here, which allows us to assume streamwise homogeneity in the form of the wavenumber α (no spanwise component). To be consistent with the study by Hill (1995), the following ansatz is defined for this validation case:

$$\tilde{\boldsymbol{u}}_i^\dagger(x,y,t) = \sum_{\alpha,\omega} \hat{\boldsymbol{u}}_i^\dagger(y)\, e^{\mathrm{i}(\alpha x - \omega t)} + \text{c.c.} \tag{3.2}$$

The base state is the Blasius boundary layer solution. Distances are non-dimensionalized by $\delta = \sqrt{\nu L/U_\infty}$, where L is the dimensional distance from the leading edge of the plate. The distance from the wall where $u = 0.99U_\infty$ is $\delta_{99} = 4.93\delta \approx 5\frac{y}{\delta}$.

The Blasius boundary layer is studied at $Re = U_\infty\delta/\nu = 1274$, and is subjected to a streamwise T-S wave with $f = \omega/Re = 20 \times 10^{-6}$. Here, a real ω is prescribed, and α is the complex eigenvalue, which makes this a spatial sensitivity problem. The leading adjoint eigenvalue calculated by Hill (1995) is $\alpha = 0.0895 - \mathrm{i}0.00377$, compared

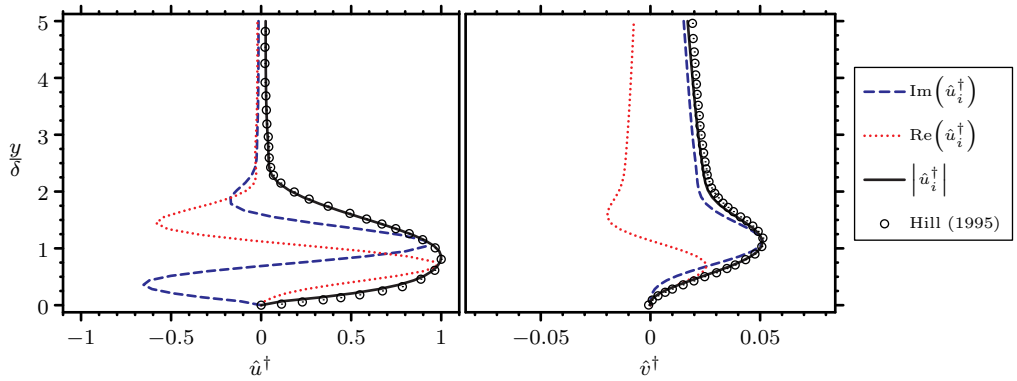

Figure 3.7: Spatial adjoint sensitivity of a Blasius boundary is used as a validation case. Hill (1995) performed parallel flow adjoint sensitivity analysis at $Re = U_\infty \delta/\nu = 1274$ subject to a T-S wave with $f = \omega/Re = 20 \times 10^{-6}$. Hill (1995) recovered the leading adjoint eigenvalue $\alpha = 0.0895 - \mathrm{i}0.00377$ compared to $\alpha = 0.0894 - \mathrm{i}0.00381$ from the present work. The associated eigenmodes are displayed above and show good agreement when comparing the magnitudes. The grid used by Hill (1995) has 84 elements in the y-direction, compared to the 80 points used in the present work. Note that $\delta_{99} = 4.93\delta \approx 5\frac{y}{\delta}$.

to $\alpha = 0.0894 - \mathrm{i}0.00381$ from the present work. The associated adjoint eigenmodes are shown in figure 3.7 (normalized by $\max(|\hat{u}_i|)$), which highlight the good agreement between the magnitudes from both calculations.

Recall that $\hat{u}^\dagger$ corresponds to the sensitivity of the direct eigenmode (in this case a T-S wave with $f = 20 \times 10^{-6}$) to streamwise momentum point forcing. Similarly, $\hat{v}^\dagger$ describes the sensitivity to wall-normal momentum point forcing. From the adjoint analysis, it is clear that applying streamwise momentum point forcing at a distance $y/\delta \approx 1$ is the most effective way to excite the associated T-S direct eigenmode. Additionally, wall-normal momentum forcing is approximately 5.5% as effective at generating a response from the T-S direct eigenmode.

3.2.2 Laminar channel flow

The final validation problem compares two leading eigenvalues from direct parallel linear stability (Juniper *et al.*, 2014), global linear stability (§3.1.4), and the global adjoint

sensitivity of laminar channel flow. The parallel flow assumption holds true, and therefore the streamwise and spanwise directions can be assumed to be homogeneous. In other words, for the parallel flow analysis the following ansatz will be used:

$$\tilde{\boldsymbol{u}}_i^\dagger(x,y,z,t) = \sum_{\alpha,\beta,\omega} \hat{\boldsymbol{u}}_i^\dagger(y)\, e^{\mathrm{i}(\alpha x+\beta z)+\omega t} + \text{c.c.} \tag{3.3}$$

However, in global linear stability and global adjoint sensitivity analyses, all spatial directions are considered inhomogeneous. Results from the global linear stability and global adjoint sensitivity use the ansatzes defined in §2 (eq. 2.15 and eq. 2.38, respectively).

A steady baseflow is used in the stability and sensitivity analyses corresponding to the laminar channel flow at $Re = 1000$, based on the centerline velocity and the channel half-height h. The length in the streamwise direction is 4π and the length in the spanwise direction is $4\pi/3$. In the streamwise and spanwise directions we apply periodic boundary conditions, and a no-slip condition is applied at the top and bottom of the channel.

Any combination of streamwise and spanwise wavenumbers may be present in the global linear stability and adjoint sensitivity results because those directions are assumed to be inhomogeneous. However, the eigenmodes from global linear stability (figures 3.2a and 3.3a-b) and global adjoint sensitivity (figures 3.8a and 3.9a-b) are specifically chosen because they show clear streamwise (α) and spanwise (β) wavenumbers. These wavenumbers are recovered by performing a two-dimensional Fast Fourier Transform (FFT) in the x and z directions. Next, the recovered α and β are used as input for the parallel flow linear stability analysis. A detailed description of the input parameters and eigenvalue results are shown in table 3.7.

Figure 3.8 shows the adjoint sensitivity eigenmode (a) and the associated Fourier coefficients (b) corresponding to $\alpha = 1$ and $\beta = 0$. Note that the streamwise and spanwise velocity components are negligible as shown in figure 3.8b. This adjoint mode highlights that the associated direct eigenmode in §3.1.4 is most sensitive to spanwise point momentum forcing near the center of the channel. Figure 3.9 shows an additional adjoint

Reference	ω_1 $[\alpha = 1,\ \beta = 0]$	ω_2 $[\alpha = 1,\ \beta = 1.5]$
Juniper *et al.* (2014)	$-2.33610 \times 10^{-2} + \mathrm{i}0.977640$	$-2.56110 \times 10^{-2} + \mathrm{i}0.977640$
From §3.1.4	$-2.33374 \times 10^{-2} \pm \mathrm{i}0.977638$	$-2.55906 \times 10^{-2} \pm \mathrm{i}0.977638$
Present	$-2.33374 \times 10^{-2} \pm \mathrm{i}0.977638$	$-2.55906 \times 10^{-2} \pm \mathrm{i}0.977638$

Table 3.7: Two leading eigenvalues (ω_1 and ω_2) from adjoint sensitivity for laminar channel flow at $Re = 1000$ are compared to results from parallel (Juniper *et al.*, 2014) and global linear stability. Streamwise wavenumbers, α, and spanwise wavenumbers, β, are observed in the global adjoint eigenmodes (see figures 3.2 and 3.3) and are used as input to the parallel flow stability analysis of Poiseuille flow. The parallel flow stability results are produced using a code available in the supplementary material by Juniper *et al.* (2014).

sensitivity eigenmode (a,b) and its associated Fourier coefficients (c) corresponding to $\alpha = 1$ and $\beta = 1.5$. Looking at this adjoint eigenmode, we can conclude that streamwise point momentum forcing near the center of the channel is what the direct eigenmode is most sensitive to. Additionally, wall-normal and spanwise forcing are about 12% and 30% as effective at generating a response. Table 3.7 shows how the eigenvalues from the different analyses compare. Note the good agreement between parallel linear stability and the global linear/adjoint analyses, as well as the degree of precision to which the global linear stability and global adjoint sensitivity eigenvalues are coincident with each other.

3.3 Optimal perturbation

3.3.1 Lid-driven cavity validation

Validation for optimal perturbation analysis is performed using the lid-driven cavity at $Re = 1000$, using the same baseflow that was used to validate linear stability and adjoint sensitivity. Recall from §2.4 that performing optimal perturbation analysis requires forward integration through the LNS and then a corresponding integration backwards in time through the adjoint LNS to solve for the optimal modes. Since the direct

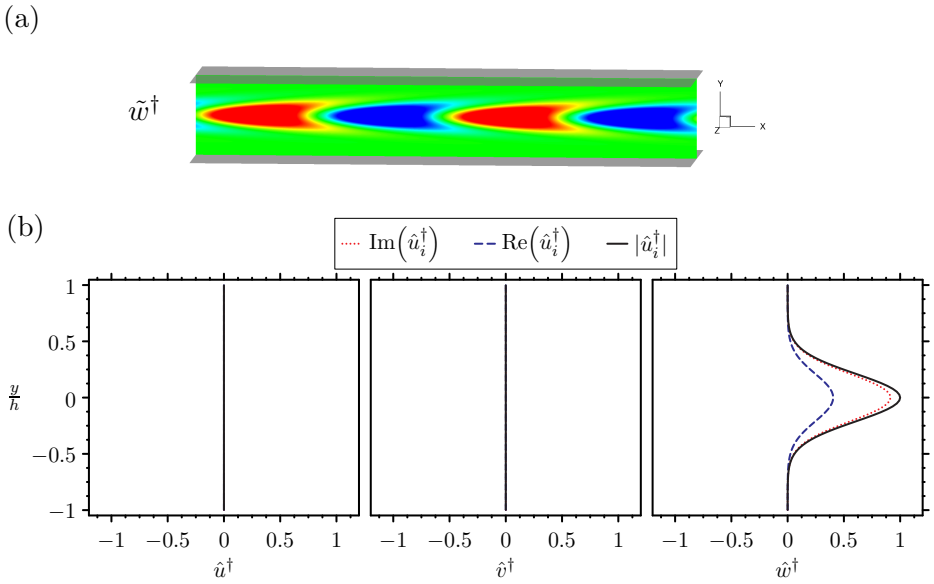

Figure 3.8: Real part of the first adjoint eigenmode corresponding to the first adjoint sensitivity eigenvalue ω_1 in table 3.7 for laminar channel flow at $Re = 1000$. Here, there is no variation in the z-direction, making a single slice sufficient to display all relevant data. The results are shown as an x-y slice ($z = 0$) with contours of $\tilde{w}^\dagger$ (note: $\tilde{u}^\dagger = \tilde{v}^\dagger = 0$). The streamwise and spanwise wavenumbers ($\alpha = 1$, $\beta = 0$) are extracted and used as input to classic parallel flow stability analysis of Poiseuille flow. Additionally, the adjoint sensitivity eigenmode Fourier coefficients ($\hat{u}_i^\dagger$) are computed and shown in (b).

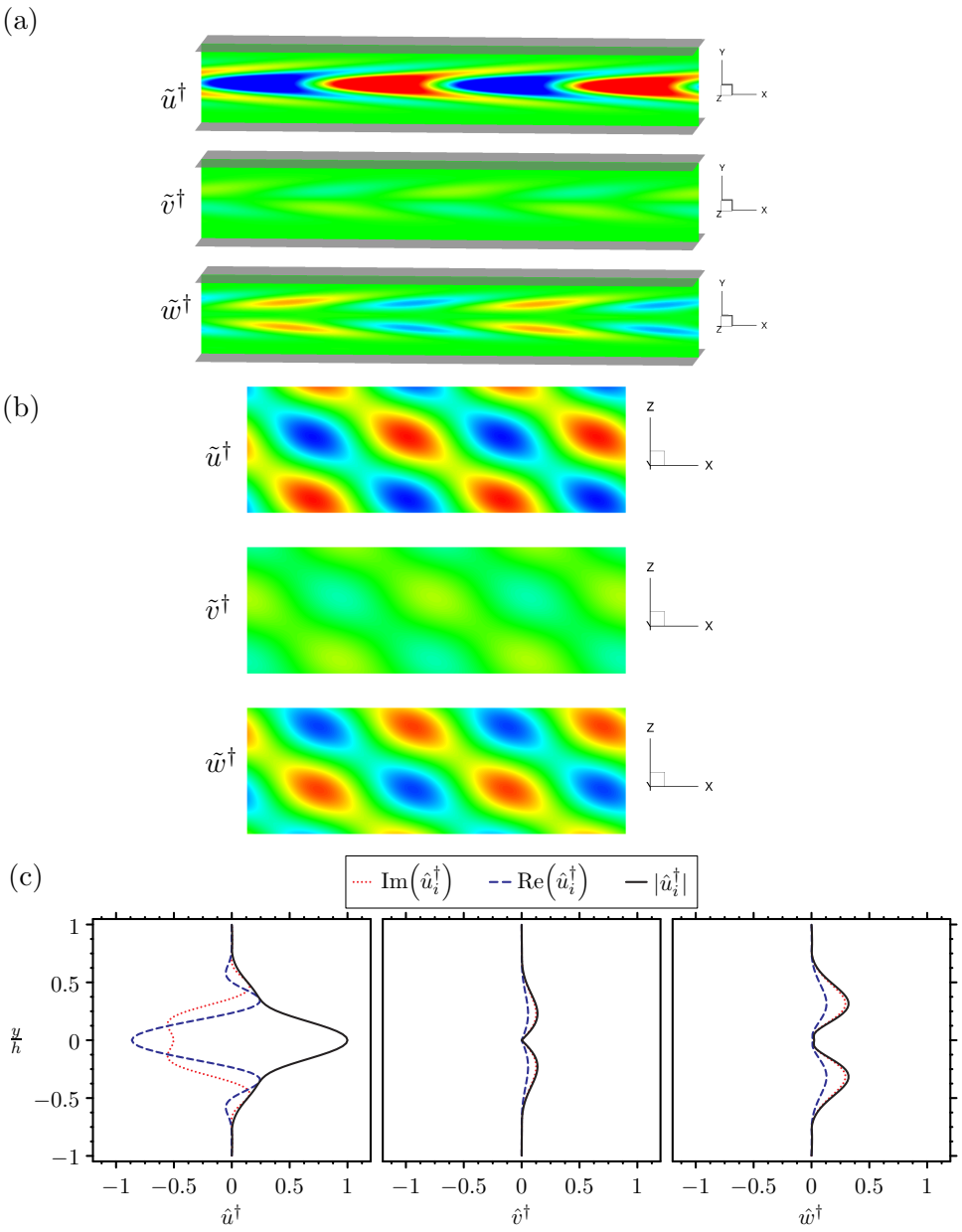

Figure 3.9: Real part of the second adjoint eigenmode corresponding to the eigenvalues ω_2 in table 3.7 from adjoint sensitivity for laminar channel flow at $Re = 1000$. The results are shown as x-y ($z = 0$) and $z - x$ ($y = 0.25$) slices with contours of $\tilde{u}^\dagger$, $\tilde{v}^\dagger$, and $\tilde{w}^\dagger$. The adjoint sensitivity eigenmode Fourier coefficients ($\hat{\boldsymbol{u}}_i^\dagger$) are shown for completeness (c).

Re	τ	λ	$E(\tau = 3)/E(0)$	|% Difference|
1000	3.0	6.056	6.058	0.03%
		5.870	5.872	0.03%
		3.884	3.884	0.01%
		3.389	3.387	0.06%
		3.173	3.163	0.33%
		3.129	3.118	0.35%
		2.277	2.277	0.00%
		2.117	2.112	0.20%
		1.948	1.945	0.15%
		1.893	1.889	0.17%
		1.799	1.796	0.18%
		1.792	1.788	0.20%
		1.483	1.476	0.48%
		1.554	1.549	0.37%

Table 3.8: Details are shown for validation of optimal perturbation analysis for a cubic lid-driven cavity at $Re = 1000$. A characteristic time-scale of 3 was chosen, which is non-dimensionalized by the lid velocity and cavity dimension. The leading eigenvalue λ and the observed energy growth are compared as a % difference of λ.

and adjoint integrators, as well as the IRAM, are used for linear stability and adjoint sensitivity, the validation for optimal perturbation analysis may be streamlined. Barkley *et al.* (2008) shows that an efficient way to validate optimal perturbation analysis is to compare the leading eigenmode and eigenvalue for a specific τ to the observed energy growth when the eigenmode is provided as a perturbation to the LNS over the same time τ. Barkley *et al.* (2008) show that:

$$\frac{E(\tau)}{E_0} \approx \lambda, \tag{3.4}$$

where λ is the eigenvalue from optimal perturbation analysis. Therefore, the eigenvalue is compared to the observed perturbation energy growth over τ to ensure that the energy growth is captured correctly.

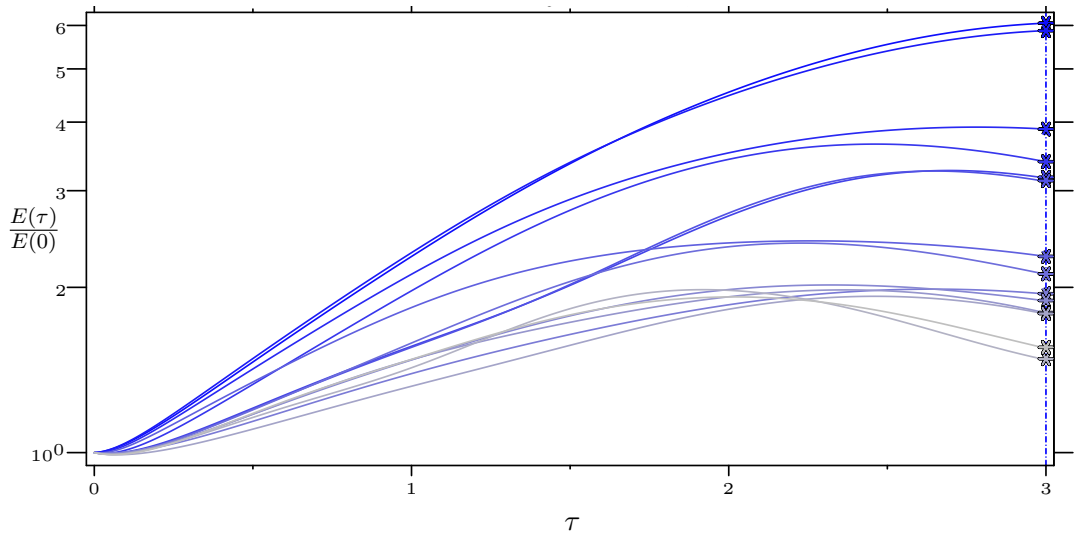

Figure 3.10: Validation for lid-driven cavity at Re=1000 for optimal perturbation analysis. The energy growths are plotted as lines of different shades of blue, and the corresponding eigenvalues, λ, are shown as symbols at $\tau = 3$.

Optimal perturbation analysis results are shown in figure 3.10 by using the leading optimal perturbations as input to the LNS and integrating forward for $\tau = 3$ time units. The eigenvalues are also shown in figure 3.10 as symbols along the vertical blue-dashed line in colors that match the corresponding growth line. The resulting eigenvalues λ from optimal perturbation analysis are quantitatively compared in table 3.8. The comparison between the optimal perturbation eigenvalue λ and the observed growth demonstrates good agreement for the 14 leading perturbations. The leading 4 optimal modes are also visualized in figure 3.11 with a-d being the initial perturbation, and e-h being the solution at τ.

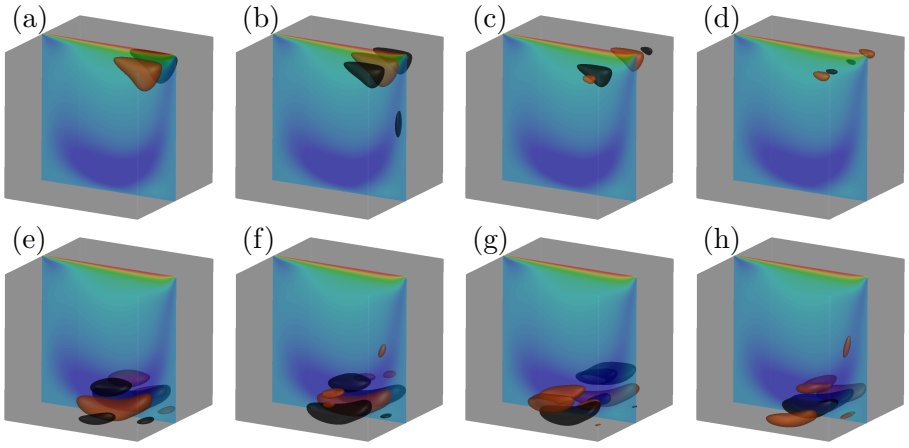

Figure 3.11: The first four leading optimal perturbations (corresponding to table 3.8) showing the initial perturbations (a-d) and their evolution at τ (e-h) for the lid-driven cavity.

Chapter 4

Linear Stability Analysis of the Jet in Cross-flow

Global linear stability analysis of the JICF is performed in this chapter. The simulation setup is described in §4.1, and is the same setup used in chapters 5-6. The results are discussed in §4.2.

4.1 Problem Description

Figure 4.1 shows the simulation set-up. At the inflow, a laminar Blasius boundary layer profile is prescribed. The computational grid and boundary layer profile are the same as those used by Iyer & Mahesh (2016). The boundary layer has been shown to match well with experiments at $x/D = -5.5$. The jet nozzle is located at the origin of the computational domain and is included in all simulations. It has been shown by Iyer & Mahesh (2016) that the jet nozzle plays a crucial role in setting up the mean flow near the jet exit, thus affecting the stability characteristics of the flow. A fifth-order polynomial is used to model the nozzle shape used in the experiments of Megerian *et al.* (2007). The jet exit diameter D is 3.81 mm and the average velocity at the jet exit $\overline{v}_{jet}$ is 8 m s^{-1}. Additional simulation details are outlined in table 4.1. Simulation cases $R2$ and $R4$ are performed at the same conditions as the experiments of Megerian *et al.*

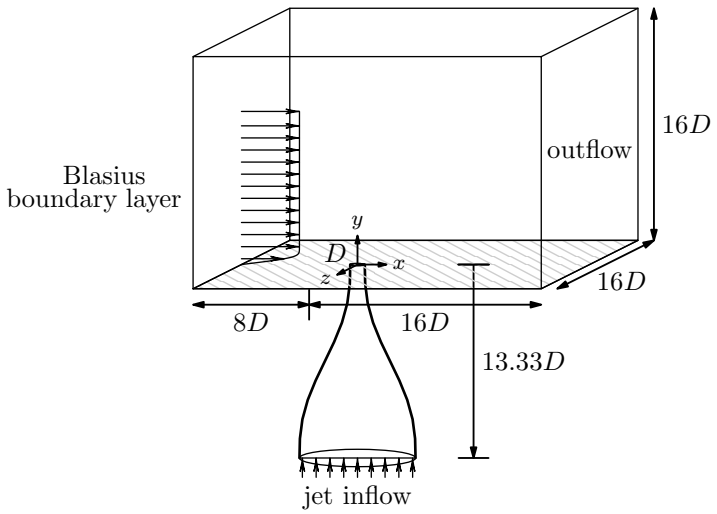

Figure 4.1: A schematic of the jet in cross-flow computational domain is shown. The origin is located at the center of the jet exit. A Blasius boundary layer is prescribed as the leftmost inflow condition. Additionally, uniform inflow is prescribed for the jet inflow. The nozzle shape is modelled using a 5th order polynomial that matches the nozzle used in experiments of Megerian *et al.* (2007).

(2007).

The unstructured capabilities of the solver allow the cross-flow domain and jet nozzle to be simulated together. Figure 4.1 also describes the extent of the computational domain. The domain extends $8D$ upstream of the jet exit to the inflow boundary where the Blasius laminar boundary layer solution is applied. $16D$ downstream of the jet exit is the outflow boundary. In addition, Neumann boundary conditions are applied to the sides located $8D$ from the origin in the spanwise directions. The simulated nozzle extends $13.33D$ below the jet orifice, at which point a uniform inflow is prescribed to achieve the correct velocity at the jet exit. The top of the domain is located $16D$ above the origin and also has a Neumann boundary condition applied.

The computational grids are shown in figures 4.2 and 4.3, and are made up of 80 and 138 million elements, respectively. First, details regarding the 80 million element grid are discussed. There are 80 elements inside of the inflow laminar boundary layer in the y-direction and 400 elements around the jet exit. Downstream of the jet exit, the grid

Case	R	$R^* = v_{\text{jet,max}}/u_\infty$	Re	$Re_{\text{cf}} = Du_\infty/\nu_\infty$	θ_{bl}/D
$R2$	2	2.44	2000	1000	0.1215
$R4$	4	4.72	2000	500	0.1718

Table 4.1: Details are shown for the simulations used to study the stability of the JICF. Jet to cross-flow ratios R of 2 and 4 are studied at a Reynolds number Re of 2000, based on the average velocity $\overline{v}_{\text{jet}}$ at the jet exit and the jet exit diameter D. Also shown is the jet to cross-flow ratio R^*, based on the jet exit peak velocity $v_{\text{jet,max}}$, and the Reynolds number Re_{cf}, based on the cross-flow velocity u_∞. The momentum thickness of the laminar cross-flow boundary layer is described at the jet exit when the jet is turned off.

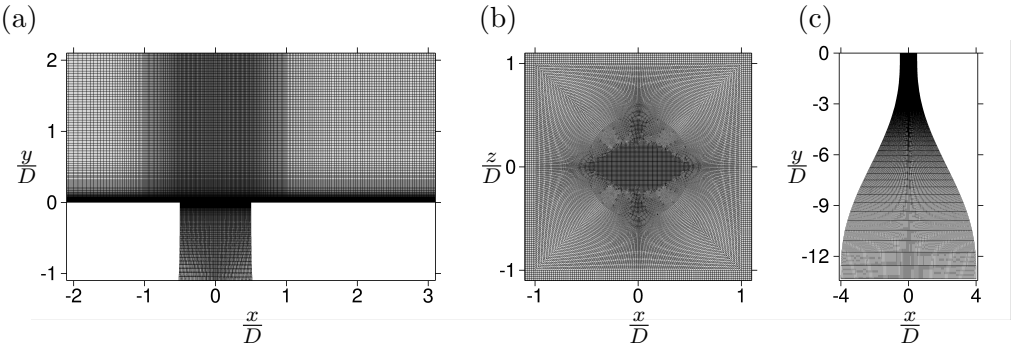

Figure 4.2: The 80 million element computational grid is shown. A view of the symmetry plane (a), as well as a wall normal plane near the jet exit (b), and the nozzle (c) are shown.

maintains a spacing of $\Delta x/D = 0.033$ and $\Delta z/D = 0.02$, with $\Delta y_{\text{min}}/D = 0.0013$, which are finer than the spacings used by Muppidi & Mahesh (2007) to simulate a turbulent JICF. After making the assumption that downstream of the jet exit the boundary layer is turbulent, viscous wall units may be computed (e.g. $\Delta x^+ = \frac{\Delta x u_\tau}{\nu}$). The local wall shear stress is used to calculate the friction velocity ($u_\tau = \sqrt{\tau_w/\rho} = \sqrt{\nu(d\overline{u}/dy|_{y=0})}$). Wall spacings at the outflow Δx^+, Δy^+_{min}, and Δz^+, are computed to be 2.74, 0.1, and 1.66 for case $R2$ and 1.48, 0.058, and 0.89 when $R = 4$.

For the 138 million grid, 86 elements are inside of the inflow laminar boundary layer and 320 elements are around the jet exit. Additionally, downstream of the jet nozzle exit, grid spacings of $\Delta x/D = 0.029$ and $\Delta z/D = 0.02$, with $\Delta y_{\text{min}}/D = 0.0013$ are maintained. Compared to the 80 million element grid, this grid is refined in the jet nozzle

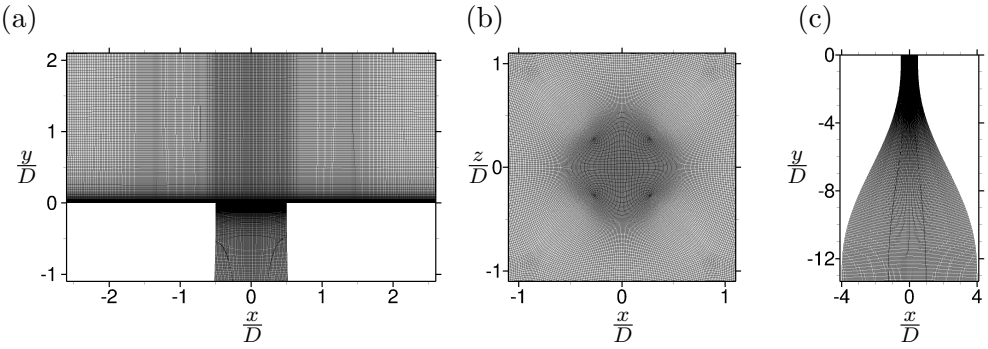

Figure 4.3: The refined, 138 element computational grid that is used in linear stability, adjoint sensitivity and optimal perturbation analyses is shown. A view of the symmetry plane (a), as well as a wall normal plane near the jet exit (b), and the nozzle (c) are shown.

and cross-flow boundary layer. Grid resolution in terms of wall units are $\Delta x^+ = 2.10$, $\Delta y^+_{\text{min}} = 0.09$, and $\Delta z^+ = 1.45$ for case $R2$ and $\Delta x^+ = 1.09$, $\Delta y^+_{\text{min}} = 0.05$, and $\Delta z^+ = 0.75$ for case $R4$.

Instantaneous isocontours of Q-criterion (eq. 3.1) colored by streamwise velocity for the turbulent flowfield are shown in figure 4.4 for case $R2$ (a) and $R4$ (b). The complexity of the turbulent JICF is illustrated by these instantaneous results. Important features include the coherent upstream shear-layer roll up, as well as long string-like wake vortices near the wall. Additionally, downstream shear-layer roll up is seen that interacts with the upstream shear-layer at the collapse of the potential core. Many fine scale turbulent structures are also visible downstream in the jet wake. In the section that follows, linear stability results are discussed that provide valuable insight to the stability of these two flow configurations.

The turbulent mean flows that are used as the base states are shown in figure 4.5 for the 138 million element grid. Except for chapter 4, results using the 138 million element are reported. The turbulent mean flows for the 80 million element grid were generated by Iyer & Mahesh (2016) using 32000 and 39000 temporal samples for case $R2$ and $R4$, respectively. Iyer & Mahesh (2016) have shown that there is good agreement between the temporally-averaged solutions from simulation and experiment. Similarly, for the 138 million element grid, 54000 and 70000 samples are used for case $R2$ and $R4$,

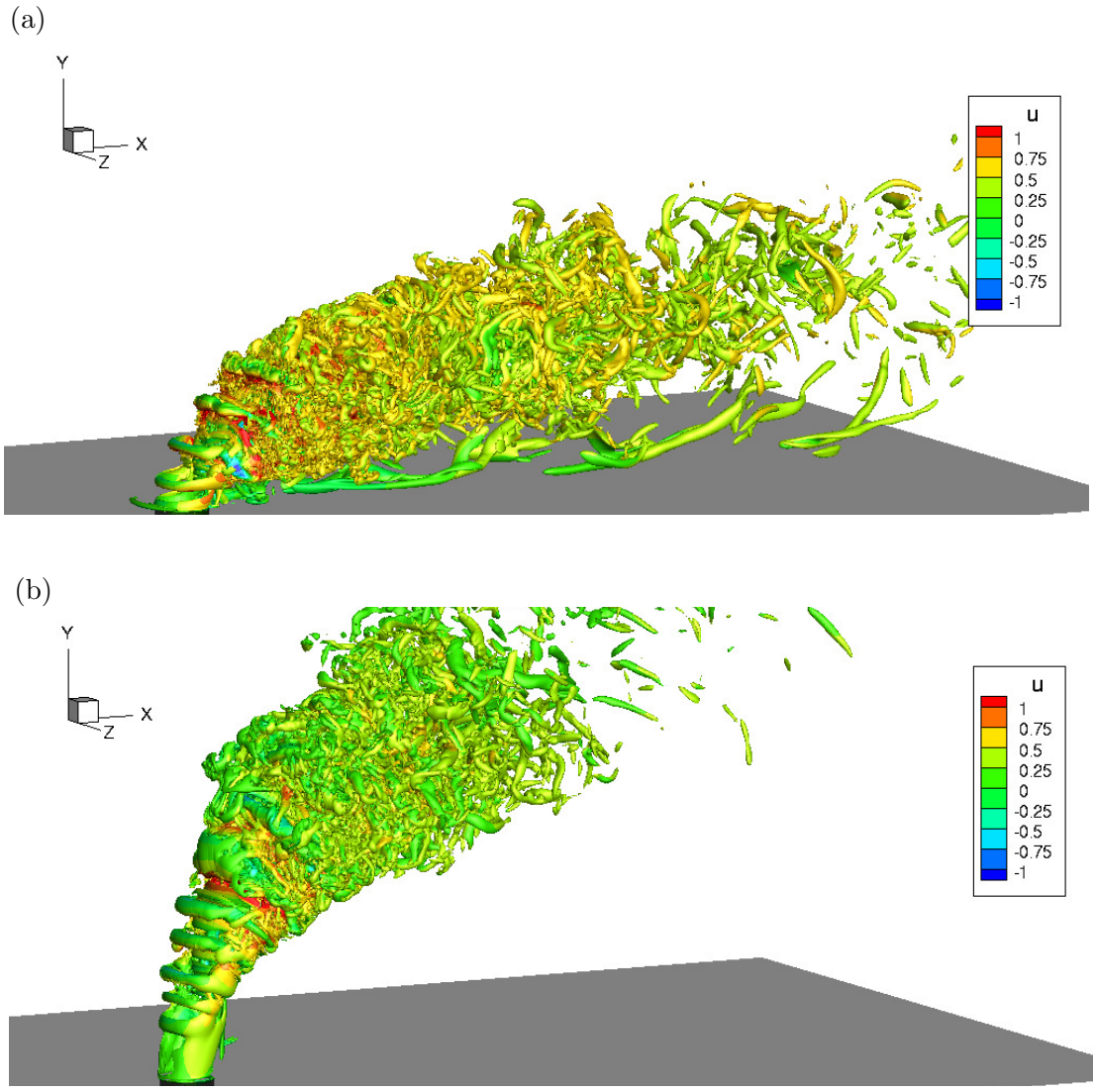

Figure 4.4: Isocontours of Q-criterion colored by streamwise velocity for the instantaneous turbulent flowfield for $R = 2$ (a) and $R = 4$ (b).

respectively.

4.2 Results

Global linear stability analysis is performed for the $R2$ and $R4$ cases described in table 4.1. These cases match the experimental and computational set-ups of Megerian *et al.* (2007) and Iyer & Mahesh (2016), respectively. Choosing an appropriate baseflow is important for linear stability analysis. The scale-separation argument from chapter 2.2 provides the following results:

$$\begin{aligned} L/\eta &= Re^{3/4} \approx 300 \\ t_L/t_\eta &= Re^{1/2} \approx 45 \end{aligned} \tag{4.1}$$

This shows that 1 or more orders of magnitude separate the time and length scales of turbulent motions and the motions of interest. Selective frequency damping (SFD) has been shown by Bagheri *et al.* (2009) to alter some important features of the JICF; specifically the collapse of the potential core and the near-wall reverse flow downstream of the jet exit. Therefore, turbulent mean flow solutions are used as the base states for linear stability analysis.

A grid convergence study was performed to study the sensitivity of the leading eigenvalue, for three different grids and $R = 2$. The upstream shear-layer eigenvalue was computed for a coarse grid (10 million elements), normal grid (80 million elements) and a finer grid (99 million elements). All three eigenvalues are shown in figure 4.6, and show good agreement. Peplinski *et al.* (2015) have shown that the leading eigenvalue can be sensitive to the size of the computational domain. Iyer & Mahesh (2016) have shown that the domain size in their DNS successfully captures both the upstream boundary layer and upstream shear-layer frequencies when compared to experiment. We use the same domain length as Iyer & Mahesh (2016).

For case $R2$, the 15 leading eigenvalues were computed to a maximum residual of 1e$-$14. In addition, 60 Arnoldi vectors were generated for each iteration in the IRAM. The LNS (eq. 2.11) were integrated 0.114 time units (non-dimensionalized by

(a)

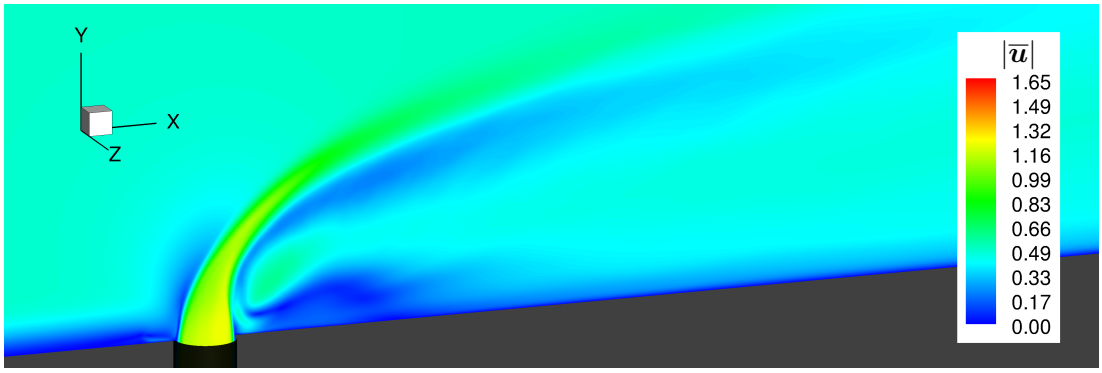

(b)

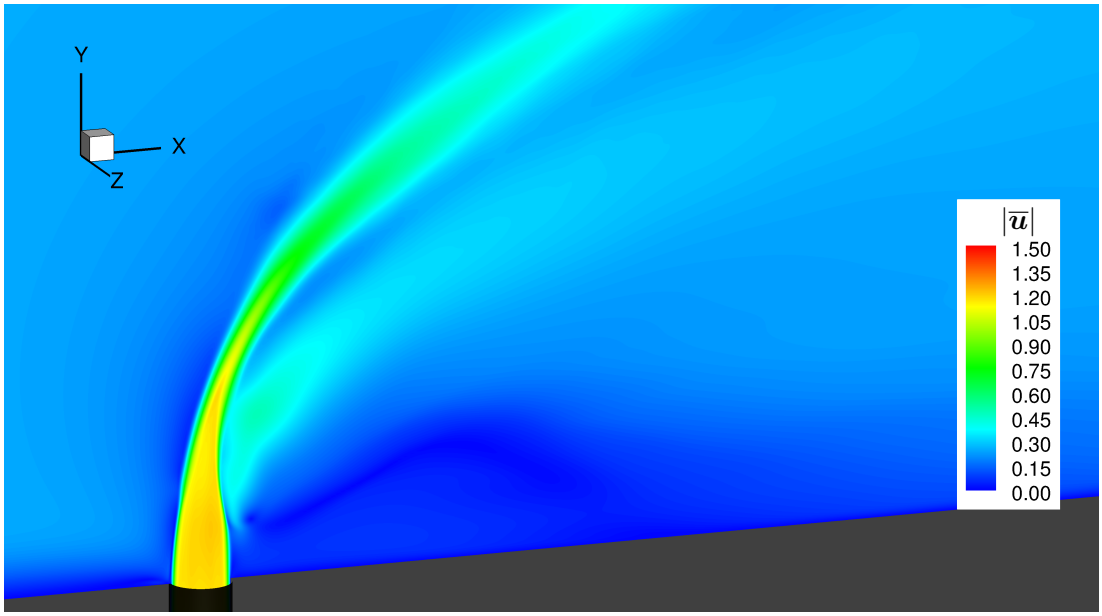

Figure 4.5: Cross-sectional views of the turbulent mean flows at the symmetry plane that are used as the base states for linear stability, adjoint sensitivity, and optimal perturbation analyses for cases $R2$ (a) and $R4$ (b). Contours of velocity magnitude $|\overline{\boldsymbol{u}}|$ are shown.

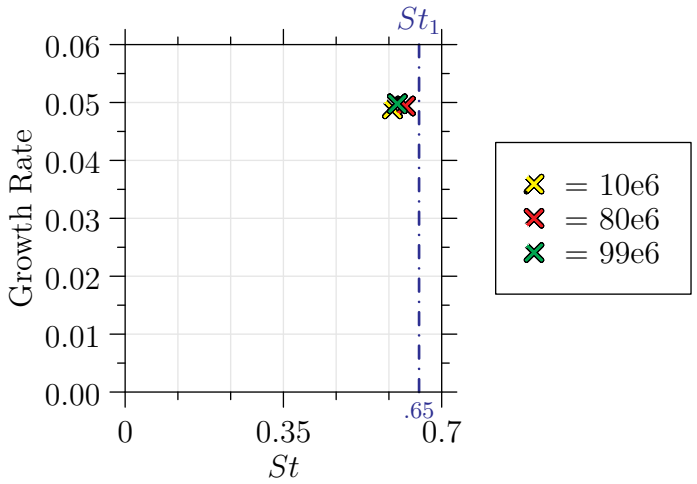

Figure 4.6: Results from the grid convergence study used to determine the sensitivity of the leading eigenvalue to the mesh for case $R2$. Three different grids were tested: coarse (10 million elements), normal (80 million elements), fine (99 million elements). St_1 highlights the primary Strouhal number observed along the upstream shear-layer in simulations by Iyer & Mahesh (2016).

$D/v_{\text{jet,max}}$) to generate each Arnoldi vector. This ensures adequate temporal resolution of the highest upstream shear-layer frequency observed in DNS, $St = 0.65$ (i.e. period of 1.54 time units). The 60 Arnoldi vectors that were generated spanned 6.85 time units, allowing the IRAM to efficiently resolve the lower frequency wake modes as well.

Similarly for case $R4$, the 16 leading eigenvalues were computed to the same maximum residual of 1e$-$14. In addition, 100 Arnoldi vectors were generated for each iteration in the IRAM. The solution was integrated to 0.157 time units to generate each Arnoldi vector. This ensures adequate temporal resolution to capture the highest upstream shear-layer frequency in DNS, $St = 0.39$ & $St = 0.78$ (i.e. periods of 2.56 and 1.28 time units, respectively). Once the 60 Arnoldi vectors were generated, they spanned 15.7 time units, allowing the IRAM to efficiently resolve lower frequency modes.

Figure 4.7 shows the eigenvalue spectra obtained from linear stability analysis for cases $R2$ (a) and $R4$ (b). The eigenvalues are non-dimensionalized such that the growth rate is $\text{Re}(\frac{\omega}{2\pi})D/v_{\text{jet,max}}$ and the Strouhal number, St, is $\text{Im}(\frac{\omega}{2\pi})D/v_{\text{jet,max}}$. As discussed in §2.2, Barkley (2006) and Turton *et al.* (2015) showed that when performing linear

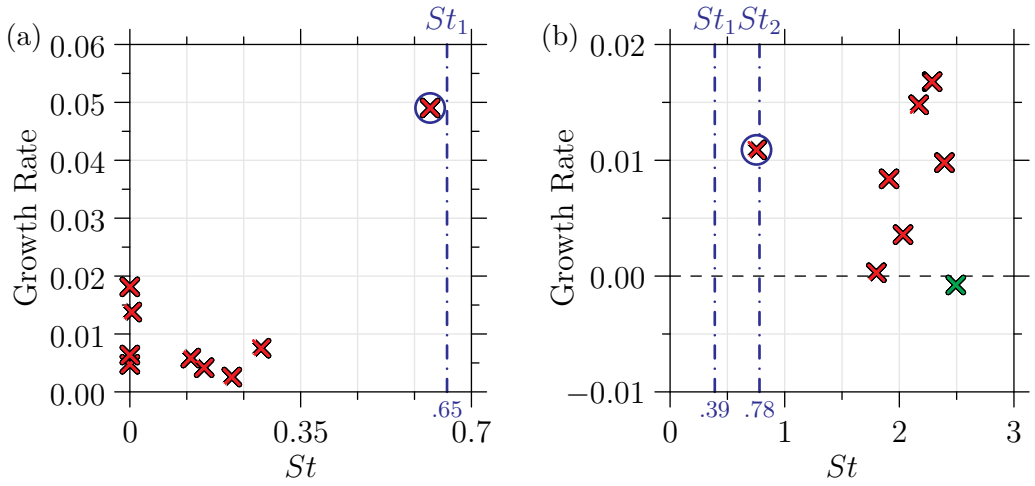

Figure 4.7: Linear stability analysis spectrum for the JICF at $Re = 2000$ for $R = 2$ (a) and $R = 4$ (b). The vertical blue dashed lines correspond to most dominant frequencies from DNS vertical velocity spectra in the upstream shear-layer obtained by Iyer & Mahesh (2016). The DNS frequency of $St_2 = 1.3$ from Iyer & Mahesh (2016) is not shown in (a) as it would obscure the lower frequency linear stability results. Eigenvalues (ω_j) with red symbols are unstable modes (i.e. positive growth rate), while stable values are colored green. The circled eigenvalues have their corresponding eigenmodes shown in Figure 4.8 for $R = 2$ (a) and $R = 4$ (b).

stability analysis around a turbulent mean flow, the resulting eigenvalues have very small growth rates; which is consistent with the results in figure 4.7. The circled eigenvalues have Strouhal numbers closest to those found in experiments (Megerian *et al.*, 2007) and simulations (Iyer & Mahesh, 2016) (i.e. St_1 ($R2$), St_2 ($R4$)) when analyzing vertical velocity spectra from the upstream shear-layer. The eigenvalues from linear stability analysis have Strouhal numbers associated with the upstream shear-layer of 0.62 for $R2$ and 0.75 for $R4$. Comparatively, vertical velocity spectra show that Strouhal numbers of 0.65 for $R2$ and 0.78 for $R4$ dominate the upstream shear-layer. Figure 4.8 provides an isometric view of the two eigenmodes for $R2$ (a) and $R4$ (b), that are associated with the circled eigenvalues in figure 4.7.

The eigenmodes from linear stability analysis are compared to the modes from dynamic mode decomposition (DMD). DMD (Rowley *et al.*, 2009; Schmid, 2010) modes have a frequency and growth rate that can describe the dynamics of a nonlinear system as a generalization of the global eigenmodes of a linear system (i.e. the infinite-dimensional linear Koopman operator). DMD modes of the JICF were determined by Iyer & Mahesh (2016) using snapshots of the nonlinear turbulent flowfield. The DMD modes are shown in figure 4.8 for $R2$ (c,e) and $R4$ (d,f). Additionally, figure 4.9 shows cross-sectional views of the upstream shear-layer eigenmodes and DMD modes at the symmetry plane ($z = 0$). The DMD results from Iyer & Mahesh (2016) have Strouhal numbers of 0.65 and 1.3 for $R2$ and 0.39 and 0.78 for $R4$, that match the frequencies from vertical velocity spectra. For case $R4$, it is not as clear how the eigenmode and DMD modes compare from figure 4.8(b,d,f) alone. However, the cross-sectional views in figure 4.9 show that the eigenmode at $St = 0.75$ (figure 4.9b) agrees well qualitatively with the DMD mode at $St = 0.78$ (figure 4.9f). Most importantly, the DMD modes confirm that the spectral peaks in the DNS and experiment correspond to upstream shear-layer modes.

Linear stability analysis for case $R2$ predicts an eigenmode at $St = 0.62$ originating near the jet exit and propagating along the upstream shear-layer. DMD and vertical velocity spectra capture $St = 0.65$ and a higher harmonic at $St = 1.3$ along the upstream

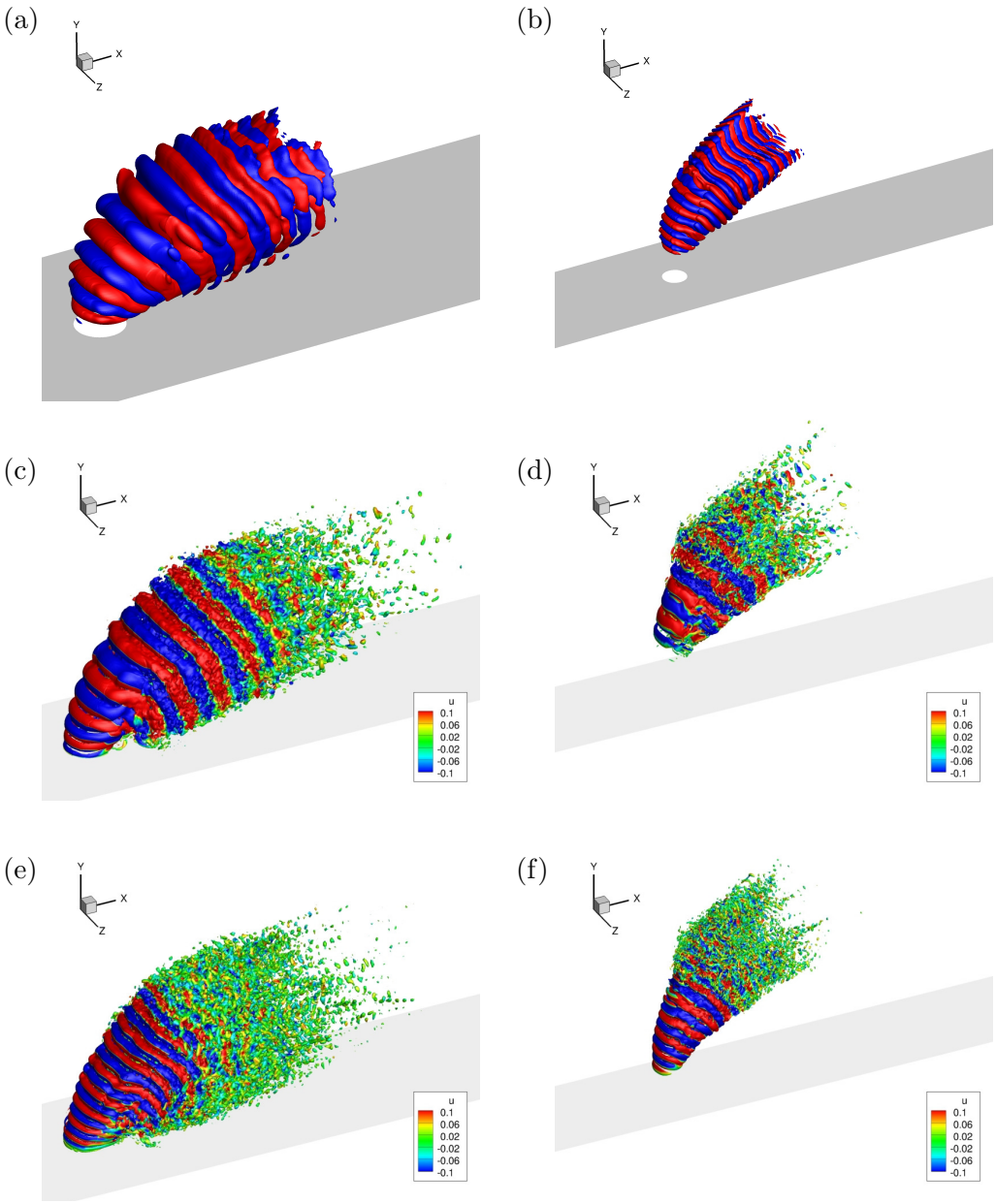

Figure 4.8: Real part of the eigenmodes for case $R2$ at $St = 0.62$ (a) and $R4$ at $St = 0.75$ (b) are shown with positive and negative isocontours of $\tilde{u}$ and $\overline{v}$. Isocontours of Q-criterion for the DMD modes by Iyer & Mahesh (2016) are shown for $R2$ at $St = 0.65$ (c) and $St = 1.3$ (e) and for $R4$ at $St = 0.39$ (d) and $St = 0.78$ (f).

shear-layer. It is clear from the isometric views in figure 4.8 that the upstream shear-layer eigenmode at $St = 0.62$ (figure 4.8a) and DMD mode at $St = 0.65$ (figure 4.8c) for case $R2$ agree well qualitatively. Additionally, figure 4.9 shows good agreement for the cross-sectional plots between the eigenmodes and DMD modes when $R = 2$. As expected, linear stability analysis does not predict the non-linear higher harmonic at $St = 1.3 \approx 0.65 \times 2$.

For case $R4$, linear stability analysis predicts an eigenmode at $St = 0.75$ along the upstream shear-layer, while DMD and vertical velocity spectra show $St = 0.39$ and a harmonic at $St = 0.78$. Iyer & Mahesh (2016) have shown $St = 0.78$ to include about 43% of the spectral energy when compared to the dominant DMD mode ($St = 0.39$). However, note that the DMD mode at $St = 0.78$ presents itself much closer to the nozzle and is clearly a shear-layer mode. $St = 0.39$, on the other hand, has its largest magnitude further downstream and is located between the upstream and downstream shear-layers. This can be observed in the cross-sectional view as a part of figure 4.9d.

Rowley *et al.* (2009) compared the JICF linear stability analysis results of Bagheri *et al.* (2009) with DNS and DMD. They showed that linear stability recovers an upstream shear-layer instability mode with a different frequency than what is captured by DNS and DMD. Bagheri *et al.* (2009) computed a steady-state baseflow using SFD. Additionally, the jet nozzle was not included in the simulation and a top-hat jet exit profile was prescribed. Interestingly, the presented work shows that using the turbulent mean flow as the base state in linear stability analysis, the captured upstream shear-layer instability mode has the same frequency as the DNS and DMD results of Iyer & Mahesh (2016).

4.2.1 Stability analysis of case $R2$

Figure 4.10 shows the eigenmodes that are associated with the eigenvalues in figure 4.7a for case $R2$. To better characterize the eigenmodes, they are grouped according to their frequencies and spatial structures. For this case, we notice that there are three main groups.

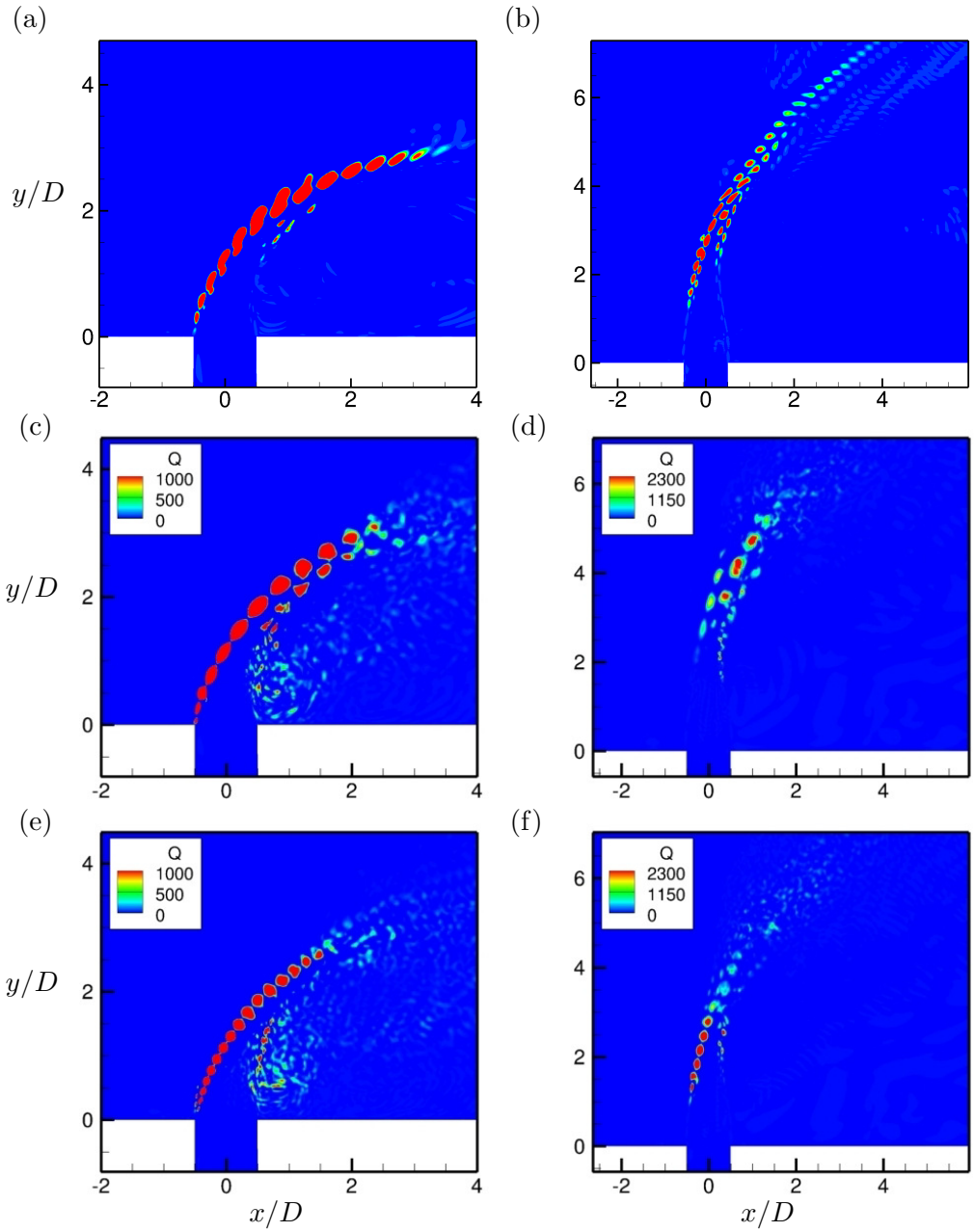

Figure 4.9: Slices of eigenmodes and DMD modes (Iyer & Mahesh, 2016) at the symmetry plane ($z = 0$) with contours of Q-criterion. The eigenmodes have frequencies of $St = 0.62$ (a) and $St = 0.75$ (b) for $R = 2$ and $R = 4$, respectively. The DMD modes have frequencies for case $R2$ at $St = 0.65$ (c) and $St = 1.3$ (e) and case $R4$ at $St = 0.39$ (d) and $St = 0.78$ (f).

The first group consists of the shear-layer mode seen in figure 4.10a. This eigenmode oscillates at a frequency very close to what is observed in DNS and experiments. Additionally, it originates near the jet exit at the initiation of the upstream shear-layer. Furthermore, this eigenmode extends downstream after the collapse of the potential core while still maintaining a large magnitude. This implies that the eigenmode is growing as it travels downstream but also growing at the jet exit; characteristic of an absolute instability.

Next is the group that occupies a range of lower frequencies that may be identified as the wake modes. This group consists of figures 4.10b-e. Low frequencies have been shown by Iyer & Mahesh (2016) to include a significant portion of the spectral energy, highlighting their importance to the overall flow physics for this configuration. The four wake modes are qualitatively similar, but exhibit different spatial length scales. Additionally, the lower frequency wake modes highlight the connection between the near wall motions, and motions deep in the jet wake. The wake modes originate behind the downstream shear-layer after the collapse of the potential core and dominate far downstream. Figure 4.10b-c shows the eigenmodes that persist downstream, but remain in the jet wake. Specifically, the eigenmodes observed in figure 4.10d-e correspond to the lowest of frequencies for this configuration. The observed frequencies are consistent with the notion that Strouhal numbers associated with the jet diameter D will be lower than those associated with the shear-layer.

The Reynolds stresses present in the turbulent mean flow show up in linear stability analysis as stationary eigenmodes. This is because the Reynolds stress term becomes a steady forcing term in the LNS equations once the baseflow equations are subtracted (eq. 2.11). The stationary eigenmodes are not relevant to the present analysis and are not included.

4.2.2 Stability analysis of case $R4$

Eigenmodes for case $R4$ are shown in figure 4.11, and are associated with the eigenvalues in figure 4.7b. Again, it is convenient to group the eigenmodes. We observe from the spectrum in figure 4.7b and the eigenmodes from figure 4.11 that there are two main

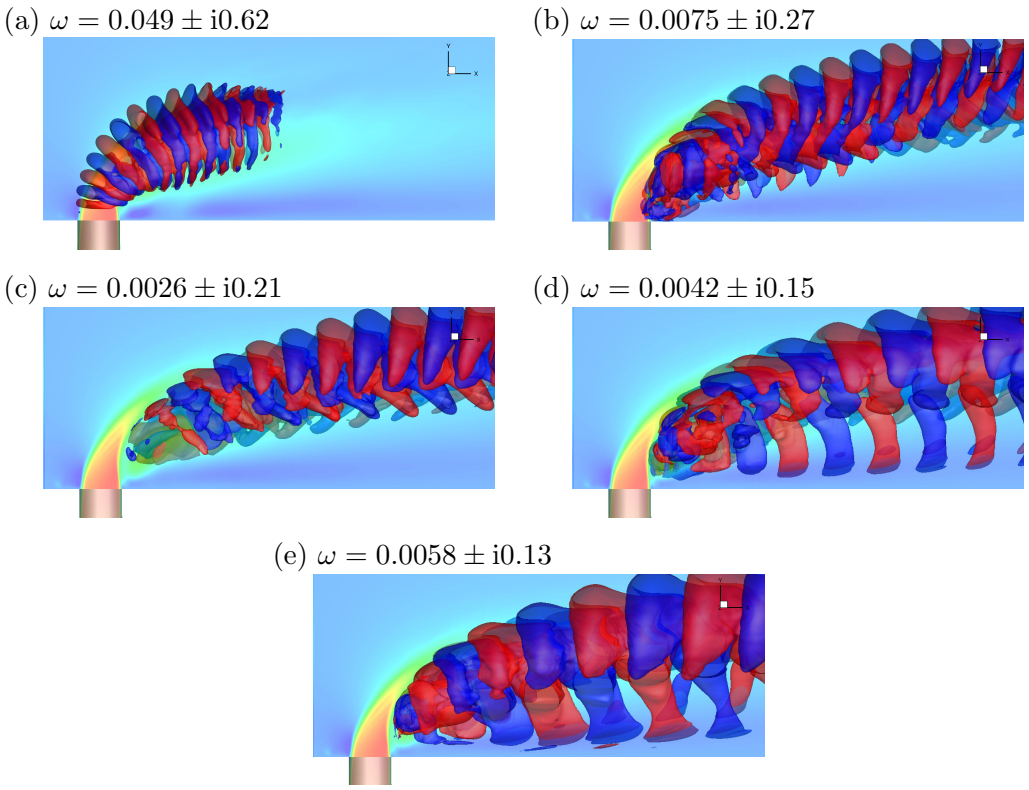

Figure 4.10: Real part of the eigenmodes for case $R2$ are shown with positive and negative isocontours of $\tilde{u}$ and $\overline{v}$ contours of the base state in the background. The eigenvalues are shown above, with the real part being the growth rate, and the imaginary part being the Strouhal number. Mode (a) corresponds to the most unstable and highest frequency upstream shear-layer mode. Modes (b-e) are lower frequency and originate near the downstream shear-layer and travel far downstream. Modes (d) and (e) also show a connection between near-wall motions and motions in the jet wake.

groups.

The high frequency eigenmodes make up the first group. These eigenmodes are all located along the downstream shear-layer. Not much attention has been paid to the stability of the downstream shear-layer. However, the present work shows that two of the downstream shear-layer modes have higher growth rates than the upstream shear-layer, and therefore must not be ignored when considering the stability at $R = 4$. Note that the downstream shear-layer modes occupy a range of frequencies. All of these modes interact with the upstream shear-layer at the collapse of the potential core. This may explain why different frequencies are present along the shear-layer as seen from upstream shear-layer vertical velocity spectra for $R = 4$.

Case $R4$ has been shown to change its dominant frequencies along the upstream shear-layer; unlike case $R2$. When $R = 4$, the upstream shear-layer eigenmode at $St = 0.75$ originates farther away from the jet when compared to the upstream shear-layer mode of case $R2$. This is consistent with a convective instability where the instability travels downstream, but does not grow at the point of origin (i.e. near the jet exit).

4.3 Summary

Linear stability analysis has been shown to successfully capture the upstream shear-layer instabilities at the same Strouhal numbers as those found using DNS and DMD analysis of Iyer & Mahesh (2016). Linear stability analysis has also provided supporting evidence for the upstream shear-layer's transition from absolute to convective instability as R increases from 2 to 4. The present work has shown that the downstream shear-layer plays an important role in the stability of the JICF at higher R values.

The spectrum for case $R2$ (figure 4.7a) shows that the eigenvalue with the highest growth rate has a frequency of $St = 0.62$. Its associated eigenmode observed in figure 4.8a is located along the upstream shear-layer. Leveraging this knowledge by either attempting to dampen or amplify the upstream shear-layer mode near the jet exit can be an effective control strategy in applications. However, farther downstream, this mode has a dramatic reduction in amplitude, which suggests this mode is only dominant $4-5D$

(a) $\omega = 0.017 \pm \mathrm{i}2.3$ (b) $\omega = 0.0010 \pm \mathrm{i}2.4$

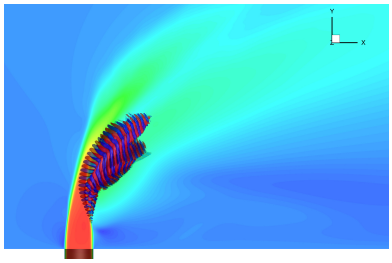
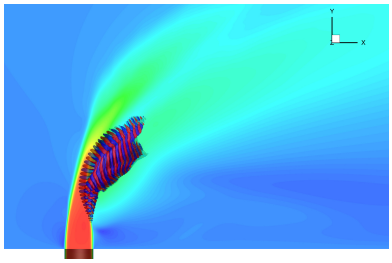

(c) $\omega = 0.015 \pm \mathrm{i}2.2$ (d) $\omega = -0.00077 \pm \mathrm{i}2.5$

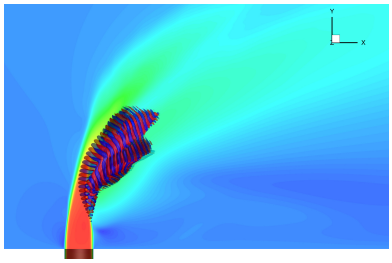
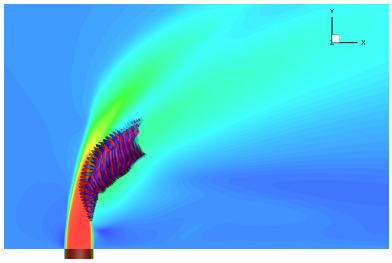

(e) $\omega = 0.0084 \pm \mathrm{i}1.9$ (f) $\omega = 0.0036 \pm \mathrm{i}2.0$

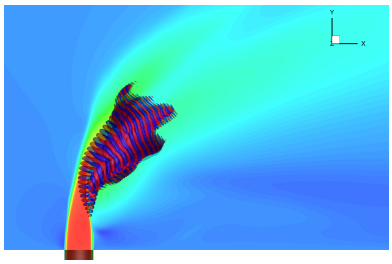
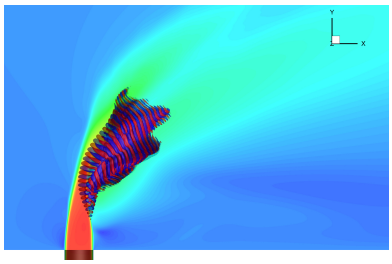

(g) $\omega = 0.00029 \pm \mathrm{i}1.8$ (h) $\omega = 0.011 \pm \mathrm{i}0.75$

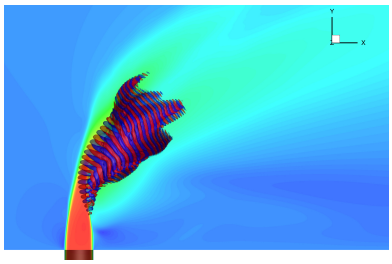
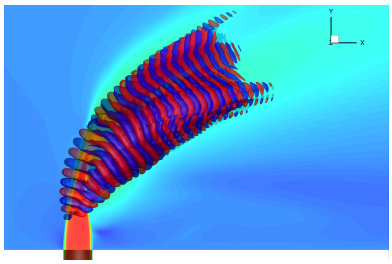

Figure 4.11: Real part of the eigenmodes for case $R4$ are shown with positive and negative isocontours of $\tilde{u}$ and $\overline{v}$ contours of the base state in the background to highlight the jet baseflow. The associated eigenvalues are shown above, with the real part being the growth rate, and the imaginary part being the Strouhal number. Modes (a-g) correspond to the higher frequency downstream shear-layer modes. Mode (h) is associated with the upstream shear-layer.

downstream of the jet orifice. The rest of the spectrum for $R = 2$ has growth rates less than 30% of the growth rate for the upstream shear-layer mode. However, the spatial structure of these lower frequency modes reveals that they continue to have a large impact far downstream. This behavior could be important when attempting to control the JICF. For example, if mixing downstream is important, dampening or amplifying these unstable wake modes may be more effective than trying to control the upstream shear-layer instability. Note that the origin of the wake modes appears to be slightly above the jet orifice, which makes it unclear how effective actuation in the nozzle or near the jet orifice may be.

For case $R4$, linear stability analysis has again been shown to capture the relevant flow physics. Unlike the $R2$ case, the analysis spectrum for case $R4$ in figure 4.7b shows that the most unstable eigenvalue is not associated with the upstream shear-layer. Instead, the most unstable eigenvalue resides on the downstream shear-layer, and is accompanied by a range of other eigenvalues also located along the downstream shear-layer. These downstream shear-layer eigenvalues have a range of Strouhal numbers from about $1.7 - 2.5$. Not much attention has been paid to the downstream shear-layer in the past; the present work suggests that for higher R values, it should not be ignored.

Chapter 5

Adjoint Sensitivity Analysis of the Jet in Cross-flow

This chapter presents results from the adjoint analysis of cases $R2$ and $R4$. §5.1 discusses the behavior in the upstream shear-layer, CVP, downstream of the jet exit and downstream shear-layer, respectively. A brief summary in §5.2 concludes the chapter.

5.1 Results

Figure 5.1 shows the eigenvalues from linear stability (see chapter 4) and adjoint sensitivity analyses. The eigenvalues are again non-dimensionalized such that the growth rate is $\mathrm{Re}(\frac{\omega}{2\pi})D/v_{\mathrm{jet,max}}$ and the Strouhal number, St, is $\mathrm{Im}(\frac{\omega}{2\pi})D/v_{\mathrm{jet,max}}$. Note that the adjoint eigenvalues match those from linear stability, and agree well with the upstream shear-layer spectra results (i.e. vertical blue-dashed lines in figure 5.1, St_1(a) and St_2(b)) from experiments (Megerian *et al.*, 2007) and simulations (Iyer & Mahesh, 2016).

In this chapter, eigenmodes from linear stability analysis are shown using isocontours of the streamwise (x-direction) perturbation velocity, $\mathrm{Re}(\hat{u}) = \pm 0.0003$. Adjoint sensitivity analysis eigenmodes are presented using isocontours of the vertical (y-direction) adjoint perturbation velocity, $\mathrm{Re}(\hat{v}^\dagger) = \pm 0.0001$, which highlight regions

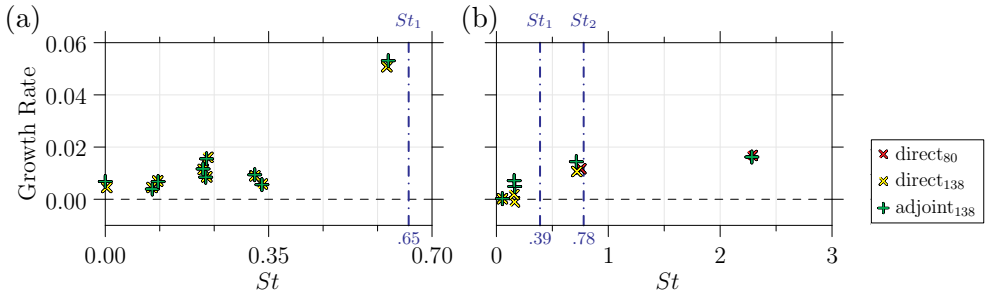

Figure 5.1: Eigenvalues from linear stability and adjoint sensitivity for $R2$ (a) and $R4$ (b). The blue-dashed lines correspond to the dominant frequencies observed within the upstream shear-layer by Iyer & Mahesh (2016). The legend subscripts refer to results from the 80 million and 138 million grids.

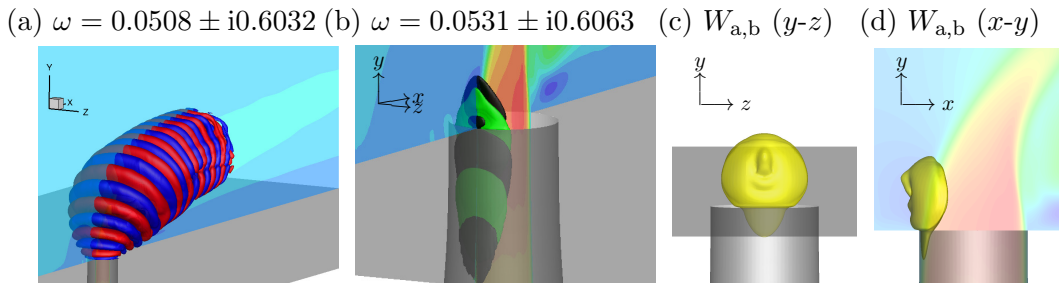

Figure 5.2: The $R2$ upstream shear-layer linear stability (a) and adjoint sensitivity analyses (b) eigenmodes along with their associated wavemaker (c-d). Symmetry plane contours show the vertical velocity of the baseflow $\overline{v}$.

most sensitive to vertical point momentum forcing. Eigenmodes are normalized such that $\|\hat{u}\| = \left\|\hat{v}^{\dagger}\right\| = 1$.

5.1.1 Upstream shear-layer

The upstream shear-layer linear stability eigenmodes for both case $R2$ (figure 5.2a) and case $R4$ (figure 5.3) were discussed in detail in chapter 4. Recall that the main difference between the direct (i.e. linear stability analysis) eigenmodes for each case is that for case $R2$ the mode originates near the jet exit plane, whereas for $R4$ the mode is elevated.

The adjoint eigenmodes (figures 5.2b and 5.3b) show that the direct modes are most sensitive to y-direction momentum forcing along the upstream side of the jet nozzle,

(a) $\omega = 0.0107 \pm \mathrm{i}0.7190$ (b) $\omega = 0.0144 \pm \mathrm{i}0.7146$ (c) $W_{\mathrm{a,b}}$ (y-z) (d) $W_{\mathrm{a,b}}$ (x-y)

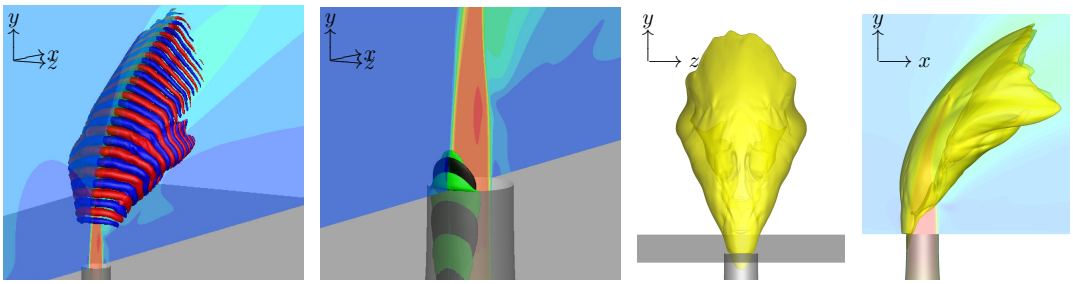

Figure 5.3: Similar to figure 5.2, but for the $R4$ upstream shear-layer.

near the jet exit. Interestingly, for $R2$ the wavemaker region (figure 5.2c-d) is localized along the upstream side of the nozzle. Conversely, $R4$ (figure 5.3c-d) is most sensitive to localized feedback along the entire upstream shear-layer.

The wavemaker results are consistent with the notion that the upstream shear-layer region transitions from absolute to convective instability as R changes from 2 to 4. For $R2$, the region most sensitive to localized feedback is dominated by the formation of the upstream shear-layer, which is in direct contrast to case $R4$, which is sensitive to localized feedback along the entire upstream shear-layer. The tonal nature of case $R2$ is due to the fact that the location where the shear-layer roll-up forms is where localized feedback is strongest. Case $R4$ is not only weaker, but includes harmonics due to the wavemaker region extending along the upstream shear-layer.

5.1.2 Asymmetries in the CVP

Smith & Mungal (1998) studied the JICF experimentally, and determined that at high jet-to-cross-flow ratios ($R > 10$) asymmetries may form in the time-averaged CVP. Getsinger *et al.* (2014) have also observed asymmetric mean CVP cross-sections in their experiments. They conclude that an absolutely unstable JICF ($R2$) is less likely to exhibit asymmetric mean profiles when compared to the weaker, convectively unstable JICF ($R4$). The reason why the JICF behaves asymmetrically is not fully understood; specifically the reason why there is a preferential direction in certain configurations.

In the present work, we observe significant asymmetries in some eigenmodes. The

(a) $\omega = 0.0090 \pm \mathrm{i}0.3203$ (b) $\omega = 0.0094 \pm \mathrm{i}0.3202$ (c) $W_{\mathrm{a,b}}$ (y-z) (d) $W_{\mathrm{a,b}}$ (x-y)

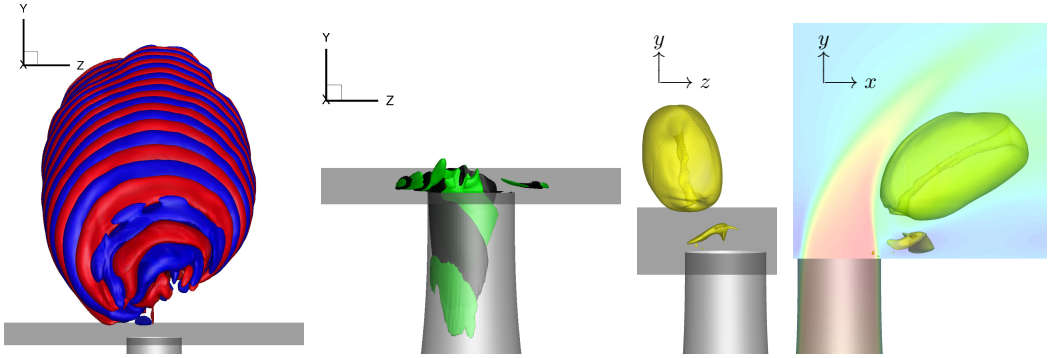

Figure 5.4: Similar to figure 5.2, but for the $R2$ *left-leaning* asymmetric eigenmodes.

(a) $\omega = 0.0018 \pm \mathrm{i}0.1559$ (b) $\omega = 0.0071 \pm \mathrm{i}0.1588$ (c) $W_{\mathrm{a,b}}$ (y-z) (d) $W_{\mathrm{a,b}}$ (x-y)

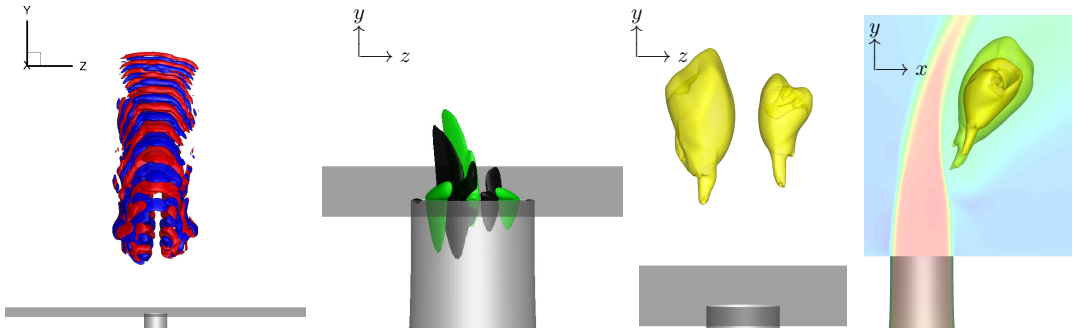

Figure 5.5: Similar to figure 5.2, but for the $R4$ *left-leaning* asymmetric eigenmodes.

direct (a) and adjoint (b) eigenmodes in figure 5.4 for case $R2$, and figure 5.5 for case $R4$ are *left-leaning* and correspond to a wavemaker region biased towards the left side. Conversely, additional eigenmodes (not shown) are mirrored across the symmetry plane, and are *right-leaning*. The adjoint eigenmodes (b) are most sensitive to vertical point momentum forcing in a similar way as the upstream shear-layers, but with biases to each side. The wavemakers (c-d) are located along the CVP, directly behind the collapse of the jet potential core. By animating the linear stability analysis eigenmodes (not shown) it is seen that the eigenmodes for both cases rotate with the CVP.

Linear stability analysis results for case $R2$ originate much closer to the jet nozzle exit compared to case $R4$. The adjoint modes provide valuable information regarding the sensitivity of these asymmetric instabilities to y-direction point momentum forcing. Note the spatial and temporal length scales that characterize the regions where asymmetric instabilities are most sensitive. For instance, adjoint sensitivity analysis results for case $R2$ (figure 5.4b) show much longer length scales in the circumferential direction just below the jet nozzle exit when compared to case $R4$ (figure 5.5b). This knowledge, in conjunction with the frequency information gathered from animating (not shown) the adjoint sensitivity analysis eigenmodes, provide valuable information regarding the best location and frequencies to excite asymmetries.

Growth rates from the linear stability and adjoint sensitivity analyses are often discussed in terms of their relative strength. We can compute the relative strength of the asymmetric eigenmodes for each case by comparing them to the strength of their respective upstream shear-layer growth rates. The difference $\Delta\omega_{R2}$ between the growth rates of asymmetric eigenmodes and the upstream shear-layer eigenmodes for case $R2$ is in the range $0.042 \leq \Delta\omega_{R2} \leq 0.047$. However, for the $R4$ case, the difference $\Delta\omega_{R4}$ is in the range $0.014 \leq \Delta\omega_{R4} \leq 0.009$. Notice $\Delta\omega_{R2} > \Delta\omega_{R4}$ over their entire ranges, suggesting that asymmetric modes and sensitivity to experimental asymmetries are more significant for $R4$ than $R2$; consistent with experimental results (Smith & Mungal, 1998; Getsinger *et al.*, 2014).

(a) $\omega = 0.0114 \pm \mathrm{i}0.2098$ (b) $\omega = 0.0116 \pm \mathrm{i}0.2095$ (c) $W_{\mathrm{a,b}}$ (y-z) (d) $W_{\mathrm{a,b}}$ (x-y)

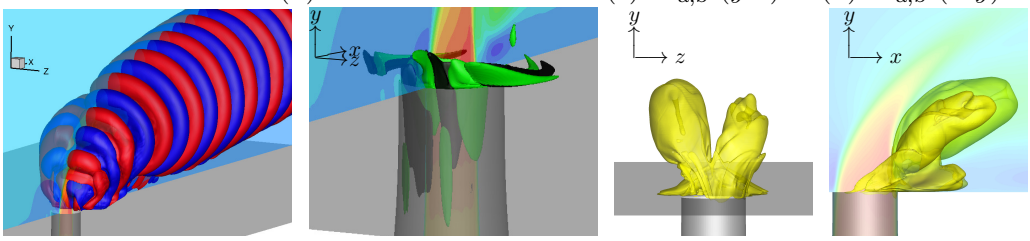

Figure 5.6: Similar to figure 5.2, but for a representative pair of $R2$ downstream eigenmodes.

(a) $\omega = 0.0002 \pm \mathrm{i}0.0539$ (b) $\omega = 0.0002 \pm \mathrm{i}0.0532$ (c) $W_{\mathrm{a,b}}$ (y-z) (d) $W_{\mathrm{a,b}}$ (x-y)

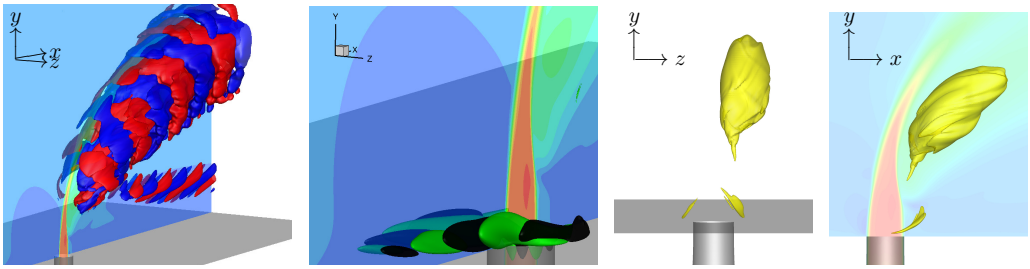

Figure 5.7: Similar to figure 5.2, but for the $R4$ lowest frequency eigenmodes.

5.1.3 Downstream of the jet exit

Figure 5.6 shows one of the pairs of downstream linear stability and adjoint sensitivity eigenmodes that have lower frequencies and longer length scales as compared to those previously discussed for case $R2$. Additionally, they persist far downstream along the wall. Adjoint sensitivity analysis (b) reveals sensitivities in the jet nozzle near the exit, but also in the region where the incoming cross-flow wraps around the jet nozzle exit; hinting at an increased sensitivity to perturbations from within the cross-flow boundary layer. The wavemaker region (c-d) reveals some minor asymmetries in the sensitivity to localized feedback, but is largely symmetric between each side of the CVP.

Looking at case $R4$, the lowest frequency pair of eigenmodes is shown in figure 5.7. The linear stability analysis eigenmode (a) has larger spatial length scales than all previous eigenmodes, and also branches downward towards the wall. There is a bias towards the right-side of the symmetry plane. Adjoint sensitivity analysis (b) shows that

(a) $\omega = 0.0168 \pm \mathrm{i}2.2861$ (b) $\omega = 0.0162 \pm \mathrm{i}2.2834$ (c) $W_{\mathrm{a,b}}$ (y-z) (d) $W_{\mathrm{a,b}}$ (x-y)

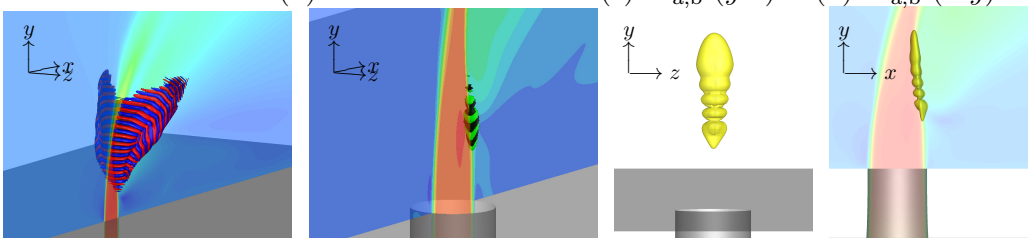

Figure 5.8: Similar to figure 5.2, but for the $R4$ leading downstream shear-layer eigenmodes (circled in figure 5.1b). Note that (a) is generated using the 80 million grid.

the largest sensitivity is not around the jet nozzle exit, but is upstream of the jet nozzle exit within the cross-flow boundary layer. Fric & Roshko (1994) performed experiments that studied the wake vortices of the JICF by seeding the incoming cross-flow boundary layer and discovered that wake vortices could be visualized, leading to the conclusion that fluid inside the incoming cross-flow boundary layer travelled downstream to form wake vortices. Adjoint sensitivity analysis results are consistent with these experiments, by showing there is a connection between perturbations in the cross-flow boundary layer and downstream of the jet exit near the wall. The wavemaker highlights the asymmetry, which implies that it is likely that a mirrored low frequency pair of eigenmodes also exists.

5.1.4 Downstream shear-layer

First shown in chapter 4, the eigenvalue with the highest growth rate for case $R4$ is associated with the downstream shear-layer and is shown in figure 5.8 (a). It is intuitive that as R becomes large, the upstream and downstream side of the JICF become indistinguishable, making it acceptable that the downstream shear-layer is important to case $R4$, but not for case $R2$. The linear stability analysis eigenmode is elevated from the jet nozzle exit and is located along the downstream side of the jet. This instability is most sensitive at the formation of the downstream shear-layer. This region would be difficult to actuate in a control application, since it would most likely be invasive to the flowfield.

The wavemaker is located where the downstream shear-layer forms. By building upon the previous analysis, figure 5.8c-d shows the localization of the wavemaker, which has a strong resemblance to the absolutely unstable upstream shear-layer of case $R2$ (figure 5.2). It is therefore natural to identify this region of the downstream shear-layer as absolutely unstable. Furthermore, an extension to higher values of R would suggest a critical value R_{crit} exists, at which point the downstream shear-layer region becomes convectively unstable, characterized by a non-localized downstream shear-layer wavemaker region.

5.2 Summary

The sensitivity of the upstream shear-layer mode to vertical point momentum forcing is largest along the upstream side of the jet nozzle for both cases $R2$ and $R4$. Wavemaker results are consistent with the upstream shear-layer stability transition. For case $R2$, the wavemaker is localized near the jet exit, but for case $R4$ the wavemaker is a large region along the upstream shear-layer, and is consistent with the transition from absolute to convective instability.

Asymmetric linear stability and adjoint sensitivity eigenmodes are observed, with *left-leaning* and *right-leaning* direct eigenmodes being most sensitive to vertical forcing on the left- and right-sides, respectively. Additionally, the asymmetric direct modes reside on the CVP. By examining relative growth rates, it is suggested that the asymmetric modes are more relevant to the overall dynamics for case $R4$. Additionally, the spatial length-scales of the adjoint modes provide insight for control strategies.

Direct eigenmodes persist far downstream, and are most sensitive to forcing in the jet nozzle near the exit as well as around the jet nozzle exit. The main difference in case $R4$ for the direct mode is that there is a clear branch that extends downward towards the wall. Additionally, the adjoint sensitivity region extends upstream into the cross-flow boundary layer, highlighting the connection between the cross-flow boundary layer and the near-wall region downstream.

For case $R4$ only, a representative pair of downstream shear-layer modes are shown

which are consistent with the fact that as R increases, the downstream shear-layer and the upstream shear-layer become indistinguishable. A connection is drawn between the wavemakers of the upstream and downstream shear-layers for case $R2$ and $R4$, respectively, which leads to the conclusion that the downstream shear-layer region can be absolutely unstable.

Chapter 6

Optimal Perturbation Analysis of the Jet in Cross-flow

The JICF is studied using optimal perturbation analysis in this chapter. Several different optimization times are chosen relative to the characteristic time-scale of the upstream shear-layer roll-up. In §6.1, the results are introduced and the observed growth is verified. Optimal perturbations for cases $R2$ and $R4$ are then discussed separately §6.2 and §6.3. A summary of the results is provided in §6.4.

6.1 Results

Global optimal perturbation analysis is performed for the same cases described in table 4.1. The same turbulent mean flows from adjoint sensitivity analysis are used as the baseflows for optimal perturbation analysis, using the 138 million grid.

For cases $R2$ and $R4$, the 19 leading optimal perturbations were computed to a maximum residual of 1e$-$14. 40 Arnoldi vectors were generated for each iteration in the IRAM. For optimal perturbation analysis the LNS equations (eq. 2.11) were integrated τ time units (non-dimensionalized by $D/v_{\text{jet,max}}$) and then the adjoint LNS equations (eq. 2.35) were used to integrate backwards τ time units for each Arnoldi vector. Different τ values were chosen relative to the observed frequency of the upstream shear-layer.

Case	τ	$\max(\lambda)$	$\max(E(\tau)/E(0))$	|% Difference|	Type
$R2$	0.4	2.26×10^1	2.28×10^1	0.94%	Asymmetric
	0.8	1.14×10^2	1.20×10^2	4.55%	Asymmetric
	1.6	1.14×10^3	1.05×10^3	7.35%	Down SL
	3.2	2.87×10^4	2.71×10^4	5.62%	Up SL
	4.9	6.72×10^5	6.16×10^5	8.29%	Up SL
$R4$	0.4	1.54×10^1	1.48×10^1	4.09%	Down SL
	0.8	1.27×10^2	1.20×10^2	5.07%	Down SL
	1.6	6.18×10^3	5.72×10^3	7.35%	Down SL
	3.1	1.97×10^6	1.79×10^6	9.24%	Down SL
	4.7	4.27×10^7	4.16×10^7	2.48%	Hybrid

Table 6.1: Details are shown for optimal perturbation analysis used to study the transient stability of the JICF. Several different time horizons are chosen that are shorter and longer than the characteristic time-scale of the upstream shear-layer, $1/St_{up}$ (see text). Additionally, the leading eigenvalue λ and the observed energy growth are compared as a % difference of λ. Note that the "upstream shear-layer" and "downstream shear-layer" are abbreviated as "Up SL" and "Down SL", respectively.

For case $R2$, $1/St_{\text{up}} = 1.54$, and for case $R4$, $1/St_{\text{up}} = 1.28$. This allowed study of optimal perturbations over times less than, equal to, and greater than the characteristic time-scale for each case.

Figures 6.1 and 6.2 show the results from optimal perturbation analysis for the different τ outlined in table 6.1. Note that the horizontal axis is linear in time, and the vertical axis is logarithmic in energy growth. Different colors are used for different values of τ, with vertical dash-dotted lines in the same color intercepting the x-axis at τ. Along the vertical colored lines, the eigenvalues are plotted in order to make a visual comparison between the eigenvalue λ from optimal perturbation analysis and the energy growth obtained by applying the associated perturbation to the baseflow, and integrating over the time τ using the LNS. Additionally, each eigenvalue is labeled with a short description of the optimal perturbation shape, with similar modes grouped together. Finally, the characteristic time-scale of the upstream shear-layer is marked with a vertical dashed-line in black.

Table 6.1 also describes the maximum growth observed for different τ, and how well the eigenvalue and observed growth agree. Overall, good agreement is observed as the error is shown to be less than $< 10\%$. For a computational domain with inflow and outflow boundaries, this error is reasonable due to the fact that any perturbation that escapes the domain will no longer be included in the overall perturbation kinetic energy. To reduce the amount of error between the eigenvalue and observed growth, the domain would need to be extended to allow perturbations to travel further before escaping the computational domain. This effect can be observed in table 6.1 by noting how the % difference is generally larger for greater values of τ.

In the following sections, these figures, and the associated optimal perturbation modes will be discussed in detail. Both cases are organized into three subsections describing short-, characteristic-, and long-time horizons. The optimal perturbation modes are shown using either an isometric view, or a side-view in an xy-plane. The optimal perturbations are visualized using iso-contours of the vertical perturbation velocity, $\tilde{v}$, at levels equal to ± 0.001 colored as orange and black, respectively. Additionally, for the isometric view, contours of the vertical velocity of the baseflow, $\overline{v}$, are shown for the

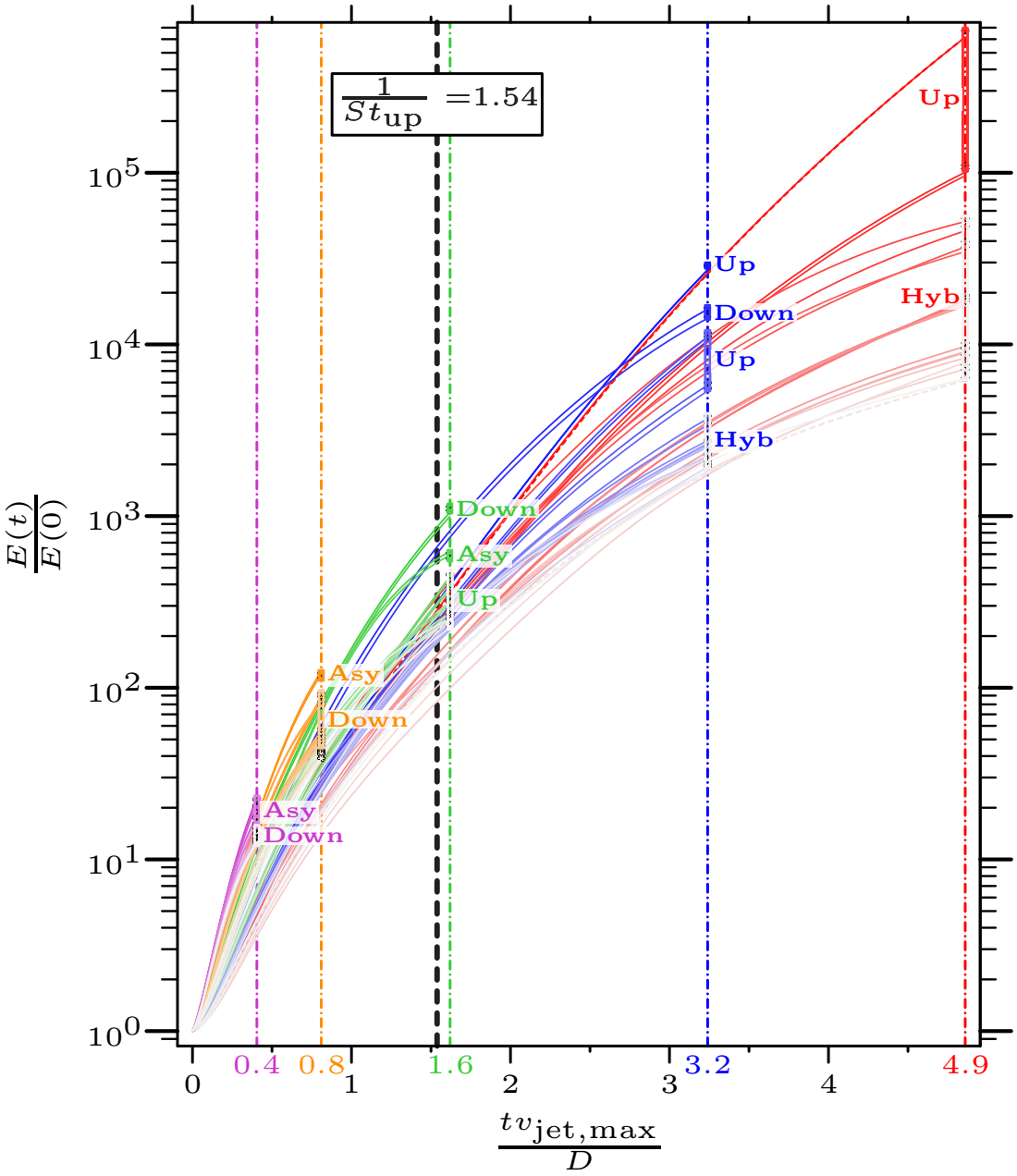

Figure 6.1: Transient growth is shown for case $R2$, optimized for different τ, which are differentiated by color and the vertical dash-dotted lines. Additionally, the upstream shear-layer characteristic time-scale, $1/St_{\mathrm{up}}$, is shown as a vertical black dashed line to provide temporal context. Eigenvalues for different τ are shown on their associated vertical lines.

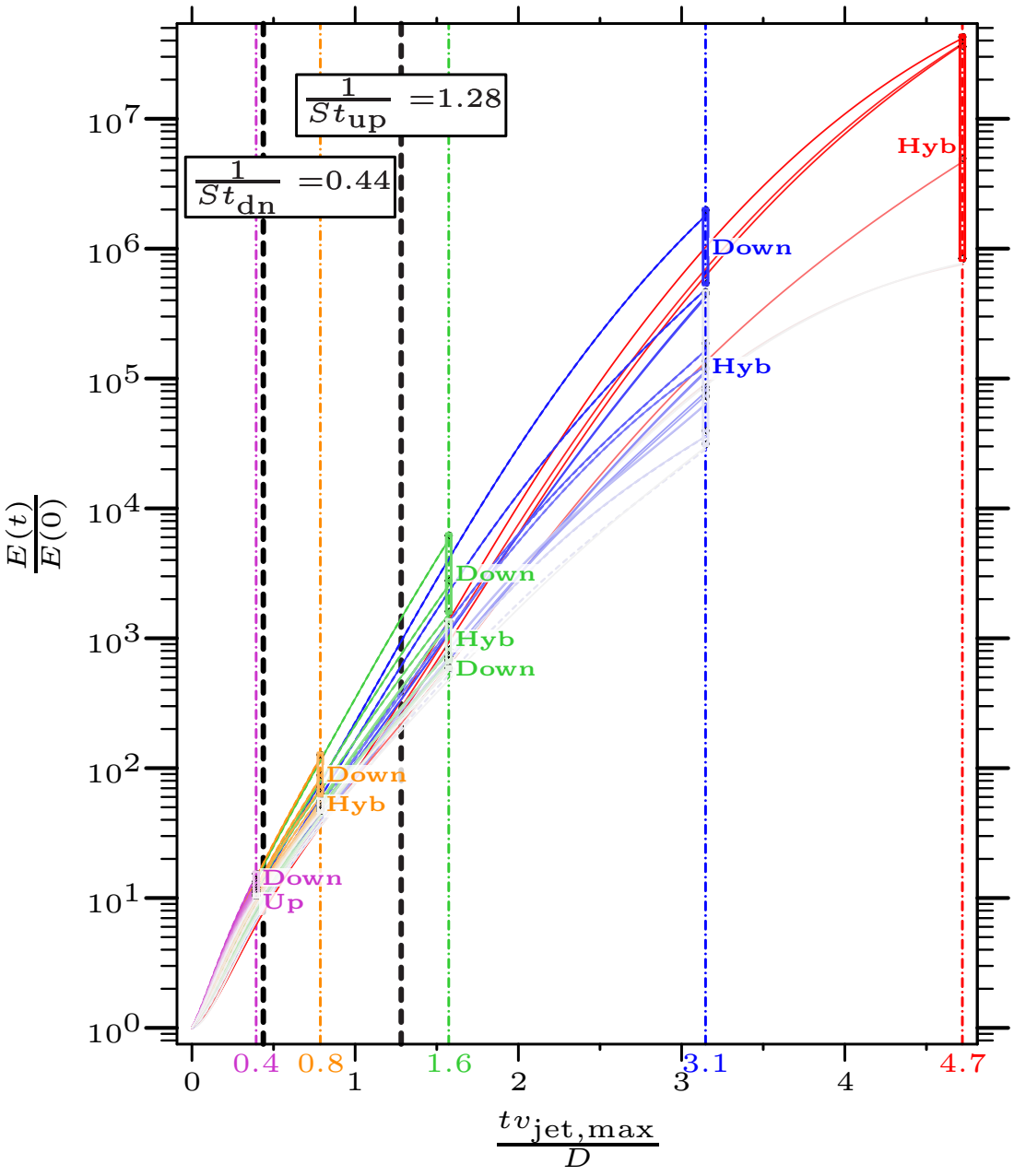

Figure 6.2: Similar to figure 6.1, but for case *R*4. Additionally, the time-scale of the downstream shear-layer, $1/St_{\mathrm{dn}}$, is shown as another vertical black dashed line.

symmetry plane at $z = 0$.

6.2 Optimal perturbations for case $R2$

Figure 6.1 suggests some overall conclusions from optimal perturbation analysis of case $R2$. For short-time (i.e. $\tau < 1/St_{up}$), asymmetric perturbations dominate where the CVP forms, with sub-optimal perturbations growing along the downstream shear-layer. For $\tau = 0.8$, there are sub-optimal modes that symmetrically perturb both the downstream shear-layer and the CVP.

Not until the characteristic time-scale (i.e. $\tau \approx 1/St_{up}$) does perturbing the downstream shear-layer become optimal. On this time-scale, it becomes clear from figure 6.1 that asymmetric perturbations of the CVP are sub-optimal. This gives rise to other sub-optimal perturbations of the upstream shear-layer that quickly become significant for larger time-scales.

When optimal perturbations are considered for long-time horizons (i.e. $\tau > 1/St_{up}$), the modes result in growth along the upstream shear-layer. Furthermore, sub-optimal perturbations move from the downstream shear-layer to complex perturbations with higher circumferential wavenumbers along the upstream shear-layer for $3.2 \leq \tau \leq 4.9$. Finally, the group of optimal perturbations that have the lowest growth factors include a series of hybrid perturbations that grow along both the upstream and downstream shear-layers, as well as a series of increasing circumferential wavenumbers. The three time horizons are discussed in detail below.

6.2.1 Short-time horizon

For the short-time horizon, optimal perturbations take advantage of mechanisms that act much faster than the characteristic time-scale $1/St_{up} = 1.54$ (i.e. period of upstream shear-layer roll-up) to produce energy growth. First and foremost are the asymmetric perturbations, which dominate energy growth over the short time-scales $0.4 \leq \tau \leq 0.8$. The state of these optimal perturbations at $t = \tau$ are shown in figures 6.3 and 6.4. These perturbations ride along the CVP present in the baseflow as they propagate in

(a) (b)

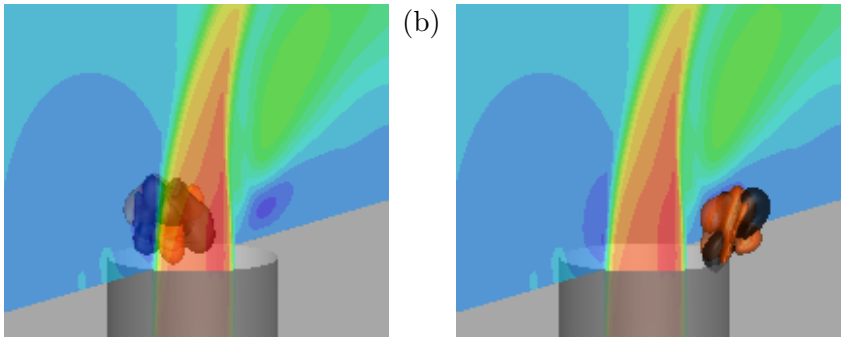

Figure 6.3: Case $R2$, short-time horizon, $\tau = 0.4$, final state of the leading asymmetric optimal perturbations.

(a) (b)

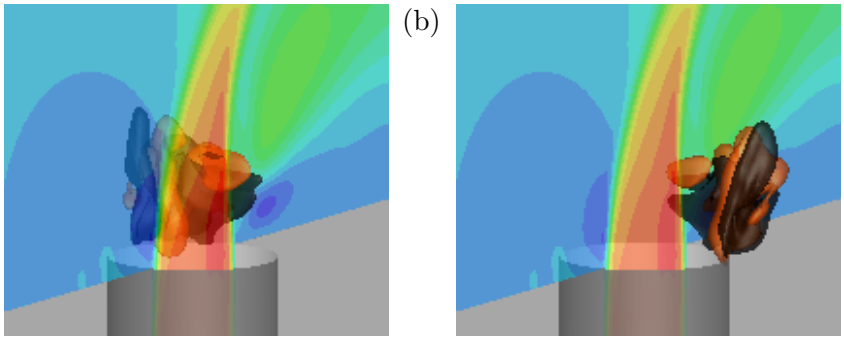

Figure 6.4: Case $R2$, short-time horizon, $\tau = 0.8$, final state of the leading asymmetric optimal perturbations.

helical fashion downstream. Not only are there pairs of asymmetric perturbations, but a series of increasing circumferential wavenumbers characterize the next few sub-optimal eigenmodes for $\tau = 0.4$. The final state of the negative z-side perturbations are shown in figure 6.5. The asymmetric initial perturbations originate at the jet nozzle exit (not shown) and propagate downstream on either side of the CVP.

The next sub-optimal perturbations for $\tau = 0.4$, 0.8 grow along the downstream shear-layer, which are shown in figure 6.6 and 6.7. The evolution of the downstream shear-layer perturbations are characteristic of the downstream shear-layer roll-up observed in DNS (figure 4.4a). These perturbations originate within the nozzle on the downstream side as shown in figure 6.6a and 6.7a. The sub-optimal downstream shear-layer perturbations (figure 6.6) generate $\approx 68\%$ of the energy growth compared to the

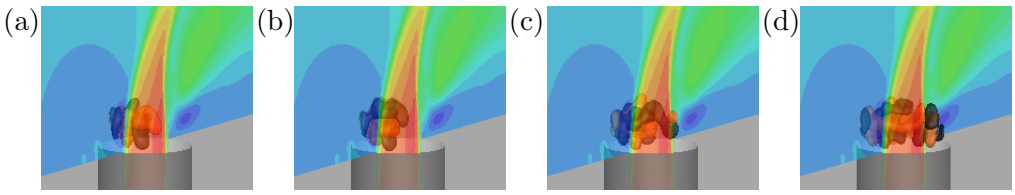

Figure 6.5: Case $R2$, short-time horizon, $\tau = 0.4$, final state of sub-optimal asymmetric optimal perturbations with decreasing growth factors and increasing circumferential wavenumbers.

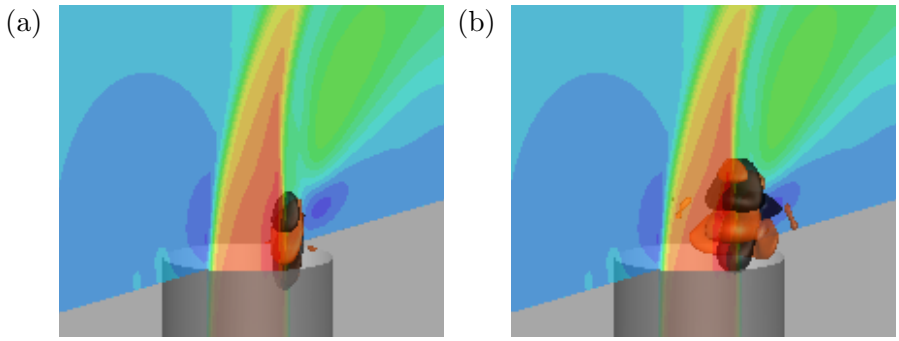

Figure 6.6: Case $R2$, short-time horizon, $\tau = 0.4$, origination (a) and final state (b) of the sub-optimal downstream shear-layer perturbation.

leading asymmetric optimal perturbation (figure 6.3) for $\tau = 0.4$. Comparatively, when $\tau = 0.8$, the sub-optimal downstream shear-layer perturbation (figure 6.7) generates $\approx 73\%$ of the energy growth compared to the optimal asymmetric perturbation (figure 6.4). This highlights the fact that as τ increases these perturbations are becoming efficient at producing energy growth.

The least effective sub-optimal perturbations that generate the lowest energy growth for $0.4 \leq \tau \leq 0.8$ include a series of hybrid and higher wavenumber versions of the previously shown perturbations. For $\tau = 0.4$, the least efficient perturbations that were found are the hybrid perturbations that attempt to generate energy from both the CVP and the downstream shear-layer. These perturbations are shown in figure 6.8. The results are similar for $\tau = 0.8$, which have a series of hybrid CVP and downstream shear-layer perturbations shown in figure 6.9 with increasing wavenumbers and decreasing growth factors.

(a) (b)

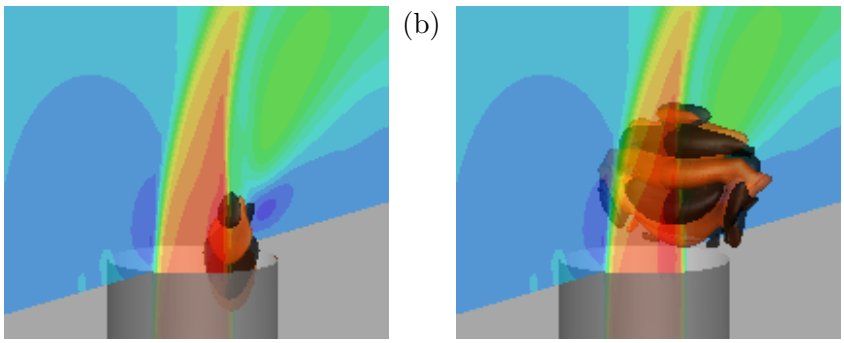

Figure 6.7: Case $R2$, short-time horizon, $\tau = 0.8$, origination (a) and final state (b) of the sub-optimal downstream shear-layer perturbation.

(a) (b)

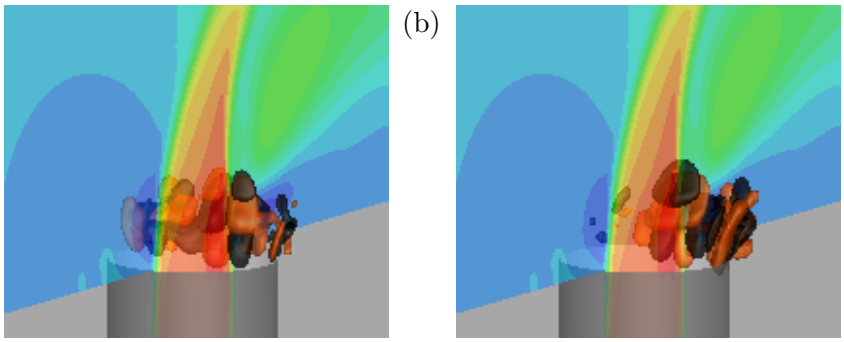

Figure 6.8: Case $R2$, short-time horizon, $\tau = 0.4$, final state of the sub-optimal hybrid asymmetric downstream shear-layer and perturbations.

(a) (b) (c) (d)

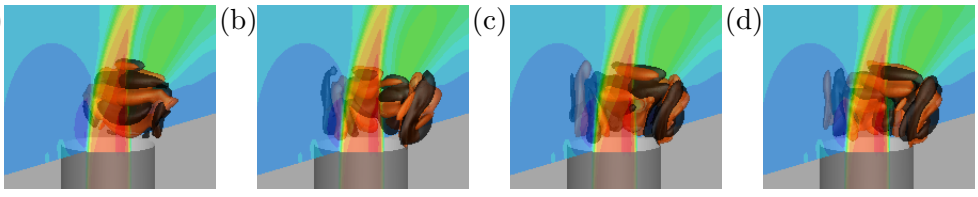

Figure 6.9: Case $R2$, short-time horizon, $\tau = 0.8$, final state of sub-optimal asymmetric optimal perturbations with decreasing growth factors and increasing circumferential wavenumbers.

(a) (b)

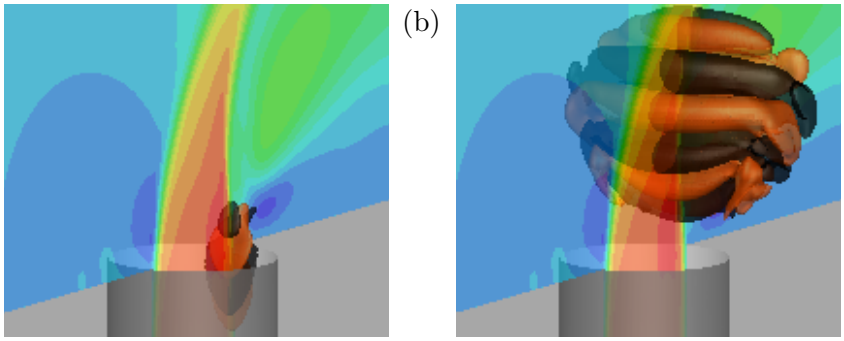

Figure 6.10: Case $R2$, characteristic-time horizon, $\tau = 1.6$, origination (a) and final state (b) of the leading downstream shear-layer optimal perturbations.

(a) (b)

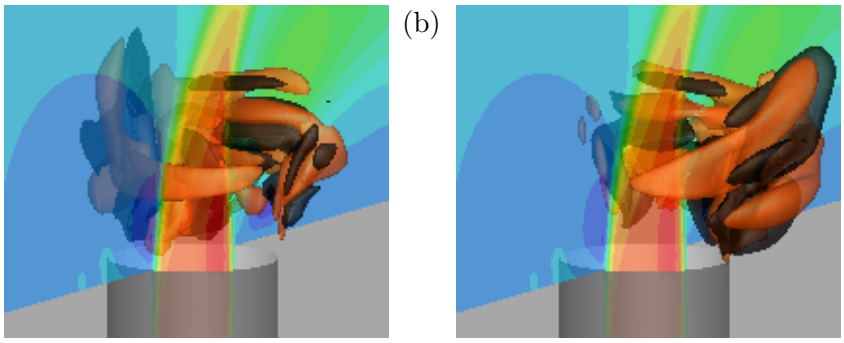

Figure 6.11: Case $R2$, characteristic-time horizon, $\tau = 1.6$, final state of the sub-optimal hybrid asymmetric downstream shear-layer optimal perturbations.

6.2.2 Characteristic-time horizon

The characteristic-time scale optimal perturbations take advantage of processes that act on the order of the characteristic time-scale $1/St_{up} = 1.54$ to increase energy. As τ is increased beyond the short-time-scale, there is a bifurcation. The highest energy growth optimal modes change from asymmetric perturbations (figure 6.11) to perturbations that grow along the downstream shear-layer (figure 6.10). Figure 6.1 clearly shows the significant drop in energy growth for the asymmetric perturbations, which are now sub-optimal for $\tau = 1.6$.

Sub-optimal perturbations of the upstream shear-layer are found for the first time

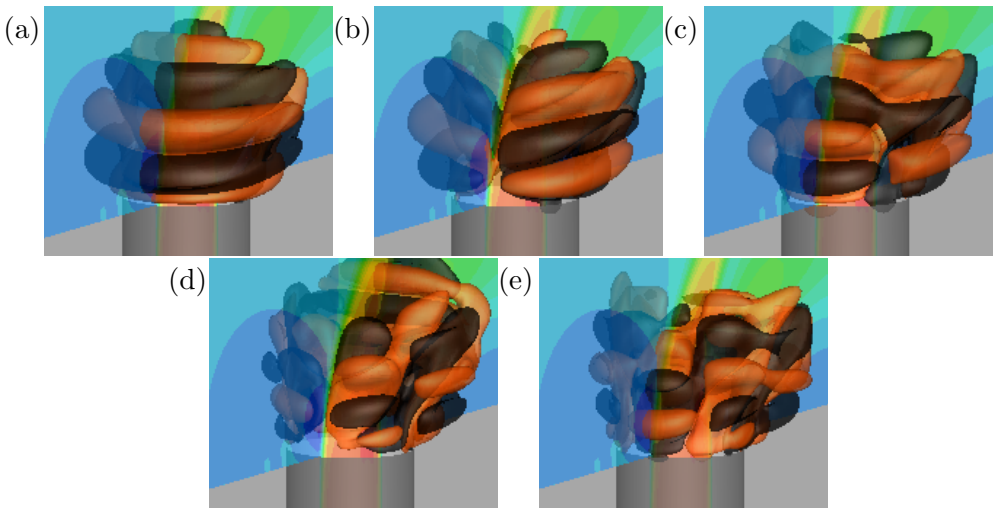

Figure 6.12: Case $R2$, characteristic-time horizon, $\tau = 1.6$, final state of the sub-optimal upstream shear-layer optimal perturbations, along with higher circumferential wavenumbers with decreasing growth factors.

in the optimal analysis at the characteristic-time scale. The upstream shear-layer sub-optimal modes are shown in figure 6.12, arranged with decreasing energy growth and increasing circumferential wavenumbers. It is significant that higher wavenumber counterparts to the upstream shear-layer mode are also found. This shows that the upstream shear-layer region is becoming a significant energy growth opportunity since higher wavenumber downstream shear-layer and asymmetric perturbations are no longer recovered in the analysis.

6.2.3 Long-time horizon

The long-time scale optimal perturbations take advantage of processes that act on larger times than the characteristic time-scale $1/St_{up} = 1.54$. Another bifurcation in optimal perturbation analysis for case $R2$ happens over the long-time horizon. In the range $1.6 \leq \tau \leq 3.2$ the optimal perturbations change from acting along the downstream shear-layer (figure 6.14) to the upstream shear-layer (figure 6.13). Also, there are, several higher wavenumber counterparts to the upstream shear-layer optimal perturbations shown in figure 6.13b-d.

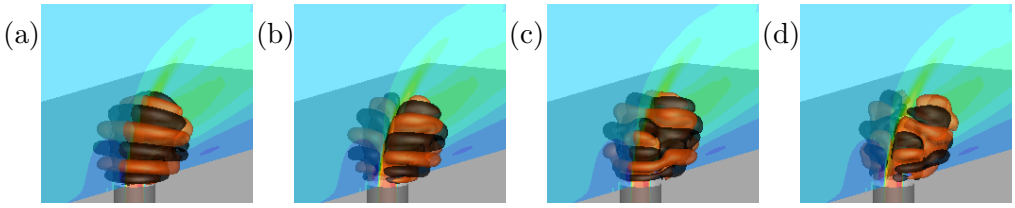

Figure 6.13: Case $R2$, long-time horizon, $\tau = 3.2$, final state of the leading upstream shear-layer optimal perturbations, along with lower growth factor perturbations with increasing circumferential wavenumbers.

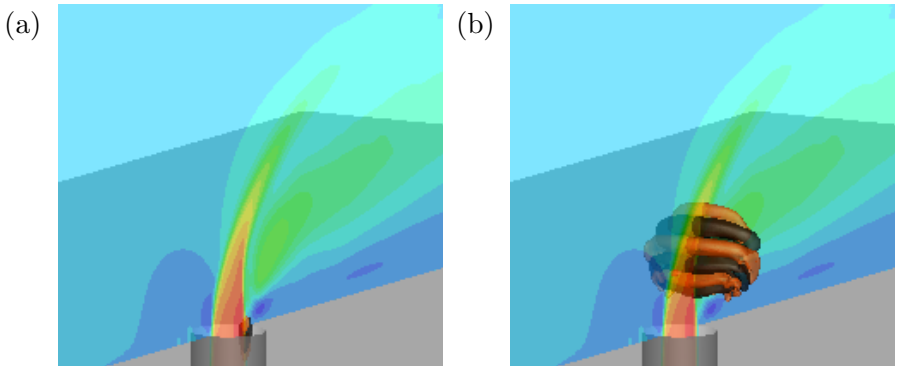

Figure 6.14: Case $R2$, long-time horizon, $\tau = 3.2$, origination (a) and final state (b) of the sub-optimal downstream shear-layer optimal perturbation.

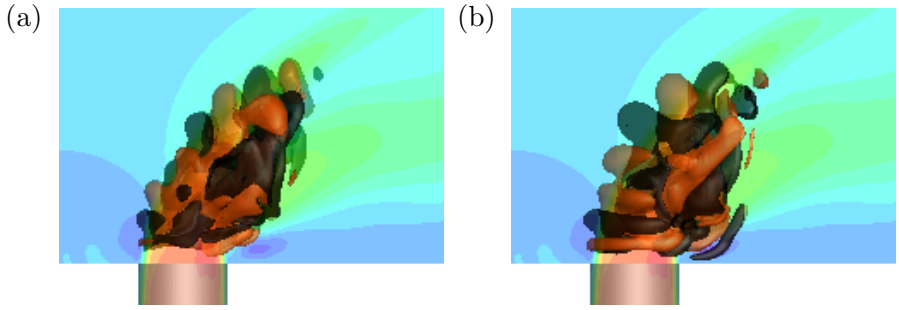

Figure 6.15: Case $R2$, long-time horizon, $\tau = 3.2$, final state of the sub-optimal hybrid shear-layer optimal perturbations.

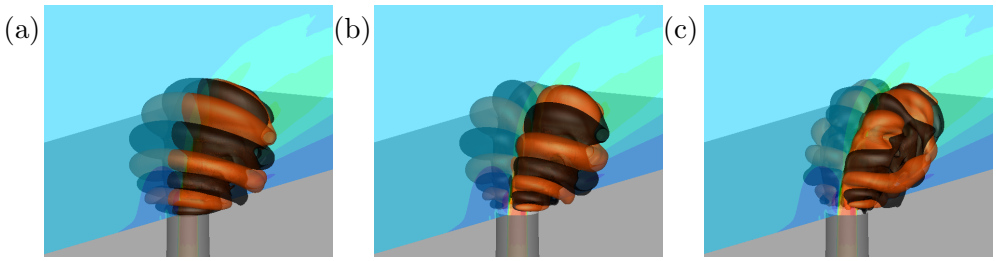

Figure 6.16: Case $R2$, long-time horizon, $\tau = 4.9$, final state of the leading upstream shear-layer optimal perturbations, along with lower growth factor perturbations with increasing circumferential wavenumbers.

The least effective perturbations generate energy along the upstream and downstream shear-layers simultaneously. The evolution of these hybrid perturbations are shown in figure 6.15. For the longest time horizon that was studied for case $R2$, the leading optimal perturbations again act along the upstream shear-layer to generate the most energy growth, which are visualized in figure 6.16. This is consistent with the results from the linear stability and adjoint sensitivity analyses in chapters 4 and 5, which examined the stability and sensitivity at the asymptotic limit of time. Now the first few sub-optimal perturbations are also upstream shear-layer modes with higher circumferential wavenumbers (figure 6.16b-c).

Shown in figure 6.17 are the remaining sub-optimal perturbations organized with decreasing energy growth that are a set of hybrid upstream and downstream shear-layer modes. For these longer time modes, there are no longer any purely downstream

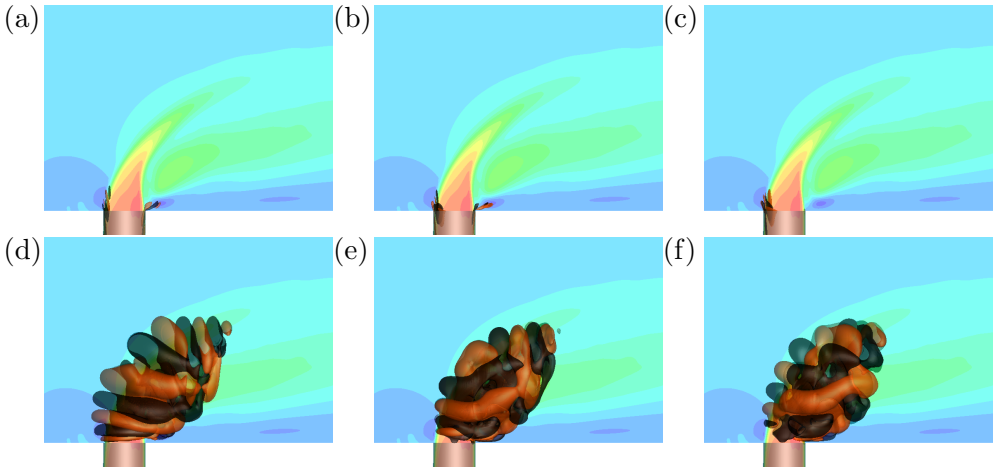

Figure 6.17: Case $R2$, long-time horizon, $\tau = 4.9$, originations (a-c) and final state (d-f) of the sub-optimal hybrid shear-layer optimal perturbations, organized in order of decreasing growth factor.

shear-layer optimal perturbations. Instead, perturbations act on both the upstream and downstream side of the jet nozzle exit (see figure 6.17a-c) to generate growth along the jet trajectory (see figure 6.17d-f).

6.3 Optimal perturbations for case $R4$

Similar to case $R2$, some overall conclusions from optimal perturbation analysis for case $R4$ are highlighted using figure 6.2. Short-time horizon optimal perturbations are dominated by growth along the downstream shear-layer for $0.4 \leq \tau \leq 0.8$. However, there are sub-optimal perturbations that grow along the upstream shear-layer, as well as hybrid perturbations for both shear-layers when $\tau = 0.8$.

For the characteristic time-scale, the downstream shear-layer growth again dominates. However, a group of sub-optimal hybrid perturbations also highlight significant growth. For this value of $\tau = 1.6$, there are no longer purely upstream shear-layer sub-optimal modes, only hybrids that grow along the upstream and downstream shear-layers.

Over the long time horizons, it is shown that all optimal perturbations are some

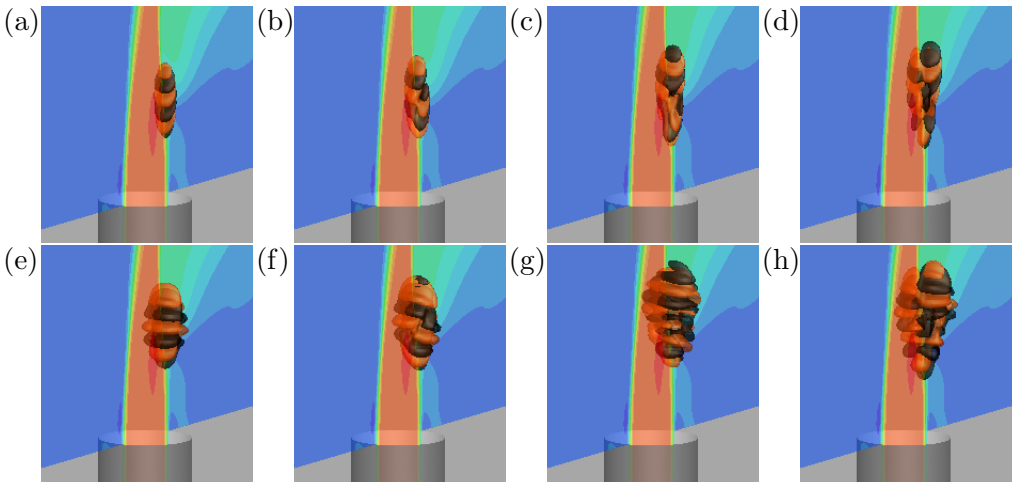

Figure 6.18: Case $R4$, short-time horizon, $\tau = 0.4$, origination (a-d) and final state (e-h) of the leading downstream shear-layer perturbation, in addition to sub-optimal higher wavenumber perturbations with decreasing growth factors that are not symmetric across the $z = 0$ plane.

form of hybrid mode. When $\tau = 3.1$, there is often with a bias towards either the upstream or downstream shear-layers. However, for $\tau = 4.7$, the hybrid modes have less significant biases, with a more evenly spread perturbation across the upstream and downstream shear-layers.

6.3.1 Short-time horizon

The short-time scale optimal perturbations take advantage of processes that act on times shorter the characteristic time-scale (i.e. less than $1/St_{up} = 1.28$) to increase energy. Unlike case $R2$, there are no asymmetric perturbation modes. Instead, the short-time ($0.4 \leq \tau \leq 0.8$) optimal modes, and the first few sub-optimal modes, generate energy growth by as they propagate along the downstream shear-layer. The group of downstream shear-layer modes for $\tau = 0.4$ are shown in figure 6.18, and for $\tau = 0.8$ in figure 6.19. For this short-time, the perturbation modes do not have much time to advect along the baseflow, which results in the focus on the downstream shear-layer to generate growth.

The next few sub-optimal perturbation modes make use of the upstream shear-layer

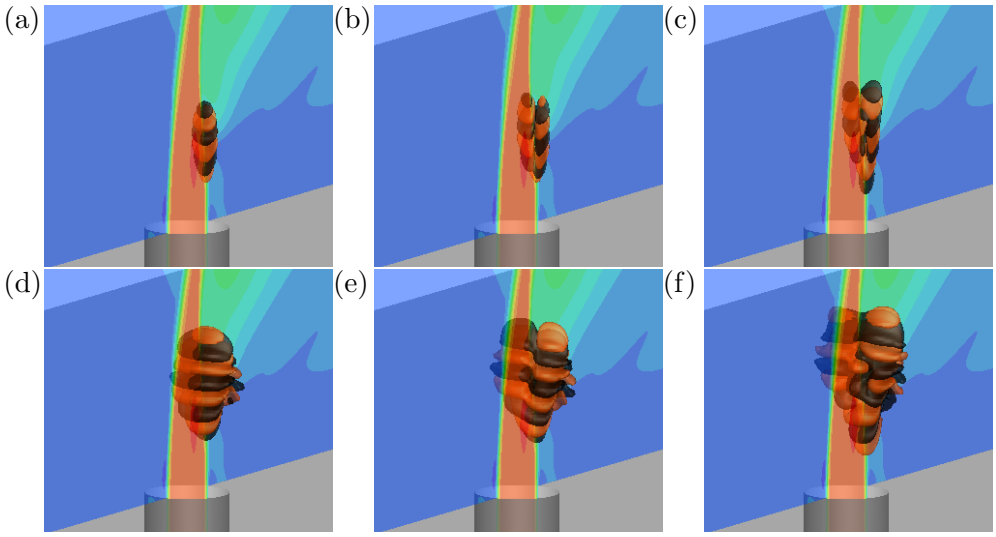

Figure 6.19: Case $R4$, short-time horizon, $\tau = 0.8$, origination (a-c) and final state (d-f) of the leading downstream shear-layer perturbation, in addition to sub-optimal higher wavenumber perturbations with decreasing growth factors that are not symmetric across the $z = 0$ plane.

to grow on top of the baseflow. Figure 6.20 shows that when $\tau = 0.4$, the upstream shear-layer perturbation has a circumferential wavenumber. Conversely, for $\tau = 0.8$, figure 6.21a shows a sub-optimal perturbation mode with no circumferential wavenumber that generates the highest growth compared to its higher wavenumber counterparts (figure 6.21).

6.3.2 Characteristic-time horizon

Optimal perturbations on the characteristic-time horizon take advantage of processes that act on the order of the characteristic time-scale $1/St_{up} = 1.28$, to increase energy. The leading optimal perturbations are again a group of modes that grow along the downstream shear-layer. Figure 6.22 shows the leading optimal perturbation for $\tau = 1.6$, along with the first few sub-optimal modes which also grow predominately along the downstream shear-layer, but with higher circumferential wavenumbers.

The remaining sub-optimal perturbation modes are all hybrid perturbation modes that show growth along upstream and downstream shear-layers simultaneously, and are

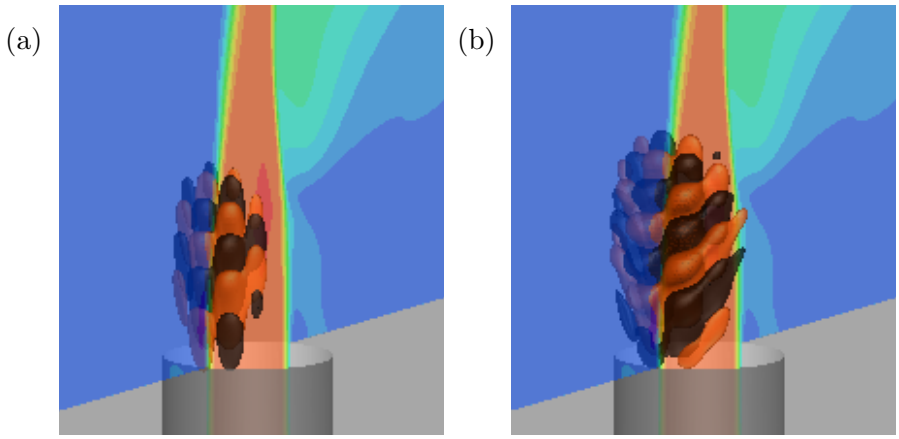

Figure 6.20: Case $R4$, short-time horizon, $\tau = 0.4$, origination (a) and final state (b) of sub-optimal upstream shear-layer perturbation with a high circumferential wavenumber.

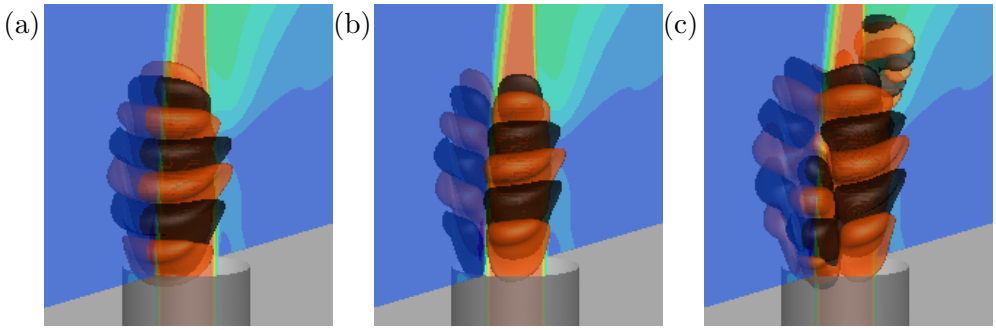

Figure 6.21: Case $R4$, short-time horizon, $\tau = 0.8$, final state of sub-optimal upstream shear-layer perturbation, along with lower growth factor perturbation with higher circumferential wavenumbers.

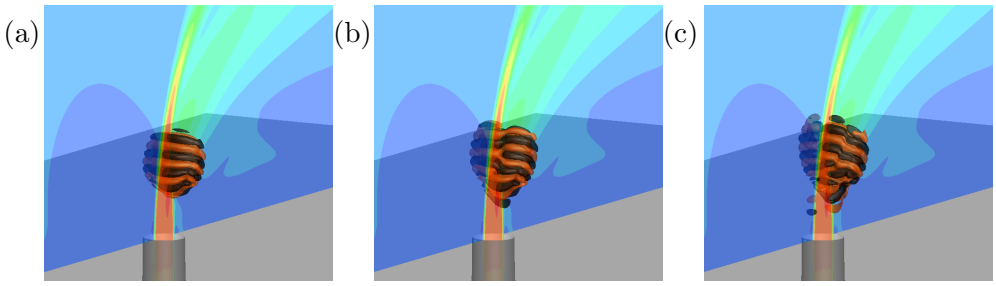

Figure 6.22: Case $R4$, characteristic-time horizon, $\tau = 1.6$, final state of the leading downstream shear-layer optimal perturbations, as well as sub-optimal perturbations with decreasing growth factor and increasing circumferential wavenumbers.

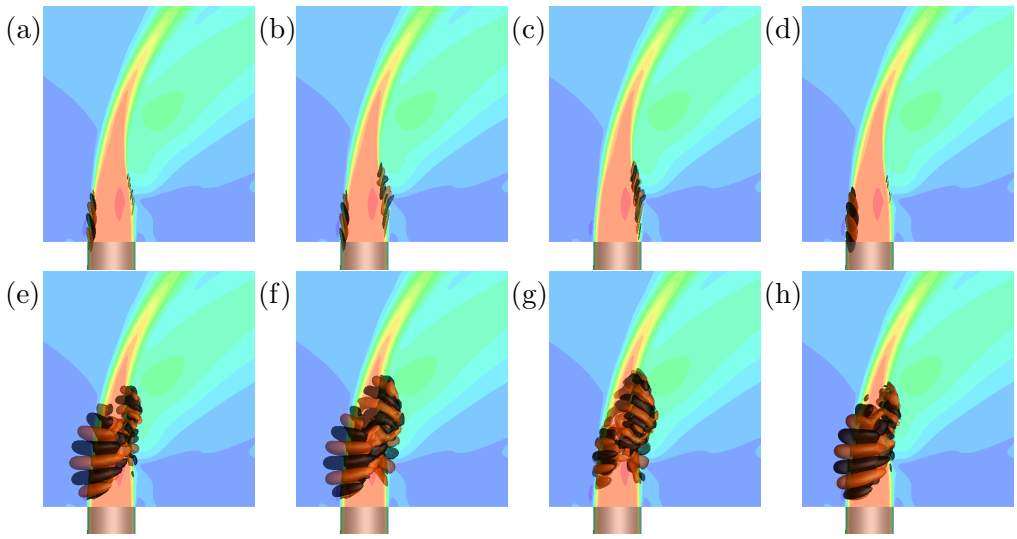

Figure 6.23: Case $R4$, characteristic-time horizon, $\tau = 1.6$, origination (a-d) and final state (e-h) of the sub-optimal hybrid shear-layer optimal perturbations organized with decreasing growth factors.

presented in figure 6.23. These modes have varying biases towards the upstream and downstream shear-layers, and thus have slightly different evolutions. Interestingly, the final state of the perturbations at time τ appear to be optimized so that the upstream and downstream perturbations propagate along the shear-layers and meet up at the collapse of the potential core at this time.

6.3.3 Long-time horizon

The long-time scale optimal perturbations take advantage of processes that act on larger times than the characteristic time-scale $1/St_{up} = 1.28$. The optimal perturbation for $\tau = 3.1$, shown in figure 6.24, continues to take advantage of the downstream shear-layer as the only path to generate energy growth. The initial perturbation (figure 6.24a) is elevated from the jet nozzle exit and grows significantly around the downstream shear-layer as it travels further downstream. The sub-optimal perturbations for $\tau = 3.1$ are shown in figure 6.25 and again show different biases towards the upstream and downstream shear-layers.

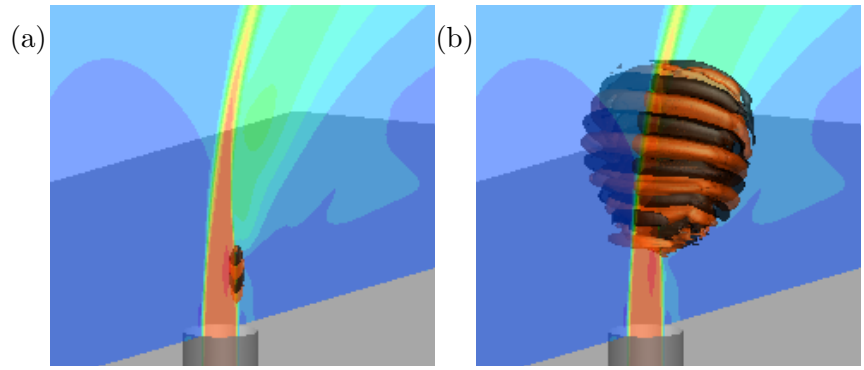

Figure 6.24: Case $R4$, characteristic-time horizon, $\tau = 3.1$, origination (a) and final state (b) of the leading downstream shear-layer optimal perturbations.

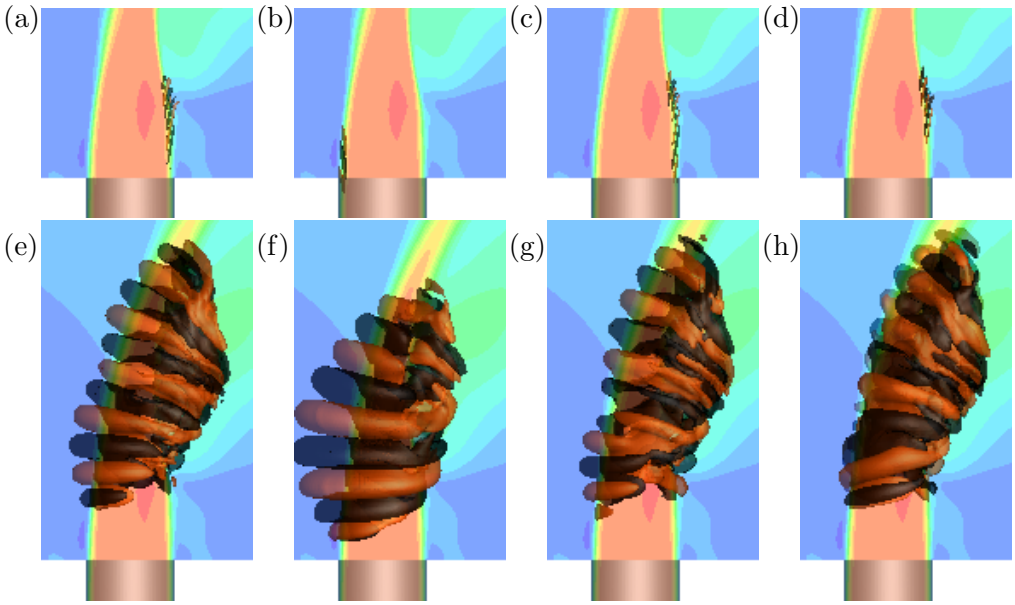

Figure 6.25: Case $R4$, long-time horizon, $\tau = 3.1$, sub-optimal hybrid shear-layer perturbations organized with decreasing growth factor. Note that the initial perturbations (a-d) are above the associated final states (e-h).

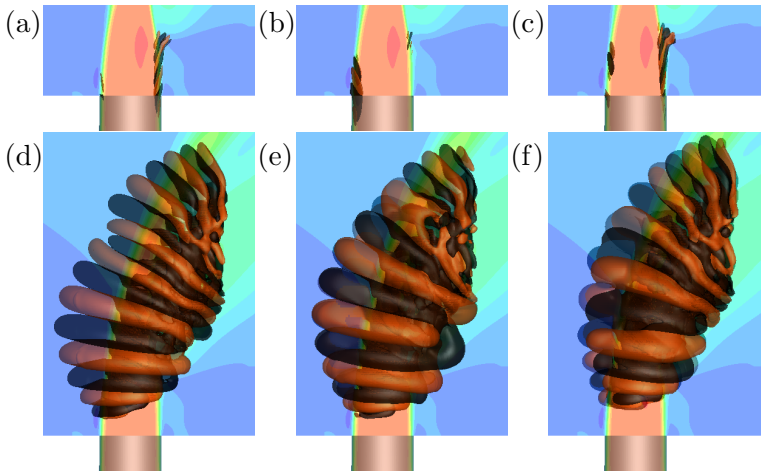

Figure 6.26: Case $R4$, long-time horizon, $\tau = 4.7$, sub-optimal hybrid shear-layer perturbations organized with decreasing growth factor. Note that the initial perturbations (a-c) are above the associated final states (d-f).

For the longest time horizon of $\tau = 4.7$ for case $R4$, all of the perturbations are shown to grow in energy along both upstream and downstream shear-layers (figure 6.26). The initial perturbations (figure 6.26a-c) show biases toward both the shear-layers, but their evolution (figure 6.26d-f) is qualitatively similar. Therefore, for long time horizons for case $R4$, the best way to perturb the baseflow is to simultaneously perturb the upstream and downstream shear-layers. This is consistent with the results from linear stability and adjoint sensitivity analyses in figure 5.1b, which highlights that the upstream and downstream shear-layer instability modes have similar growth rates.

6.4 Summary

Global optimal perturbation analysis is shown to provide insight into the different perturbations influencing the JICF for cases $R2$ and $R4$.

For case $R2$, it is shown that for short-time horizons, asymmetric perturbations dominate energy growth. However, as the time horizon is increased, the optimal perturbation changes twice. For the characteristic-time horizon, the optimal perturbation

shifts to the downstream shear-layer. Over the long-time horizon, the optimal perturbation switches back, to growth along the upstream shear-layer.

When $R = 4$, results from optimal perturbation analysis show that perturbation growth on top of the baseflow for short- and characteristic-time horizons are focused along the downstream shear-layer. Not until the time horizon increases beyond the characteristic-time do perturbations along the upstream shear-layer become the efficient way to generate growth. Furthermore, for the longest-time horizon, optimal perturbations are all of the hybrid nature, which consist of growth along both the upstream and downstream shear-layers.

Chapter 7

Conclusion

The extensive use of the JICF in engineering applications provides motivation for this study. Previous studies have greatly increased our understanding of the JICF, but there is still much to be discovered in terms of controlling the JICF to our advantage. Shapiro *et al.* (2006) studied jet penetration and mixing experimentally by acoustically pulsing the jet. Their study largely provided data that can be used to control jet penetration and mixing characteristics. Sau & Mahesh (2010) showed that for the pulsed JICF the optimal forcing for jet penetration could be described by considering the vortex rings produced by strong pulsing. The study by Megerian *et al.* (2007) discovered that the upstream shear-layer had a stability transition between $R = 2$ and $R = 4$. $R = 2$, with its strong tonal frequency, was less receptive to external forcing, and displayed absolute-like instability behavior. Conversely, when $R = 4$ there was a range of frequencies along the upstream shear-layer that were much weaker and more receptive to forcing at external frequencies. This was discussed as being analogous to a convectively unstable flow which is more readily influenced by external forcing. Iyer & Mahesh (2016) proposed an analogy to parallel flow stability of counter-current mixing layers (Huerre & Monkewitz, 1985) to explain the stability transition of the upstream shear-layer for the JICF; this has been shown to agree well for cases $R2$ and $R4$.

The goal of this research is to understand the stability and sensitivity of the low-speed JICF from a global perspective using linear stability, adjoint sensitivity, and

optimal perturbation analyses. Such understanding provides insight into how to best control the JICF and paves the way for more sophisticated control strategies based on, where the regions with the largest energy growth are most sensitive to actuation. The combination of these three analyses provides a description of the stability and sensitivity of the JICF, for both finite and asymptotic times.

The global modes from linear stability analysis highlight the areas where the largest growth are observed asymptotically. This provides insight into the best placement of sensors for measuring the flow state. The upstream shear-layer linear stability analysis eigenmodes were shown to have frequencies that agree well with those observed in DNS (Iyer & Mahesh, 2016) and experiment (Megerian *et al.*, 2007). Additionally, DMD modes (Iyer & Mahesh, 2016) were shown to qualitatively agree well with the linear stability analysis eigenmodes, suggesting that linear stability provides relevant insight into the turbulent flow. The linear stability analysis results show that case $R2$ is dominated by the upstream shear-layer instability. However, there are other eigenmodes that are asymmetric across the mid-plane and much lower frequency modes that travel far downstream and have finger-like fluid structures that resemble wake vortices. Case $R4$ also has an upstream shear-layer instability mode, but there is an additional downstream shear-layer instability that has a higher growth rate. The importance of the downstream shear-layer stability has not been discussed before. Furthermore, the asymmetric instabilities for case $R4$ are shown to have higher relative growth rates than case $R2$, highlighting their increased significance to the overall stability dynamics. This behavior also suggests an explanation for the asymmetric CVP eigenmodes that are observed experimentally at higher R.

Global adjoint sensitivity analysis results are complementary, as they provide sensitivity information that outlines the regions where the linear stability analysis modes are sensitive to momentum forcing. This information is valuable when trying to decide the most effective placement for actuators. The upstream shear-layer modes for both cases are most sensitive along the upstream side of the jet nozzle exit. The asymmetric modes for both cases are most sensitive on each side of the upstream side of the jet nozzle exit. For case $R4$, the downstream shear-layer is most receptive to actuation

at an elevated position from the jet nozzle exit on the downstream side. Interestingly, the low frequency modes are sensitive to perturbations on the upstream side of the jet nozzle, and wrap around to the outer edge. For $R4$, the low frequency modes are sensitive to an extended region upstream of the jet nozzle exit in the incoming cross-flow, highlighting the connection to perturbations in the incoming cross-flow on the fluid structures that resemble wake vortices. Wavemaker regions are also computed for the upstream shear-layer modes from the linear stability and adjoint sensitivity analyses and are qualitatively different for cases $R2$ and $R4$. For case $R2$, the wavemaker region is concentrated to a small region near the upstream edge of the jet nozzle exit right where the upstream shear-layer is formed. Conversely, case $R4$ has a wavemaker region that extends along a considerable length of the upstream shear-layer. These differences are consistent with the stability transition of the upstream shear-layer.

Global optimal perturbation analysis examines the stability and sensitivity at finite time-scales to determine the 'most dangerous' disturbances for the JICF. The optimal perturbations provide additional information about where the most sensitive regions to actuation are located. The evolutions of the perturbations highlight the paths that the perturbations follow to generate energy growth, and provide insight into actuation (initial state) and sensor placement (final state). For case $R2$, the optimal perturbations for short-time display the ability to grow along each half of the CVP by perturbing the left- and right-sides just above the downstream side of the jet nozzle exit. For time horizons of the order of the upstream shear-layer shedding period, the optimal actuation occurs along the downstream side of the jet nozzle exit, and results in growth along the downstream shear-layer. For the longer time-scales, hybrid perturbations that grow along the upstream and downstream shear-layers simultaneously are the most optimal. For case $R4$, the optimal perturbations along the downstream shear-layer dominate for lower time-scales. However, for time-scales longer than the characteristic-time horizon, hybrid perturbations are again the most efficient at generating energy by leveraging growth along both shear-layers.

The research presented in this dissertation uses high-fidelity numerical methods and high performance computing to study the stability and sensitivity of the low-speed JICF

from a global perspective. The results presented are state-of-the-art, and represent the largest stability and sensitivity simulations performed, to the best of the authors' knowledge. Valuable insight is gained that increases understanding of the stability and sensitivity of the JICF. This information provides insight into the best placement of both sensors and actuators to efficiently manipulate the most dominant instabilities of the JICF.

Bibliography

Akervik, E., Brandt, L., Henningson, D. S., Hœpffner, J., Marxen, O. & Schlatter, P. 2006 Steady solutions of the Navier-Stokes equations by selective frequency damping. *Physics of Fluids* **18** (6), 068102.

Alves, L. S. De B., Kelly, R. E. & Karagozian, A. R. 2008 Transverse-jet shear-layer instabilities. Part 2. Linear analysis for large jet-to-crossflow velocity ratio. *Journal of Fluid Mechanics* **602**, 383–401.

Arnoldi, W. E. 1951 The principle of minimized iteration in the solution of the matrix eigenproblem. *Quarterly of Applied Mathematics* **9**, 17–29.

Babu, P. C. & Mahesh, K. 2004 Upstream entrainment in numerical simulations of spatially evolving round jets. *Physics of Fluids* **16** (10), 3699–3705.

Bagheri, S., Schlatter, P., Schmid, P. J. & Henningson, D. S. 2009 Global stability of a jet in crossflow. *Journal of Fluid Mechanics* **624**, 33–44.

Barkley, D. 2006 Linear analysis of the cylinder wake mean flow. *Europhysics Letters* **75** (5), 750–756.

Barkley, D., Blackburn, H. M. & Sherwin, S. J. 2008 Direct optimal growth analysis for timesteppers. *International Journal for Numerical Methods in Fluids* **57**, 1435–1458.

Boberg, L. & Brosa, U. 1988 Onset of Turbulence in a Pipe. *Z. Naturforsch* **43a**, 697–726.

Butler, K. M. & Farrell, B. F. 1994 Nonlinear equilibration of two-dimensional optimal perturbations in viscous shear flow. *Physics of Fluids* **4**, 1637–1650.

Cater, J. E. & Soria, J. 2002 The evolution of round zero-net-mass-flux jets. *Journal of Fluid Mechanics* **472**, 167–200.

Chang, P. A., Vargas, A., Jiang, M., Lummer, D. & Mahesh, K. 2011 Fully-resolved LES of weakly separated flows. *20th AIAA Computational Fluid Dynamics Conference* (June), 1–23.

Coelho, S. L. V. & Hunt, J. C. R. 1989 The dynamics of the near field of strong jets in crossflows. *Journal of Fluid Mechanics* **200**, 95–120.

Crighton, D. G. & Gaster, M. 1976 Stability of slowly diverging jet flow. *Journal of Fluid Mechanics* **77**, 397–413.

Criminale, W. O., Jackson, T. L. & Joslin, R. D. 2003 *Theory and computation of hydrodynamic stability*. Cambridge University Press.

Ding, Y. & Kawahara, M. 1998 Linear stability of incompressible flow using a mixed finite element method. *Journal of Computational Physics* **273**, 243–273.

Eiff, O. S., Kawall, J. G. & Keffer, J. F. 1995 Lock-in of vortices in the wake of an elevated round turbulent jet in a crossflow. *Experiments in Fluids* **19**, 203–213.

Eroglu, A. & Breidenthal, R. E. 2001 Structure, Penetration, and Mixing of Pulsed Jets in Crossflow. *AIAA Journal* **39** (3), 417–423.

Falgout, R. D. & Yang, U. M. 2002 HYPRE: A Library of High Performance Preconditioners. In *Computational Science ICCS 2002*, pp. 632–641. Berlin, Heidelberg.

Fric, T. F. & Roshko, A. 1994 Vortical structure in the wake of a transverse jet. *Journal of Fluid Mechanics* **279**, 1–47.

Getsinger, D.R., Gevorkyan, L., Smith, O.I. & Karagozian, A.R. 2014 Structural and stability characteristics of jets in crossflow. *Journal of Fluid Mechanics* **760**, 342–367.

Giannetti, F., Luchini, L. & Marino, L. 2009 Linear stability analysis of three-dimensional lid-driven cavity flow. In *Proceedings of the 19th Congress of the Italian Association of Theoretical and Applied Mechanics, 1417 September, 2009, Aras Edizioni, Ancona, Italy*, pp. 738.1–738.10.

Giannetti, F. & Luchini, P. 2007 Structural sensitivity of the first instability of the cylinder wake. *Journal of Fluid Mechanics* **581**, 167–197.

Gómez, F., Gómez, R. & Theofilis, V. 2014 On three-dimensional global linear instability analysis of flows with standard aerodynamics codes. *Aerospace Science and Technology* **32**, 223–234.

Gustavsson, L. H. 1991 Energy Growth of 3-Dimensional Disturbances in Plane Poiseuille Flow. *Journal of Fluid Mechanics* **224**, 241–260.

Hill, D. C. 1995 Adjoint systems and their role in the receptivity problem for boundary layers. *Journal of Fluid Mechanics* **292**, 183–204.

Huerre, P. & Monkewitz, P. A. 1985 Absolute and convective instabilities in open shear layers. *Journal of Fluid Mechanics* **159**, 151–168.

Hunt, J. C. R., Wray, A. A. & Moin, P. 1988 Eddies, streams, and convergence zones in turbulent flows. *Center for Turbulence Research, Proceedings of the Summer Program* pp. 193–208.

Ince, E. L. 1926 *Ordinary Differential Equations*. Dover.

Iyer, P. S. & Mahesh, K. 2016 A numerical study of shear layer characteristics of low-speed transverse jets. *Journal of Fluid Mechanics* **790**, 275–307.

Jang, H. & Mahesh, K. 2013 Large eddy simulation of flow around a reverse rotating propeller. *Journal of Fluid Mechanics* **729**, 151–179.

Jordan, P. & Colonius, T. 2013 Wave Packets and Turbulent Jet Noise. *Annual Review of Fluid Mechanics* **45**, 173–195.

Juniper, M. P., Hanifi, A. & Theofilis, V. 2014 Modal Stability Theory Lecture notes from the FLOW-NORDITA Summer School on Advanced Instability Methods for Complex Flows, Stockholm, Sweden. *Applied Mechanics Reviews* **66** (2), 024804–024804–22.

Kamotani, Y. & Greber, I. 1972 Experiments on a Turbulent Jet in a Cross Flow. *AIAA Journal* **10** (11), 1425–1429.

Karagozian, A. R. 2010 Transverse jets and their control. *Progress in Energy and Combustion Science* **36** (5), 531–553.

Kelso, R. M., Lim, T. T. & Perry, A. E. 1996 An experimental study of round jets in cross-flow. *Journal of Fluid Mechanics* **306**, 111–144.

Kelso, R. M. & Smits, A. J. 1995 Horseshoe vortex systems resulting from the interaction between a laminar boundary layer and a transverse jet. *Physics of Fluids* **7**, 153–158.

Krothapalli, A., Lourenco, L. & Buchlin, J. M 1990 Separated flow upstream of a jet in a crossflow. *AIAA Journal* **28** (3), 414–420.

Kumar, P. & Mahesh, K. 2017 Large eddy simulation of propeller wake instabilities. *Journal of Fluid Mechanics* **814**, 361–396.

Lehoucq, R. B., Sorensen, D. C. & Yang, C. 1997 ARPACK Users' Guide: Solution of Large Scale Eigenvalue Problems with Implicitly Restarted Arnoldi Methods.

Mahesh, K. 2013 The Interaction of Jets with Crossflow. *Annual Review of Fluid Mechanics* **45**, 379–407.

Mahesh, K., Constantinescu, G. & Moin, P. 2004 A numerical method for large-eddy simulation in complex geometries. *Journal of Computational Physics* **197**, 215–240.

Mahesh, K., Kumar, P., Gnanaskandan, A. & Nitzkorski, Z. 2015 LES Applied to Ship Research. *Journal of Ship Research* **59**, 238–245.

Margason, R. J. 1993 Fifty Years of Jet in Cross Flow Research. In *Aerospace Research & Development Conference 534*, pp. 1–41. Winchester, United Kingdom.

M'Closkey, R. T., King, J. M., Cortelezzi, L. & Karagozian, A. R. 2002 The actively controlled jet in crossflow. *Journal of Fluid Mechanics* **452**, 325–335.

McMahon, H. M., Hester, D. D. & Palfery, J. G. 1971 Vortex shedding from a turbulent jet in a cross-wind. *Journal of Fluid Mechanics* **48**, 73–80.

Megerian, S., Davitian, J., Alves, L. S. de B. & Karagozian, A. R. 2007 Transverse-jet shear-layer instabilities. Part 1. Experimental studies. *Journal of Fluid Mechanics* **593**, 93–129.

Morse, P. M. & Feshbach, H. 1953 *Methods of Theoretical Physics*. McGraw Hill.

Moussa, Z. M., Trischka, J. W. & Eskinazi, D. S. 1977 The near field in the mixing of a round jet with a cross-stream. *Journal of Fluid Mechanics* **80**, 49–80.

Muppidi, S. & Mahesh, K. 2005 Study of trajectories of jets in crossflow using direct numerical simulations. *Journal of Fluid Mechanics* **530**, 81–100.

Muppidi, S. & Mahesh, K. 2007 Direct numerical simulation of round turbulent jets in crossflow. *Journal of Fluid Mechanics* **574**, 59–84.

Muppidi, S. & Mahesh, K. 2008 Direct numerical simulation of passive scalar transport in transverse jets. *Journal of Fluid Mechanics* **598**, 335–360.

Narayanan, S., Barooah, P. & Cohen, J. M. 2003 Dynamics and Control of an Isolated Jet in Crossflow. *AIAA Journal* **41** (12), 2316–2330.

Peplinski, A., Schlatter, P. & Henningson, D. S. 2015 Global stability and optimal perturbation for a jet in cross-flow. *European Journal of Mechanics - B/Fluids* **49**, 438–447.

Pope, S. B. 2000 *Turbulent Flows*, 1st edn. Cambridge Univesity Press.

Reddy, S. & Henningson, D. S. 1993 Energy growth in viscous channel flows. *Journal of Fluid Mechanics* **252**, 209–238.

Reddy, S. C., Schmid, P. J. & Henningson, D. S. 1993 Pseudospectra of the Orr-Sommerfeld Operator. *SIAM Journal on Applied Mathematics* **53**, 15–47.

Regan, M. A. & Mahesh, K. 2017 Global linear stability analysis of jets in cross-flow. *Journal of Fluid Mechanics* **828**, 812–836.

Rowley, C. W., Mezić, I., Bagheri, S., Schlatter, P. & Henningson, D. S. 2009 Spectral analysis of nonlinear flows. *Journal of Fluid Mechanics* **641**, 115–127.

Sau, R. & Mahesh, K. 2007 Passive scalar mixing in vortex rings. *Journal of Fluid Mechanics* **582**, 449–461.

Sau, R. & Mahesh, K. 2008 Dynamics and mixing of vortex rings in crossflow. *Journal of Fluid Mechanics* **604**, 389–409.

Sau, R. & Mahesh, K. 2010 Optimization of pulsed jets in crossflow. *Journal of Fluid Mechanics* **653**, 365–390.

Schmid, P. J. 2007 Nonmodal Stability Theory. *Annual Review of Fluid Mechanics* **39**, 129–62.

Schmid, P. J. 2010 Dynamic mode decomposition of numerical and experimental data. *Journal of Fluid Mechanics* **656**, 5–28.

Schmid, P. J. & Henningson, D. S. 2001 *Stability and Transition in Shear Flows*. New York: Springer-Verlag.

Shapiro, S. R., King, J., M'Closkey, R. T. & Karagozian, A. R. 2006 Optimization of Controlled Jets in Crossflow. *AIAA Journal* **44** (6), 1292–1298.

Smith, S. H. & Mungal, M. G. 1998 Mixing, structure and scaling of the jet in crossflow. *Journal of Fluid Mechanics* **357**, 83–122.

Su, L. K. & Mungal, M. G. 2004 Simultaneous measurements of scalar and velocity field evolution in turbulent crossflowing jets. *Journal of Fluid Mechanics* **513**, 1–45.

Tammisola, O. & Juniper, M. P. 2016 Coherent structures in a swirl injector at Re = 4800 by nonlinear simulations and linear global modes. *Journal of Fluid Mechanics* **792**, 620–657.

Theofilis, V. 2011 Global Linear Instability. *Annual Review of Fluid Mechanics* **43**, 319–352.

Trefethen, L. N., Trefethen, A. E., Reddy, S. C. & Driscoll, T. A. 1993 Hydrodynamic Stability Without Eigenvalues. *Science* **261** (5121), 578–584.

Turton, S. E., Tuckerman, L. S. & Barkley, D. 2015 Prediction of frequencies in thermosolutal convection from mean flows. *Physical Review E* **91** (4), 1–10.

Verma, A., Jang, H. & Mahesh, K. 2012 The effect of an upstream hull on a propeller in reverse rotation. *Journal of Fluid Mechanics* **704**, 61–88.

Vyazmina, E. 2010 Bifurcations in a swirling flow. PhD thesis, École Polytechnique X.